Karlsruhe Institute of Technology

Department of Physics
IEKP and TLK(ITEP)

Measurement of Temperature Stability and Homogeneity of the KATRIN WGTS Cryostat

Master's thesis

to acquire the academic degree of

Master of Science (M.Sc.)

at the Department of Physics
at the Karlsruhe Institute of Technology
by

B.Sc. Alexander Curt Marsteller

prepared at the Institute of Experimental Nuclear Physics (IEKP) and at the Tritium Laboratory Karlsruhe (TLK) of the Institute for Technical Physics (ITEP)

Reviewer:	Prof. Dr. G. Drexlin
Second Reviewer:	Prof. Dr. B. Holzapfel
Advisor:	M. Hackenjos
Second Advisor:	H. Seitz-Moskaliuk

15.04.2016 – 14.04.2017

Erklärung zur Selbstständigkeit

Ich versichere, dass ich diese Arbeit selbstständig verfasst habe und keine anderen als die angegebenen Quellen und Hilfsmittel benutzt habe, die wörtlich oder inhaltlich übernommenen Stellen als solche kenntlich gemacht und die Satzung des KIT zur Sicherung guter wissenschaftlicher Praxis in der gültigen Fassung vom 17.05.2010 beachtet habe.

Karlsruhe, den 11.04.2017, ___________________________

Alexander Curt Marsteller

Als Ansichtsexemplar genehmigt von

Karlsruhe, den 11.04.2017, ___________________________

Prof. Dr. G. Drexlin

Contents

List of Figures

List of Tables

1. Introduction

The standard model of particle physics as a description of the fundamental properties and interactions of particles has time after time proven its worth as a scientific theory by accurately predicting the existence of several elementary particles before their experimental discovery [Gre12]. In particular, it predicted the existence of the Higgs boson, discovered in 2012 [Aad12, Cha12], which gives the other particles of the standard model their mass by interacting with them. However, this mechanism of giving particles mass requires the particles to exist in both left- and right-handed variety. Therefore, this mechanism does not work for the purely left-handed neutrinos of the standard model, meaning that according to the standard model, they should be massless particles [Lee57, Asn13]. In contrast to this prediction, oscillations between different neutrino flavors, which necessitate a mass difference between different mass eigenstates, have been found by several independent experiments [Fuk98, Suz99, Nak00, Ahm01, Mic06]. Therefore, the neutrino mass is a pathway into the interesting realm of physics beyond the standard model.

But the existence of the neutrino mass has more extensive consequences, as primordial neutrinos, produced during the earliest stages of our universe, have an immense impact on the formation of large structures such as galaxies and galaxy clusters, and are the best candidate for hot dark matter [Aba11]. Knowledge of the neutrino mass will thus allow pinning one of the fit parameters for cosmological models and determining the impact of neutrinos on the distribution of invisible mass throughout the universe.

Several experiments have attempted direct experimental measurement of the neutrino mass, but have only been able to derive an upper limits on the neutrino mass. The currently best limit of $2\,\mathrm{eV}/c^2$ ($95\,\%$ C. L.) was achieved by the Mainz and the Troitsk experiment [Kra05, Ase11]. Following in its predecessors' footsteps, the Karlsruhe Tritium Neutrino experiment (KATRIN), currently in its final commissioning phase at the Karlsruhe Institute of Technology (KIT), aims to measure the electron anti-neutrino mass via energy spectroscopy of β-decay electrons of tritium with an unprecedented accuracy. KATRIN measures the shape of the β-decay energy spectrum of tritium near its high energy endpoint. The specifications of KATRIN result in an experimental setup with a discovery potential of $5\,\sigma$ for a neutrino mass of $350\,\mathrm{meV}/c^2$ and the capability to push the upper limit on the neutrino mass down to $200\,\mathrm{meV}/c^2$ $90\,\%$ C. L. if no neutrino mass can be detected [Ang05, Dre13].

To achieve this unprecedented sensitivity, statistical and systematical uncertainties have to be stringently minimized. The reduction of statistical uncertainties requires a total measurement of 3 years with a Windowless Gaseous Tritium Source (WGTS) capable of producing 10^{11} β-electrons per second. To keep the systematical uncertainties at the low level required to reach the target sensitivity, the activity of this β-electron source also needs to be stable to 0.1 % [Bab12]. The stability of the source is influenced by several factors such as the purity and pressure of the tritium gas, as well as the temperature of the WGTS beam tube enclosing the gaseous tritium.

The focus of this work are the stability and homogeneity requirements of 0.1 % on the temperature of the WGTS beam tube. These requirements have to be fulfilled at an operation temperature of 30 K as well as along the entire beam tube length of 10 m and its diameter of 9 cm. For this purpose, a specialized cooling system and a temperature measurement system have been developed and tested in a prototype experiment called Demonstrator, where their viability for neutrino mass measurements with KATRIN was proven [Gro11, Gro13].

The commissioning of this cooling system in its final setup and temperature measurements with focus on the following points are the objectives of this work:

- Improvements on and final commissioning of the WGTS beam tube temperature measurement system for KATRIN operation.
- An extensive consideration of measurement uncertainties related to the temperature measurement system.
- Measurements of the temperature stability and homogeneity of the WGTS beam tube.

These tasks are reflected by the structure of this thesis. A short overview over β-spectroscopy in general and at KATRIN in particular is given at the beginning of chapter 2. Following that, the focus is placed on the WGTS and its requirements for the neutrino measurement before going into the detail about the beam tube cooling system and temperature measurement system. This chapter is concluded by stating the concrete experimental objectives of this thesis. In chapter 3 the structure of the temperature measurement system as well as its calibration procedure are described. Achieved results with regard to the uncertainty and reproducibility of the calibration are shown. Measurement results of the temperature stability and homogeneity of the beam tube are presented in chapter 4 and their impact on the KATRIN neutrino mass measurement are discussed in detail. A summary of the achievements accomplished over the course of this thesis and an outlook on the timeline of KATRIN for the near future with regard to measurements important for the WGTS is given in chapter 5.

2. WGTS – The β-electron source of the Karlsruhe Tritium Neutrino Experiment

The Karlsruhe Tritium Neutrino Experiment (KATRIN) aims to determine the neutrino mass by high accuracy energy spectroscopy of electrons produced in the β-decay of tritium molecules. It is currently being commissioned at the Karlsruhe Institute of Technology and has been designed to achieve a sensitivity on the neutrino mass of $m(\nu_\mathrm{e}) = 200\,\mathrm{meV}/c^2$ (90 % C. L.) which corresponds to a $5\,\sigma$ discovery potential of $m(\nu_\mathrm{e}) = 350\,\mathrm{meV}/c^2$ [Ang05].
In this chapter the working principle of the KATRIN experiment is explained with a focus on its electron source. The β-decay spectroscopy approach of neutrino mass measurements is shortly summarized in section 2.1 and the detailed implemtation of that approach in the KATRIN experiment is described in section 2.2. Following that, section 2.3 describes the electron source of KATRIN, the WGTS, in more detail and discusses some of the requirements it needs to fulfill. The temperature related requirements necessitate a temperature stabilization whose principle and realization are explained in section 2.4. Finally, the objectives of this thesis are stated in section 2.5.

2.1. Neutrino mass measurement via energy spectroscopy of β-decay electrons

Due to the fact that neutrinos only interact very rarely with matter in interactions via the weak force, observing neutrinos directly is challenging. To date it has only been done for relativistic neutrinos with kinetic energies above 150 keV [Bel14]. This exceeds the current best 95 % C. L. limits on the direct measurement of the neutrino rest mass of around $2\,\mathrm{eV}/c^2$ ($2.3\,\mathrm{eV}/c^2$ [Kra05], $2.05\,\mathrm{eV}/c^2$ [Ase11]) by several orders of magnitude.
This problem of being unable to detect non-relativistic neutrinos leads to the fact that that neutrino mass measurement experiments need to derive the neutrino mass from an observable easier to measure. One such approach is the high-resolution energy spectroscopy of electrons produced by β-decay. In this method, a neutron inside an atom, with atomic mass m and atomic number n, decays into a proton while emitting an electron and an electron antineutrino [Ott08]:

$$(A, Z) \rightarrow (A, Z+1)^+ + \mathrm{e}^- + \bar{\nu}_\mathrm{e}\ . \tag{2.1}$$

In this decay, the mass difference between the atoms (A, Z) and $(A, Z+1)$, Q, is converted to and split between the kinetic energy of the recoiling atom $(A, Z+1)^+$, E_{rec}, the electron E_β, the electron antineutrino E_ν, and the excitation of a final state of the daughter atom with energy V_j:

$$\Big(m((A,Z)) - m((A,Z+1)^+)\Big) \cdot c^2 = Q - V_j \ , \tag{2.2}$$

$$Q = E_{\mathrm{rec}} + E_\beta + E_\nu + V_j \ . \tag{2.3}$$

As this decay is a three-body decay, the distribution of Q between the three constituents is not fixed to constant values for E_{rec}, E_β and E_ν, but given by a continuous distribution. The complete energy spectrum of an electron, $\gamma(\epsilon) = \frac{\mathrm{d}\Gamma}{\mathrm{d}E}$ with $\epsilon := E_0 - E$, emitted in the β-decay of an atom with charge Z, has been calculated by Fermi [Fer34] and can be expressed after [Ott08] as:

$$\begin{aligned}\gamma(\epsilon) =& \frac{G_\mathrm{F} \cos^2 \Theta_\mathrm{C}}{2\pi^3} \left|M_{\mathrm{nuc}}\right|^2 F \cdot (E_0 + m_\mathrm{e} c^2 - \epsilon) \\ &\cdot \sqrt{(E_0 + m_\mathrm{e} c^2 - \epsilon)^2 - m_\mathrm{e}^2 c^4} \sum_{i,j} \left|U_{\mathrm{e}i}\right|^2 P_j \cdot (\epsilon - V_j) \\ &\cdot \sqrt{(\epsilon - V_j)^2 - m_i^2 c^4} \cdot \Theta(\epsilon - V_j - m_i^2 c^4) \ ,\end{aligned} \tag{2.4}$$

with:

- the kinetic energy of the emitted electron $E = E_0 - \epsilon$,
- the endpoint energy $E_0 = Q - E_{\mathrm{rec}}$ of an energy spectrum with a vanishing neutrino mass ($m_\nu = 0\,\mathrm{eV}/c^2$) and the daughter atom in its ground state ($V_j = V_0 = 0$),
- the speed of light c,
- the Fermi constant G_F,
- the Cabbibo angle Θ_C,
- the nuclear Matrix element $M_{\mathrm{nuc}}(E)$,
- the Fermi function F,
- the electron rest mass m_e,
- the mass of the i-th neutrino mass eigenstate m_i,
- entries of the PMNS-Matrix $\left|U_{\mathrm{e}i}\right|^2$,
- the probability for the daughter atom to be in the j-th excited final state P_j,
- and the Heaviside function representing the conservation of energy $\Theta(\epsilon - V_j - m_i^2)$.

From the above equation it can be derived that the influence of a small, non-vanishing neutrino mass is only visible in a region near the endpoint energy E_0. A non-vanishing neutrino mass shifts the endpoint energy to $E_0' = E_0 - m_\nu/c^2$ (see figure 2.1) and changes the spectral shape in the endpoint region with the largest effect at about $3.5\,\mathrm{eV}/c^2$ below the endpoint for tritium beta decay and an assumed neutrino mass of $0.5\,\mathrm{eV}/c^2$ [Ott08]. As has been shown through multiple neutrino oscillation experiments like SNO, Super-Kamiokande or MINOS [Fuk98, Suz99, Nak00, Ahm01, Mic06], neutrino flavor and neutrino mass eigenstates do not match up in a trivial manner. Each of the three

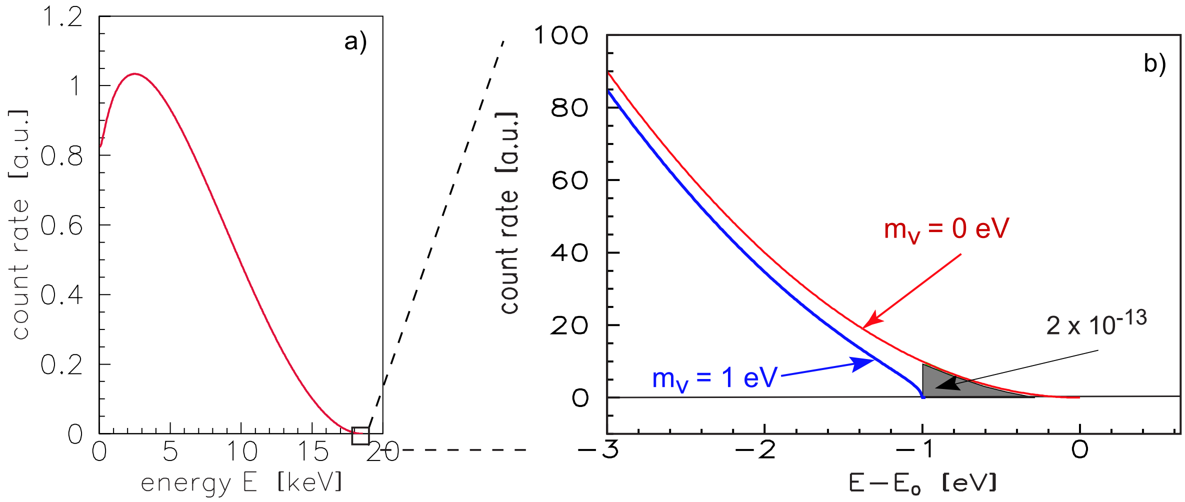

Figure 2.1.: Influence of the neutrino mass on the β-spectrum of tritium. Shown in a) are two calculated β-spectra of tritium for neutrino masses of $0\,\mathrm{eV}/c^2$ and $1\,\mathrm{eV}/c^2$ with the end point region magnified in b). The β-spectra differ in a shift of the endpoint by the neutrino rest mass of $1\,\mathrm{eV}/c^2$ and in a decrease in the count rate for energies below this value. Only a tiny fraction of $2 \cdot 10^{-13}$ of all decays produces electrons with energies between the different endpoint energies. Image from [Osi01].

flavor eigenstates is a mixture of the three mass eigenstates and vice versa.
Since the antineutrinos in β-decay are produced in their flavor eigenstate ν_e, the probabilities for the antineutrinos to be produced in a certain mass eigenstate ν_i are given by the PMNS matrix elements $|U_{\mathrm{e}i}^2|$ [Pon58, Mak62]:

$$\begin{pmatrix} \nu_\mathrm{e} \\ \nu_\mu \\ \nu_\tau \end{pmatrix} = \begin{pmatrix} U_{\mathrm{e}i} & U_{\mathrm{e}i} & U_{\mathrm{e}i} \\ U_{\mathrm{e}i} & U_{\mathrm{e}i} & U_{\mathrm{e}i} \\ U_{\mathrm{e}i} & U_{\mathrm{e}i} & U_{\mathrm{e}i} \end{pmatrix} \times \begin{pmatrix} \nu_1 \\ \nu_2 \\ \nu_3 \end{pmatrix} . \tag{2.5}$$

In practice, the mass splittings of neutrino eigenstates [For14, Ada08]

$$|\Delta m_{21}^2| = 7.6^{+0.19}_{-0.18} \cdot 10^{-5}\,\mathrm{eV}^2/c^4 \ , \tag{2.6}$$

$$|\Delta m_{23}^2| = 2.74^{+0.44}_{-0.26} \cdot 10^{-3}\,\mathrm{eV}^2/c^4 \ , \tag{2.7}$$

and

Normal hierarchy ($m_1 < m_2 < m_3$):

$$|\Delta m_{31}^2| = 2.48^{+0.05}_{-0.07} \cdot 10^{-3}\,\mathrm{eV}^2/c^4 \ , \tag{2.8}$$

Inverted hierarchy ($m_3 < m_1 < m_2$):

$$|\Delta m_{31}^2| = 2.38^{+0.05}_{-0.06} \cdot 10^{-3}\,\mathrm{eV}^2/c^4 \ , \tag{2.9}$$

found through neutrino oscillation experiments are small compared to the energy resolution of modern spectrometers for β-spectroscopy. Even with the unprecedented sensitivity of KATRIN, these splittings cannot be resolved, so this type of experiment is currently only sensitive to the incoherent sum of the mass eigenstates [Dre13]:

$$m(\nu_{\mathrm{e}})^2 = \sum_i \left|U_{\mathrm{e}i}^2\right| m(\nu_i)^2 \ . \tag{2.10}$$

Due to the fact that β-spectroscopy is a purely kinematic process, it is model-independent [Ang05]. As a result, the nature of neutrinos, whether they are Dirac or Majorana particles, cannot be probed. In comparison, neutrinoless double-β-decay is sensitive to the coherent sum of the mass eigenstates [Ell04]:

$$\langle m_{\beta\beta} \rangle = \left| \sum_i m_i U_{\mathrm{e}i}^2 \right| \ . \tag{2.11}$$

Here, $U_{\mathrm{e}i}$ contains two additional phases, which can allow destructive interference to occur. This effective mass only exists if neutrinos are Majorana particles.

2.2. The Karlsruhe Tritium Neutrino Experiment

The Karlsruhe Tritium Neutrino Experiment uses the β-decay of tritium molecules ($\mathrm{T_2}$) to measure the neutrino mass with a $5\,\sigma$ discovery potential of $m(\nu_{\mathrm{e}}) = 350\,\mathrm{meV}/c^2$ [Ang05]. Tritium is particularly suitable as a β-electron emitter for neutrino mass measurements for a multitude of reasons:

- The β-decay of tritium is super-allowed, which leads to a comparatively short half-life of 12.3 yr [Luc00]. This makes a high-intensity source using only a moderate amount of tritium possible. Since this decay is super-allowed, the matrix element M_{nuc} is constant [Alt03], which simplifies the analysis.
- The simple structure of tritium and $\mathrm{T_2}$ molecules allows for a detailed and quantitative theoretical calculation of the decay process and the final state distribution of the daughter molecule [Sae00, Bod15].
- The comparatively low Q value of approximately 18.6 keV [Mye15] is favorable, as a high sensitivity on the neutrino mass requires a low endpoint energy of the β-decay [Dre13].

To achieve the KATRIN goal of improving the sensitivity on the neutrino mass by one order of magnitude compared to the current best 95 % C. L. limit of $<2.0\,\mathrm{eV}/c^2$ (combined from $2.3\,\mathrm{eV}/c^2$ [Kra05] and $2.05\,\mathrm{eV}/c^2$ [Ase11]), this choice of the β-electron emitter leads to several requirements for the KATRIN experiment [Ang05]:

- a source activity on the order of 10^{11} Bq is required to reach the necessary statistical uncertainty within a given measurement frame of 3 years,
- a spectrometer with a resolution on the order of 1 eV at 18.6 keV is needed to measure the deviation from the spectrum of a massless neutrino,
- systematic effects on the endpoint of the spectrum have to be identified, characterized, considered, and minimized to reduce systematic uncertainties to the required level.

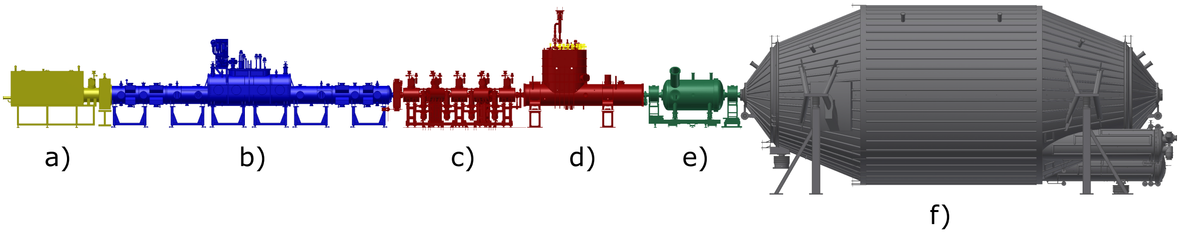

Figure 2.2.: Beam line of the KATRIN experiment. Electrons are produced via β-decay of tritium in the Windowless Gaseous Tritium Source (WGTS) (b) on the left. Important source parameters such as the activity are monitored by the Rear Section (RS) (a). Electrons leaving the WGTS are guided adiabatically by a magnetic field through the Differential Pumping Section (DPS) (c) and Cryogenic Pumping Section (CPS) (d) which reduce the tritium flux into the spectrometers by 14 orders of magnitude. After the CPS, the electrons enter the Pre-Spectrometer (PS) (e) which is set to a potential of around −18.3 kV, allowing only electrons with a high kinetic energy to pass into the main spectrometer (f). The main spectrometer then analyzes the kinetic energy of the electrons with a resolution of 0.93 eV, allowing only electrons with kinetic energy exceeding the analyzing potential of around 18.6 keV (−30 eV to 5 eV around the endpoint of the tritium decay) to reach the Detector (not shown). Image used by KATRIN collaboration.

To fulfill these requirements, the KATRIN Experiment was designed [Ang05] based on the prior research at Mainz [Kra05] and Troitsk [Ase11]. In comparison, KATRIN has been scaled up by a factor of 100 to improve the neutrino mass sensitivity by a factor of 10 (from 2 eV down to 0.2 eV) as the mass enters equation 2.4 squared. This means that statistics as well as systematic uncertainties and background have to be improved by a factor of 100.

An overview of the KATRIN Experiment and a description of its components can be found in figure 2.2. The type of spectrometer employed by KATRIN is a so called MAC-E-Filter, which stands for *Magnetic Adiabatic Collimation combined with an Electrostatic Filter*, and was first proposed in [Lob85]. The principle of a MAC-E-Filter, schematically shown in figure 2.3, is the adiabatic guiding of electrons to run against an electrostatic potential, which reflects all the electrons with kinetic energies below that potential. This is achieved by a magnetic field along the KATRIN beam line, which forces the electrons to perform a cyclotron motion around the magnetic field lines. The spectrometer is designed in a way that there is a gradient of the magnetic field with the maximal field strength B_{max} at both ends, and the minimal magnetic field strength B_{min} in the center of the spectrometer. The field strength needs to be chosen in such a way that the electrons are confined to their cyclotron motion around a specific field line at any point.
In addition, an electrostatic field is applied along the spectrometer. This field intensity has a gradient shaped inversely compared to that of the magnetic field [Ott08]. Its field strength peaks in the center of the spectrometer, the analyzing plane, and falls off towards both ends. The electrostatic potential at the analyzing plane is called analyzing potential.
This setup ensures that most of the kinetic energy of the electrons is transformed adiabatically from their cyclotron motion (with energy $E_\perp$) to their longitudinal motion (with energy $E_\|$) against the analyzing potential as can be seen in the lower section of

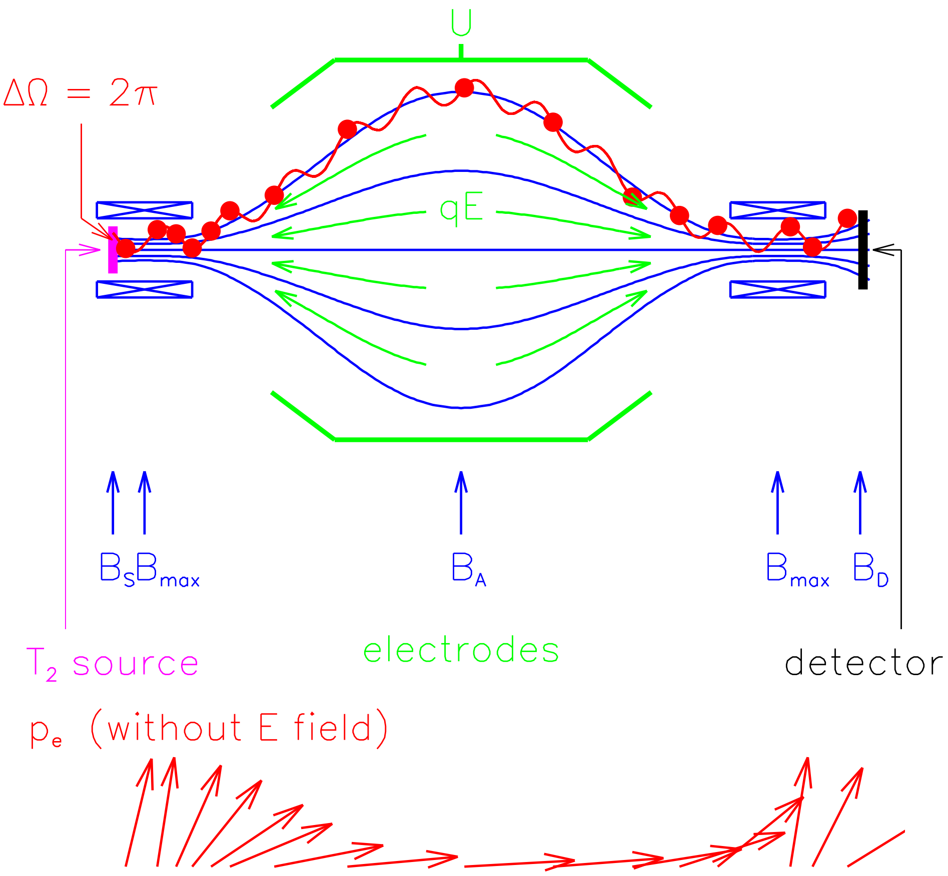

Figure 2.3.: Schematic of a MAC-E-Filter. A MAC-E filter combines a magnetic field gradient with a electrostatic retarding potential to work as a high pass filter with a high energy resolution. For details, see main text. Image from [Ang05].

figure 2.3. This transformation keeps the magnetic moment μ constant:

$$\mu = \frac{E_\perp}{B} = \text{const.} \ . \tag{2.12}$$

This causes $E_\perp$ to decrease with decreasing magnetic field B, and since the transformation is adiabatic $E_\parallel$ increases accordingly. As such, only electrons with kinetic energies exceeding this potential can pass the analyzing plane.
After passing the analyzing plane, the electrons are reaccelerated by the electrostatic field to their original energy and adiabatically guided by the magnetic field towards the exit of the spectrometer.

The energy resolution of a MAC-E-Filter is given by the difference in the magnetic field strength of B_{min} and B_{max} [Ang05]:

$$\frac{\Delta E}{E} = \frac{B_{\text{min}}}{B_{\text{max}}} \ . \tag{2.13}$$

For the KATRIN ratio of $B_{\text{max}} = 20000 \cdot B_{\text{min}}$ ($B_{\text{max}} = 6\,\text{T}$, $B_{\text{min}} = 3\,\text{G}$) and the tritium endpoint energy of about 18.6 keV, this leads to a resolution of $\Delta E = 0.93\,\text{eV}$ [Ang05].

To make full use of the analyzing capabilities of the KATRIN spectrometer, the electron source of KATRIN has to provide a high activity while tightly controlling systematic effects. Therefore, a windowless and gaseous source has been chosen: the WGTS.

2.3. The Windowless Gaseous Tritium Source

As explained in section 2.1, tritium is a nuclid particularly well suited as a source for β-electrons for neutrino mass measurement. Previous tritium β-spectroscopy experiments in Mainz [Kra05] and Troitsk [Ase11] used different source designs.

The source used at Mainz was a quench condensed tritium source (QCTS) [Wei99] consisting of tritium frozen to a highly oriented pyrolytic graphite (HOPG) substrate. Charging effects that can lead to a shift of the endpoint energy by up to several eV have been observed with this source [Bor03]. It was calculated that these charging effects would lead to unacceptably large systematic uncertainties with a source scaled to the target source activity of KATRIN.

The windowless gaseous tritium source (WGTS) used at Troitsk [Lob00] did not show effects that would prevent the upscaling of the source. Therefore, a WGTS was chosen as the source for the KATRIN experiment.

In this section, the working principle of a windowless gaseous tritium source is explained in subsection 2.3.1. The physical and technical requirements on the WGTS resulting from the specified KATRIN sensitivity of $0.2\,\text{eV}/c^2$ are discussed in subsection 2.3.2.

2.3.1. Principle of the WGTS

A windowless gaseous tritium source, as first built by the Los Alamos National Laboratory [Wil87, Rob91], consists of a gas column of molecular tritium T_2 inside a strong magnetic field of several Tesla.

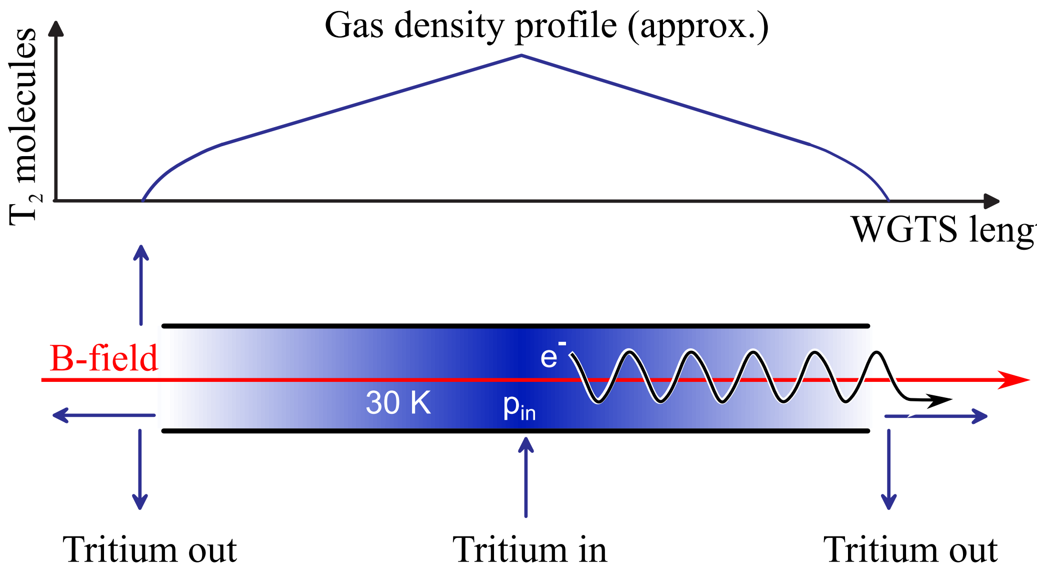

Figure 2.4.: Schematic gas flow through the WGTS. Gaseous tritium is injected at the center and pumped out at both ends of the WGTS. This causes the non-linear density profile shown at the top to form.

As shown in figure 2.4, gaseous tritium is injected in the center of a tube of several meters length and several centimeters diameter (3 m and 20 mm in case of the Troitsk experiment [Lob00, Lob02], 10 m and 90 mm for KATRIN [Bab12]), and streams towards both ends of the tube, where it is pumped out. Electrons produced by β-decay of the tritium molecules are confined by the magnetic field. They are forced to perform a cyclotron motion around individual magnetic field lines oriented along the WGTS axis. As the name suggests, a WGTS setup is windowless, and therefore the electrons do not need to pass a barrier on their way out of the source, which would have an impact on their energy. Therefore, this construction is able to adiabatically guide β-electrons towards the spectrometer. The adiabacity of a WGTS is limited by electron scattering, as is shown in the following section.

2.3.2. Physical and technical requirements

The ambitious target of improving the sensitivity on the neutrino mass by one order of magnitude, which the KATRIN experiment has set for itself, defines strict requirements, as the neutrino mass enters the β-spectrum squared, see equation 2.4. This means that improving the sensitivity by a factor of 10 requires an improvement of all experimental uncertainties as well as of the statistical uncertainty by a factor of 100.

To minimize the statistical uncertainty, a high source activity is needed. The source activity depends on the number N_{T_2} of tritium atoms inside the source, which is given by:

$$N_{\mathrm{T}_2} = \rho d \cdot A \cdot \epsilon_{\mathrm{T}_2} \ . \tag{2.14}$$

Here, A is the cross-section of the WGTS beam tube, ϵ_{T_2} the percentage of tritium atoms in the injected gas, and ρd the column density of gas inside the source. For a fixed cross-section A, the source activity can be raised by increasing the purity of the gas ϵ_{T_2} and the column density ρd. While increasing ϵ_{T_2} is dependent on and limited by the tritium processing system outside of the WGTS, the column density ρd is limited by scattering.

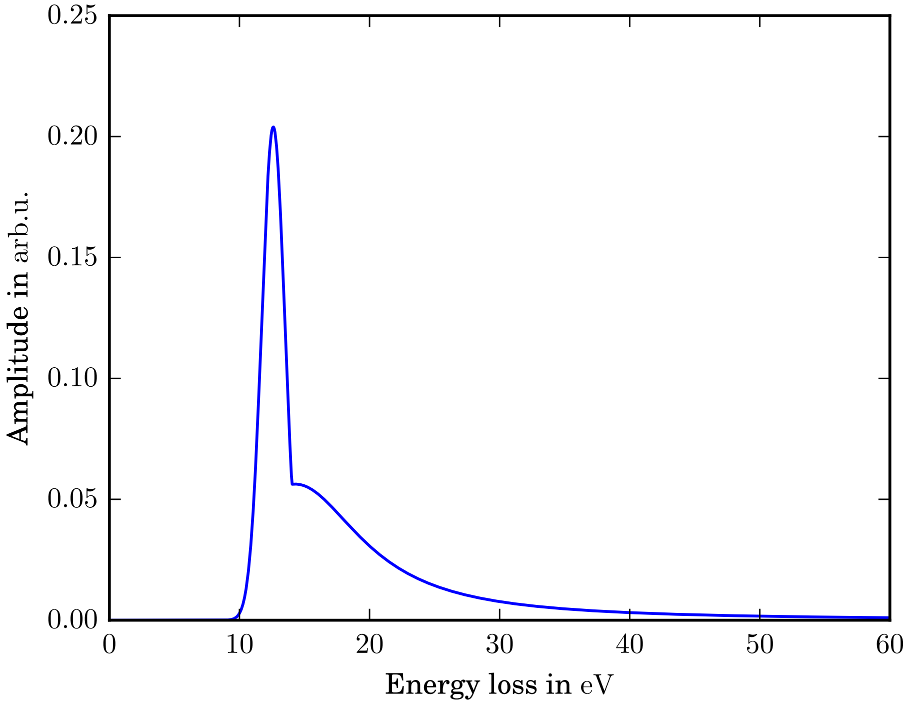

Figure 2.5.: Spectrum of energy loss due to electron tritium scattering. Shown is a spectrum of scattering amplitude over electron energy loss for a single interaction between an electron and a tritium molecule. Data taken from [Ase00]

As the column density ρd increases with the pressure of gas inside the WGTS, so does the probability for β-electrons to scatter with gas inside the WGTS. Scattered electrons lose energy (see figure 2.5), which leads to a decrease in the measured rate of electrons with energies near the endpoint of the β-spectrum. This effect is an important systematic uncertainty on the measurement of the neutrino mass [Ase00, Han17]. A reference value of $\rho d = 5 \cdot 10^{17}$ molecules/cm^2 has been calculated as an optimum of high source activity versus low systematic uncertainty for nominal KATRIN operation. For a single measurement interval of 1 h, the activity of the source has to be stable to 0.1 %. It is therefore necessary to stabilize the column density to a level of $\Delta\rho d/\rho d = 2 \cdot 10^{-3}$/h as well as the purity ϵ_{T_2} to 0.1 %/h to achieve the KATRIN target 95 % C. L. sensitivity of 200 meV/c^2 [Ang05].

The source activity can be directly measured via spectroscopy of β-induced x-rays (BIXS). This measurement uses the bremsstrahlung produced by β-electrons from the WGTS hitting the rear side boundary of the KATRIN vacuum system called *rear wall*. The planned BIXS system for KATRIN will need ∼150 s at the nominal source activity to reach the required precision of 0.1 % [Bab12].

The total column density ρd will be monitored periodically off-line by a quasi-mono-energetic electron source with a small energy spread of 0.35 eV called *e-gun* [Val11], which is part of the Rear Section (see section 2.2). Electrons produced by the e-gun are guided into the rear end of the WGTS, pass through the tritium gas inside it, and are then guided towards the spectrometer. As the scattering probability of electrons inside the source is correlated with the column density, the rate of detected versus produced electrons originating from the e-gun allows a determination of the column density with the necessary accuracy of <0.1 %.

Both methods mentioned above are only sensitive to the total activity and column density inside the source. This alone is not sufficient though, as β-electrons emitted at different points inside the WGTS need to pass through a different amount of gas before leaving the WGTS. As the scattering probability is dependent on the effective column density at a given point of the WGTS, it is necessary to know not only the total column density, but also the density profile of gas inside the WGTS. This density profile also needs to be have a relative stability of $2 \cdot 10^{-3}$/h [Ang05]. It is influenced by several factors:

- the inlet pressure of tritium gas into the beam tube,
- the pumping performance at both ends of the beam tube,
- and the temperature of the beam tube.

These factors, combined with the purity, need to be stabilized on a 0.1 %/h level [Ang05]. A short overview of their importance and achieved results in regards to the stability is given in the following.

Purity In practice, the gas injected into the WGTS will not be pure molecular tritium T_2, but also contain trace amounts of other gases, mainly consisting of other hydrogen isotopologues. The gas composition is therefore monitored continuously by the Laser Raman (LARA) system [Fis14, Sch15] to achieve the target of 95 % purity with a relative stability of 10^{-3} [Ang05]. An experiment simulating KATRIN conditions has achieved the requirements [Fis11].

Inlet pressure In order for the gas density profile to be stable on a 0.1 %/h level, the injection pressure of tritium into the WGTS has to be stable on a level better than 0.1 %/h. Measurements have been done with a dummy pipe in place of the WGTS beam tube. In these measurements, the required stability has been achieved [Pri15].

Pumping performance Similar to the inlet pressure, the pumping performance at both ends of the WGTS has to be stable on a 0.1 %/h level. As long as the gas load on the used Oerlikon Leybold MAG W2800 turbomolecular pumps is constant, so is their pumping performance on a level better than 0.1 %/h [Pri17]. Extensive testing of the long term compatibility of these pumps and possible aging effects due to contact with tritium has been done, but no adverse impact for KATRIN operation could be found [Pri13].

Beam tube temperature The temperature of the beam tube is of special importance, as it influences several other systematic effects on the neutrino mass, and necessitates the specialized cryostat design shown in subsection 2.4.1. Therefore, temperature related effects and resulting requirements are discussed in detail in the following.

The effects depending on beam tube temperature are:

- the motion of tritium molecules towards the pumps inducing a Doppler broadening of the electron energy,
- the formation of tritium molecule clusters at low temperatures,
- the conductance of the beam tube, as higher temperatures necessitate a higher rate of tritium mass flow,

- and the tritium molecule final states,
- condensation of tritium in the beam tube below 27 K [Bor06].

These effects put restrictions on the temperature of the tritium. As the tritium thermalizes after contact with the beam tube wall [Geh08], the parameter that needs to be measured and stabilized experimentally is the beam tube temperature. Therefore, the restrictions on the tritium temperature lead to an optimal temperature range of the beam tube temperature for KATRIN operation. These restrictions arise from the above effects as follows.

Doppler effect

Tritium molecules injected into the WGTS beam tube stream towards both ends in a free molecular flow. If the motion of a molecule is directed towards the detector at the time of decay, the kinetic energy of the emitted electron E_{e} is the sum of the electron's kinetic energy E_{kin} before the decay and the energy of the β-decay E_{β}. If the motion is directed away from the detector, E_{kin} is subtracted from E_{β}. An illustration of the effect for emission of mono-energetic electrons is shown in figure 2.6. As the energy of the β-decay is given by a continuous distribution, the energy measured by the detector E_{e} is a superposition of the E_{kin}-distribution onto the energy of the β-decay E_{β}.

This effect can be calculated and deconvolved from the β-spectrum accordingly if the temperature of the beam tube is sufficiently homogeneous and accurately known with a trueness of 0.5 K [Bab12]. As the width of the broadening induced by this effect is proportional to $\sqrt{T}$ [Cha71], it is favorable to reduce the uncertainty coming from this effect by lowering the temperature of the beam tube as much as possible.

Tritium clusters

At low temperatures hydrogen H_2 molecules are known to form molecular dimer clusters and their potential energy well depths[1] have been calculated ab-initio to be between 16.8 K and 41.3 K [Hye12]. Comparable energy well depths are projected to be found for tritium T_2 dimers [Gro17]. A detailed investigation by Groeßle et. al. into the binding energies of tritium clusters via infrared absorption spectroscopy is underway.

The formation of tritium clusters poses a problem as the β-decay of a tritium atom inside a cluster has distinctly different final states than the β-decay of a tritium atom inside a singular tritium molecule, which can be assumed to be uninfluenced by the surrounding tritium molecules. As not only T_2 dimers, but a multitude of clusters with different constituents such as other hydrogen isotopologues (e.g. HT, DT) can be created, cluster formation induces an uncontrollable systematic uncertainty on the neutrino mass measurement.

As the probability for tritium molecules to be bound in clusters decreases towards higher temperatures, higher temperatures are favorable to reduce uncertainties on the neutrino mass measurement due to tritium clusters.

[1] Potential energy well depth here means the potential difference between the minimum of the potential and the unbound state.

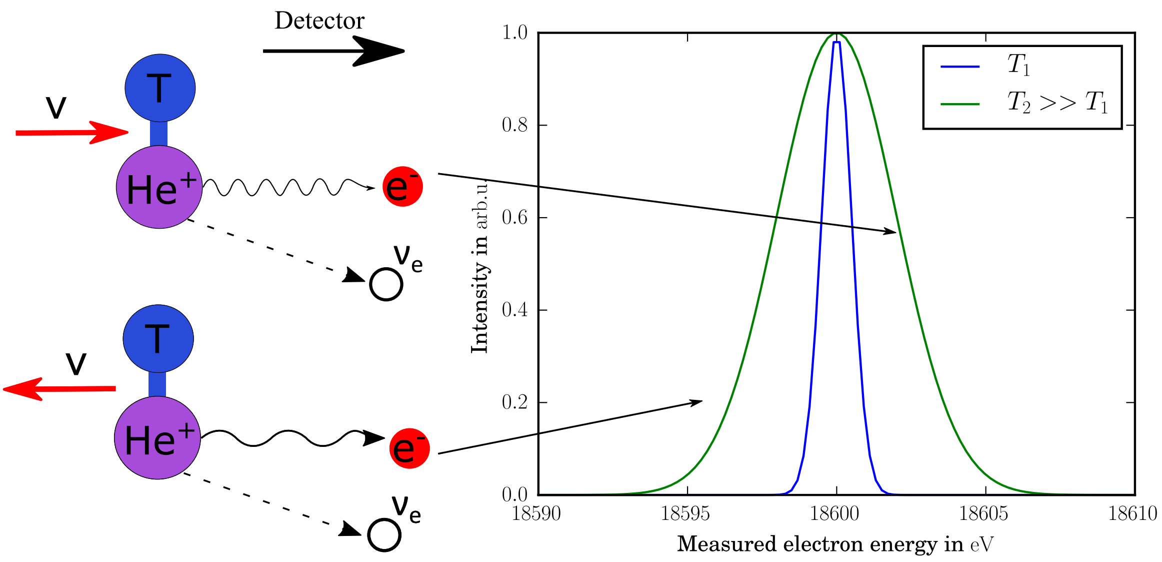

Figure 2.6.: Illustration of Doppler broadening. Shown is the Doppler effect on mono-energetic electrons with a kinetic energy of 18.6 keV. The Doppler effect causes a broadening of the measured electron energy. The magnitude of this effect depends on the bulk velocity of the decaying tritium. For the freely streaming tritium gas inside the WGTS beam tube, which is thermalized, this velocity is dictated by the temperature of the beam tube. Lower temperatures lead to a smaller Doppler-broadening which, makes low temperatures of the beam tube favorable for KATRIN operation.

Final States

A part of the tritium β-decay energy can excite the daughter molecule into an excited final state. The β-electron is missing this energy used to lift the daughter molecule into an excited state, which leads to an uncertainty on the neutrino mass measurement.

The distribution of those final states has been calculated down to the percent level in [Bod15]. With lower temperatures, the probability for the daughter molecule to be excited to final states with high energies decreases, and the probability for the daughter molecule to remain in the ground state increases. Therefore, it is favorable to operate the tritium source at low temperatures to reduce uncertainties due to the tritium molecular final states.

Summary

The column density has to be stable to a level of $\Delta\rho d/\rho d = 2 \cdot 10^{-3}/\mathrm{h}$, which leads to a requirement on the relative temperature stability of $\Delta T/T = 1 \cdot 10^{-3}/\mathrm{h}$ [Ang05]. To achieve the target KATRIN sensitivity, a homogeneous beam tube temperature on the order of 10^{-3} is necessary to keep uncertainties due to tritium final states and the Doppler effect at an acceptable level [Ang05].

The effect of Doppler broadening and the excited final states favor a low operation temperature of the WGTS. This is limited by the formation of tritium clusters at low temperatures and the condensation of tritium on the beam tube walls below 27 K [Bor06].

Table 2.1.: Requirements on the temperature of the WGTS beam tube. Values taken from [Bab12].

Parameter	Requirement
Temperature homogeneity	$< \pm 30\,\mathrm{mK}$
Temperature stability	$< \pm 30\,\mathrm{mK/h}$
Trueness of temperature measurement	$0.5\,\mathrm{K}$

These requirements have led to the decision of about 30 K for the operational temperature of the WGTS beam tube during KATRIN measurement [Ang05]. For this value, the technical temperature requirements are listed in table 2.1.

Reaching the required values of $\pm 30\,\mathrm{mK}$ temperature homogeneity of the beam tube and a temperature stability of $\pm 30\,\mathrm{mK/h}$ is a challenging task, which necessitated the specialized cryogenic system described in the following section 2.4.

2.4. Temperature stabilization of the WGTS beam tube

To achieve the requirements described in subsection 2.3.2, a sophisticated cryogenic system has to be employed to cool the WGTS beam tube down to a temperature of about 30 K. A short overview of the layered WGTS cryostat design is given in subsection 2.4.1. In subsection 2.4.2, the focus is placed on the main component which is designed to achieve the temperature requirements of the beam tube: the two-phase neon cooling system. To verify the achievement of these requirements, temperature sensors with a relative accuracy better than 10^{-3} are necessary. Due to the boundary conditions inside the WGTS cryostat, this requires a special setup of temperature sensors, which is described in subsection 2.4.3.

2.4.1. Overview of the WGTS cryostat

The WGTS cryostat is a layered cryogenic system, which cools down the WGTS beam tube as well as the superconducting solenoids needed to generate the necessary magnetic field (see section 2.1) inside the source. The WGTS cryostat, as seen in figure 2.7, has a total length of 16 m. The central 10 m contain the section of the beam tube made most important for the gas density profile. The remaining 3 m inside the cryostat on both sides house the differential pumping sections DPS1-F and DPS1-R in addition to the beam tube. The structure of the cryostat around it is important for the temperature of the central 10 m of the beam tube. A short overview of the cryostat design [Gro08] is given below.

As can be seen in figure 2.8, the hull of the WGTS cryostat is separated from the so called *outer shield* by an insulation vacuum chamber. This insulation vacuum reduces the heat load on the outer shield by allowing only heat transfer via radiation. This heat transfer via radiation is minimized by several layers of isolation films. The outer shield is cooled by a constant supply of liquid nitrogen (LN_2), which is provided from an external tank. The purpose of this shield is to minimize the heat transfer from the hull at room temperature to the *liquid helium vessel* containing the superconducting

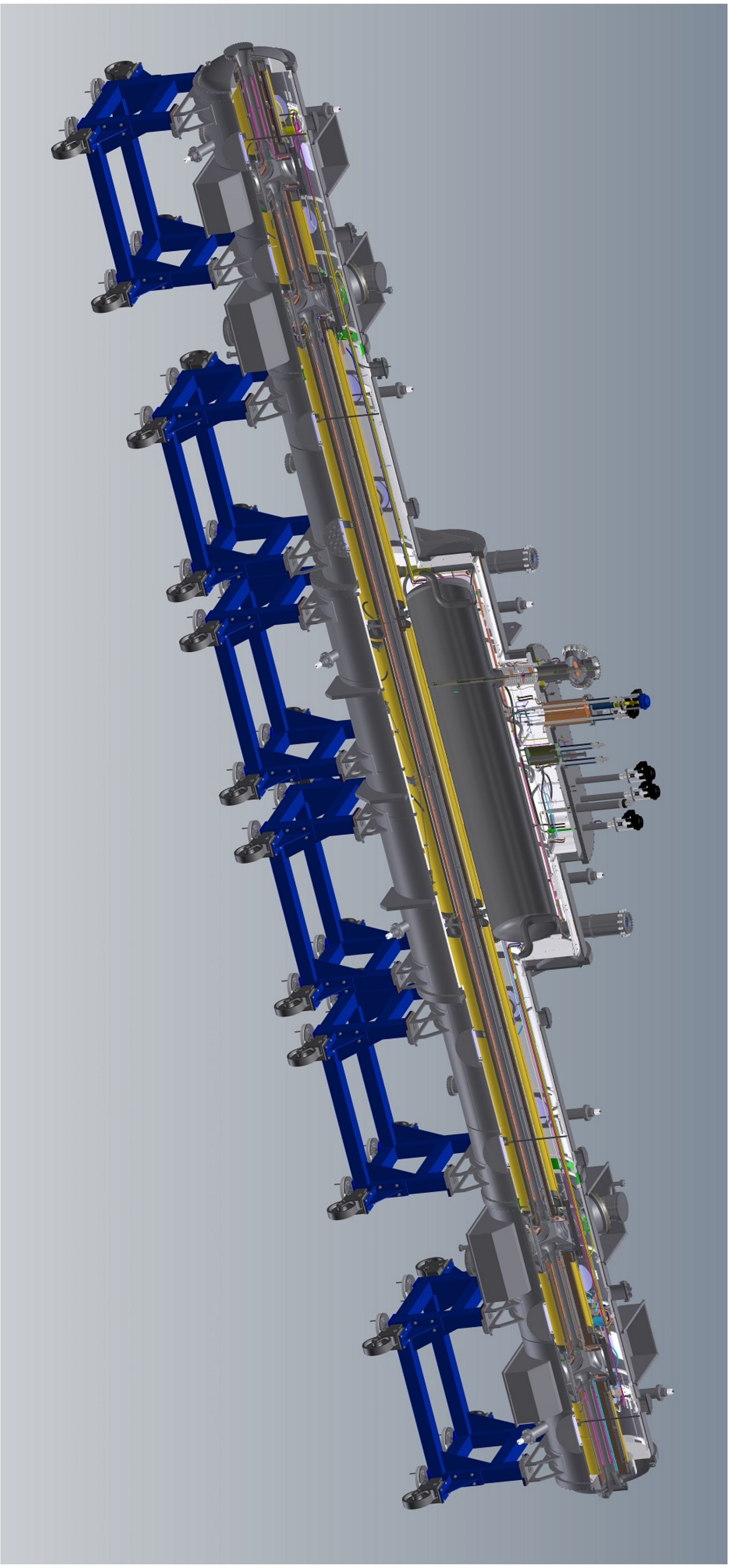

Figure 2.7.: Schematic WGTS cryostat. The section of beam tube important for the gas density profile is in the central 10 m of the cryostat, surrounded by the superconducting solenoids (here shown in yellow). Tritium is injected in the center of the beam tube and pumped out through the DPS1-F and DPS1-R on both ends. Image used by KATRIN collaboration.

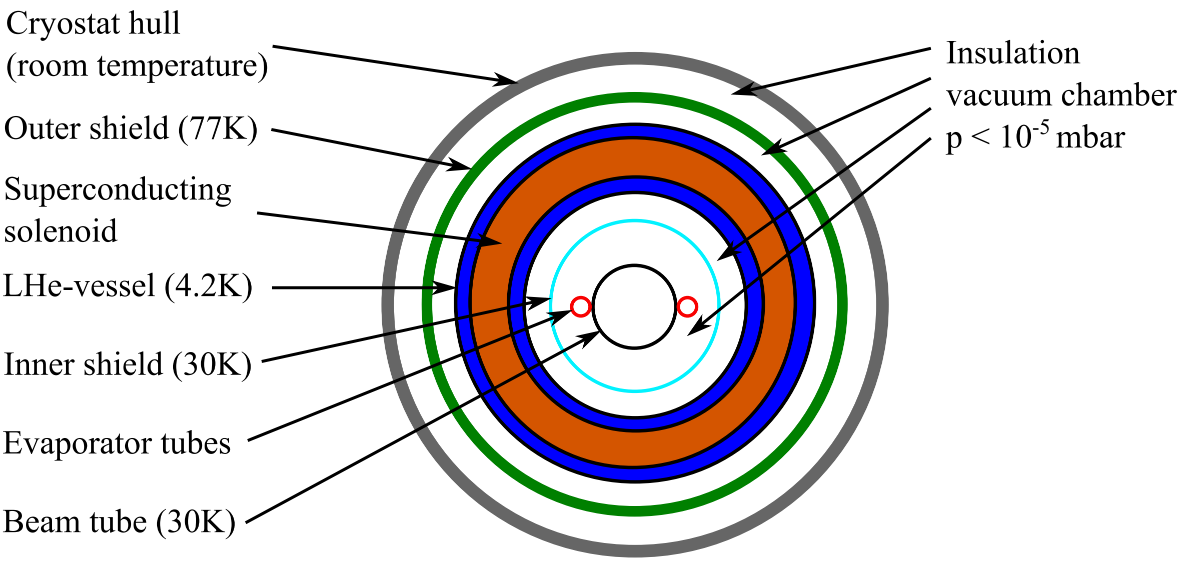

Figure 2.8.: Schematic cross-section of the WGTS cryostat. The WGTS consists of several layers of different cryogenic systems designed to shield the beam tube and cool down the superconducting solenoids.

solenoids. Due to the low temperatures of around 4.2 K, the superconducting solenoids need to operate at liquid helium is the only usable coolant. The liquid helium is provided by a refrigerating plant outside the laboratory.

As the temperature necessary to operate the superconducting solenoids is low enough that tritium would freeze, the beam tube needs to be shielded from the solenoid cooling system. The system accomplishing this is called the *inner shield*. As the inner shield is meant to reduce the heat load on the beam tube it, needs to be operated close to the required beam tube temperature of around 30 K. This is well below the freezing point of nitrogen, but above the boiling point of liquid helium, so gaseous helium is used as a coolant. As the refrigerating plant cannot directly produce gaseous helium with the required temperature, the stream of gaseous helium used to cool the inner shield is produced by mixing a low temperature stream of about 6 K with a high temperature stream of about 60 K. This mixing process leads to temperature fluctuations of approximately ±300 mK [Gro09], which is one order of magnitude more than the required beam tube stability of ±30 mK/h.

To still achieve the required stability, a cooling system using a two-phase mixture of neon is welded directly to the beam tube. This system is described in detail in the following subsection.

2.4.2. The two-phase cooling system

As mentioned in the previous subsection 2.4.1, the WGTS beam tube requires a specialized cooling system to achieve the required temperature stability of ±30 mK/h. For this purpose, a cooling system based on a thermosiphon containing a two-phase mixture of gaseous and liquid neon has been chosen [Gro09].

The two-phase cooling principle

In a closed two-phase system of a liquid and a gaseous phase in equilibrium, the first order phase transitions, evaporation and condensation, between the two phases occur at

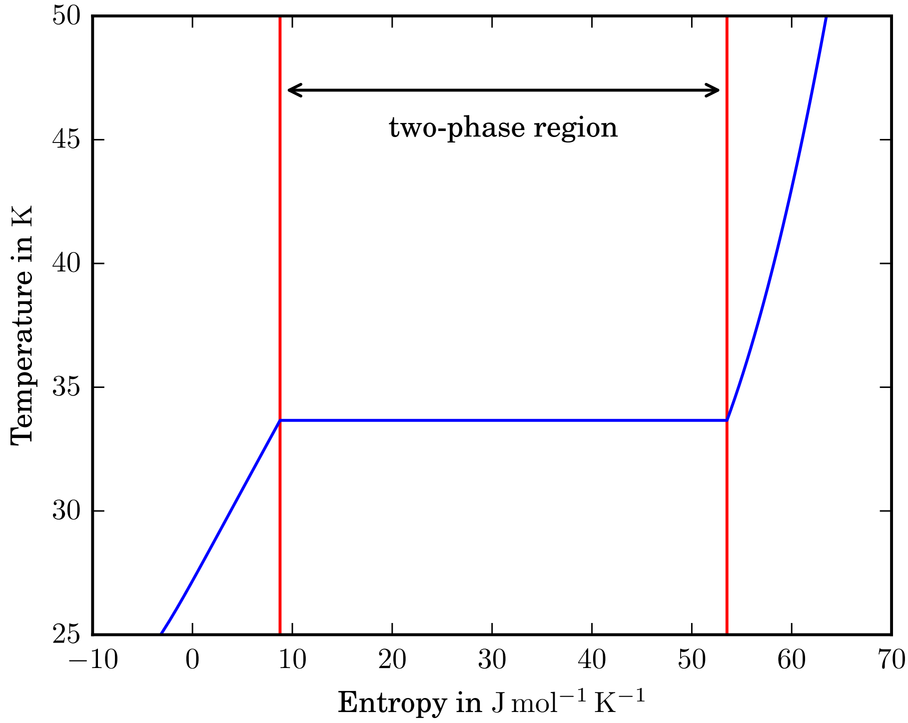

Figure 2.9.: Two-phase system temperature over entropy. Inside the two-phase region, the temperature of the system does not rise when further entropy in form of heat is brought into the system. This means that it can serve as cooling system with constant temperature. Data taken for neon at 5 bar from [Lin05].

an equal rate. Heat applied to such a system only shifts the ratio of liquid to gaseous phase, while the temperature of the system stays the same (see figure 2.9).

Therefore, as long as not all liquid has evaporated or all gas has condensed, a two-phase system is self-regulating its temperature. This temperature is given by the pressure inside the system via the saturation pressure curve (see figure 2.10) of the used substance. The stabilization achievable with this self-regulation is limited by the dimensions of the system, as the evaporation of a liquid inside a closed system leads to an increase in pressure. This pressure increase shifts the equilibrium and causes an increase in temperature. This effect is smaller for a given heat input, the bigger the volume of the system is, as the same amount of evaporated liquid leads to a smaller increase in pressure.

The two-phase cooling system

The realization of the two-phase thermosiphon cooling system for WGTS beam tube, as seen in figure 2.11, consists of the following (see figure 2.11):

- two evaporator tubes with a diameter of 16.8 mm,
- electrical heating elements,
- and a neon condenser.

The evaporator tubes form the core of the two-phase cooling system. During operation, they are filled with the mixture of gaseous and liquid neon. It has been calculated that

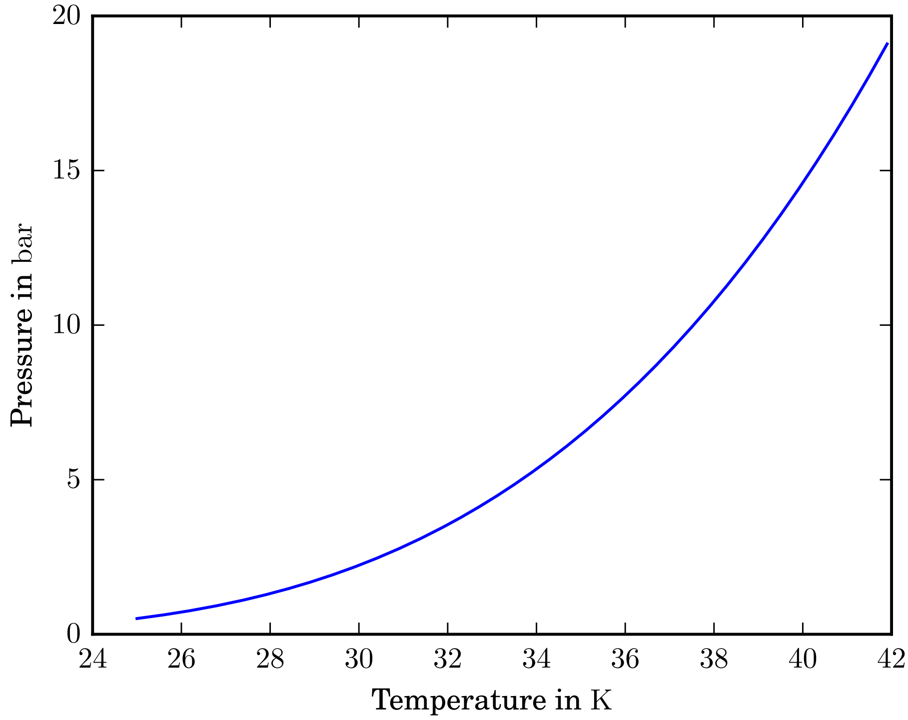

Figure 2.10.: Saturation vapor pressure curve of neon. Moderate pressures below 5 bar in the temperature region of the planned WGTS temperature of about 30 K make neon suitable for the use in a two-phase cooling system for the beam tube. Data taken from [Lin05].

the exact filling level of the evaporator tubes is not important. As long as the filling level is in the range of 4 mm to 12 mm, effects due to the filling level are not relevant [Gro09]. Evaporated neon streams into the condenser, which is cooled by the inner shield and thus is affected by the temperature fluctuations of the helium provided by the refrigeration plant. To dampen the temperature fluctuations of the gHe, the condenser contains a cold mass of 3.7 kg lead between the gHe and neon circuits [Gro09]. Four electrical heating elements with a maximal power of 2 W each are installed inside the evaporator tubes in pairs. Inside the evaporator tubes, the heaters each cover one half of the beam tube length, from the center to one end. They can be used to induce a heat load onto the system, shifting the ratio of liquid to gaseous phase. This leads to an increase of the pressure inside the evaporator tubes, which causes an increase in the temperature of the system. The temperature of the beam tube can be controlled by choosing the gHe temperature and heater power accordingly. An active regulation of the heater power, using the pressure inside the evaporator tubes as its process variable, has been put in place to increase the stability of the system.

Krypton mode

There is a special operation mode of KATRIN to perform an absolute calibration of the main spectrometer analyzing potential. In the so-called krypton mode, conversion electrons from a ^{83m}Kr source [Ang05] are used. As krypton would freeze at the nominal KATRIN operation temperature of around 30 K, the beam tube temperature needs to be raised to 100 K to 120 K. At these temperatures, argon will be used instead of neon as the coolant inside the two-phase system.

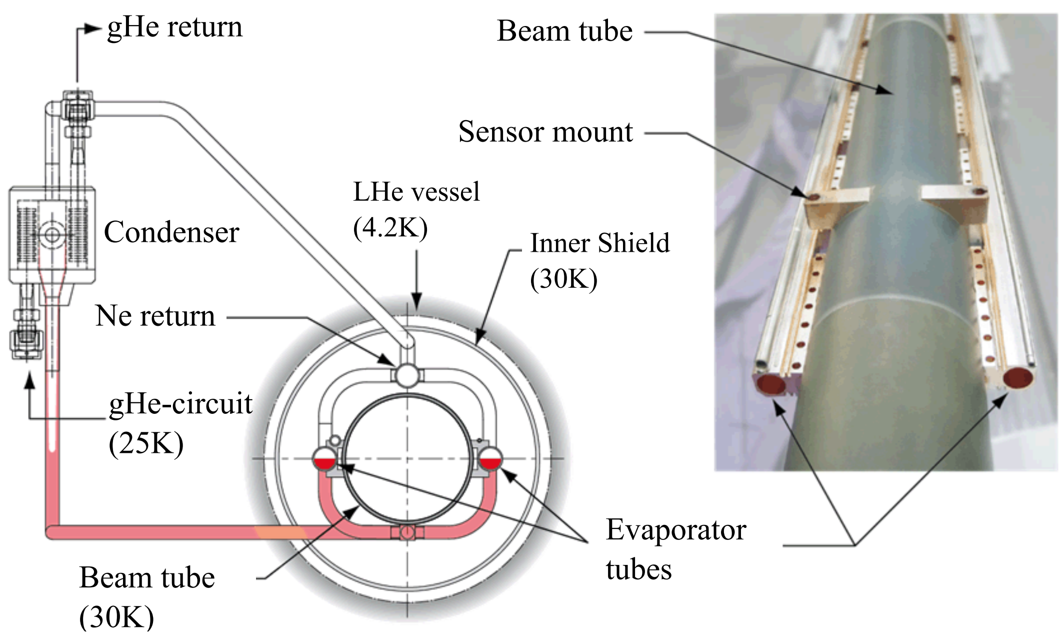

Figure 2.11.: Schematic depiction of the implemented two-phase neon cooling system. The evaporator tubes connected to the beam tube are filled halfway with liquid neon in nominal operation. Evaporating neon is liquefied in a condenser, which is cooled, over a lead cold mass as buffer, by a stream of gHe from the inner shield circuit. Electrical heaters inside the evaporator tubes regulate the pressure inside the system and thereby the temperature of the connected beam tube. Modified from image used by KATRIN Collaboration.

Demonstrator

The Demonstrator was a prototype of the WGTS cryostat and has been built to verify whether the design is viable for KATRIN.

In comparison to the final WGTS cryostat, the Demonstrator lacked the superconducting solenoids, which were replaced with dummy cold masses made from aluminum. The two-phase cooling system was only used for the central 10 m of beam tube, whereas the final WGTS cryostat also has two-phase cooling systems brazed to the beam tube inside the differential pumping sections DPS-1-F and DPS-1-R (see figure 2.7). Due to this, the Demonstrator only had one neon condenser connected to the inner shield instead of the three condensers in the final WGTS cryostat.

Measurements with this simplified structure have shown that the design is capable of fulfilling the requirements concerning temperature stability of the beam tube [Gro09]. It was also shown that the homogeneity requirements were not fulfilled and measures to remove or minimize the inhomogeneity in the final WGTS cryostat were taken. Details can be found in section 4.4. These measurements were taken with the temperature measurement system as described in the following subsection 2.4.3.

2.4.3. Temperature measurement system of the WGTS beam tube

The WGTS beam tube temperature along the central 10 m needs to be stabilized to ±30 mK/h and homogenized to ±30 mK to fulfill the KATRIN requirements. To verify

Table 2.2.: Temperature sensor types for the WGTS beam tube. Summary of calibration uncertainties of the studied sensor types. Only platinum, rhodium-iron, and the diode sensors are usable over the entire required temperature range. The diodes do not fulfill the accuracy requirement, while rhodium-iron sensors are not suitable for use in strong magnetic fields at low temperatures. Therefore platinum sensors have been chosen. Table after [Ram08].

	Temperature in K						
Sensor	4.2	10	20	77	300	400	500
Si-Diode	±12 mK	±12 mK	±14 mK	±22 mK	±32 mK	±45 mK	±50 mK
GaAlAs Diode	±12 mK	±12 mK	±14 mK	±22 mK	±32 mK	±45 mK	±50 mK
Cernox	±5 mK	±6 mK	±9 mK	±16 mK	±40 mK	±65 mK	-
Carbon-Glass	±4 mK	±5 mK	±8 mK	±25 mK	±105 mK	-	-
ROX	±16 mK	±18 mK	±37 mK	-	-	-	-
Rhodium-Iron	±7 mK	±8 mK	±10 mK	±13 mK	±23 mK	±41 mK	±46 mK
Platinum	-	-	±10 mK	±12 mK	±23 mK	±40 mK	±46 mK
Germanium	±4 mK	±5 mK	±8 mK	±30 mK	-	-	-

whether this is the case, temperature sensors distributed along the beam tube must have an accuracy of even better than 10 mK at 30 K [Ram08].

This accuracy is achievable with a wide variety of cryogenic temperature sensors. In case of the KATRIN experiment, however, several factors severely limit the choice of sensor type. These factors are:

- The sensors must be able to operate in the nominal magnetic field of the WGTS of 3.6 T.
- Due to the Kr mode of KATRIN, the sensors need to have a relative accuracy better than 10^{-3} at 100 K to 120 K.
- The sensors need to be reliable with a lifetime exceeding the operation period of KATRIN (3 years of raw measurement time, not counting maintenance periods) as they cannot be exchanged.
- The sensors need to withstand a temperature range of 30 K during nominal operation up to 550 K for bake-out purposes.

A detailed study of sensor types possibly fulfilling these criteria has been done in [Ram08]. The investigated sensor types are listed in table 2.2. As a result of this study, platinum resistance thermometers (PRTs) have been determined to be the most suited for measuring the WGTS beam tube temperature. Furthermore, platin resistance thermometers of the type Pt500 (see figure 2.12) were chosen. This type offers a compromise between better sensitivity compared to Pt100, and a more homogeneous influence of the external magnetic field due to smaller dimensions compared to Pt1000. A disadvantage of Pt500 sensors is, that there is no standard reference curve as there is for Pt100. This is not important for the target beam tube temperature of 30 K, however, as the standard reference curve for Pt100 sensor is only defined to a minimum temperature of $-200\,°C$ (73.15 K).

While this choice allows for a better theoretical calculation of shifts induced by the external magnetic field, it has been found that sensors showed individual behavior inside

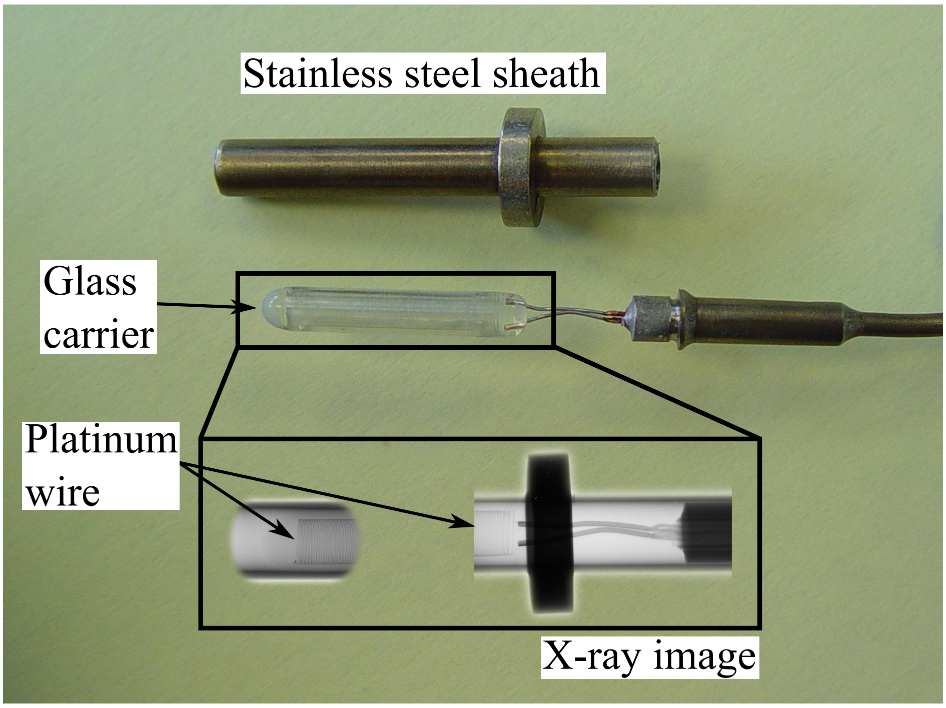

Figure 2.12.: Pt500 sensor used for WGTS beam tube with x-ray view. The custom-built Pt500 wire-wound glass sensors for the WGTS beam tube are protected by a stainless steel sheath and contacted in a four-wire configuration. Image adapted with permission from S. Grohmann.

the field. Due to this effect and a significant sample variation between the sensors, the Pt500 sensors cannot reliably measure the beam tube temperature with the accuracy of better than 10 mK required to verify the homogeneity of the beam tube temperature [Gro11, Ram08]. The uncertainties due to external magnetic field, sample variation, and other effects have been listed in [Gro11] and are shown in table 2.3. As one can see, the combined uncertainty for temperature measurement with the Pt500 inside an external magnetic field exceeds the uncertainty needed to measure the homogeneity with the required accuracy of 10 mK.

This necessitates calibrating the Pt500 sensors. For a sufficiently stable temperature on the order of several mK, most of the uncertainties shown in table 2.3 can be assumed to cause a constant offset. By calibrating the Pt500 sensors, this offset can be compensated, reducing the uncertainty to that of the calibration combined with the instrumentation and installation uncertainties. To account for potential aging effects of the sensors as well as to allow for the free choice of the external magnetic field, a system capable of in-situ calibration has been used. Each Pt500 sensor is mounted together with a vapor pressure sensor on the beam tube as seen in figure 2.13.

This type of sensor measures the pressure of a two-phase system, and is thus not influenced by external magnetic fields. Using this type of sensor for constant monitoring of the beam tube temperature is not practicable in the KATRIN WGTS cryostat design from a technical point of view. A way of monitoring the filling level to ensure that a liquid phase is present, as it is present in the two-phase system, would take up space, complicate the design, and raise the cost. For similar reasons, only a burst disk per vapor pressure sensor is used to prevent damage to the cryostat in case of uncontrolled evaporation of the contained liquid. It is very likely that an event where the burst disk

Table 2.3.: Uncertainties on uncalibrated Pt500 temperature measurement. Shown are experimental uncertainties on the temperature measurement with Pt500 sensors in normal KATRIN operation mode as well as in krypton mode. Table after [Gro11].

Parameter	Normal mode	krypton mode
Operating temperature	30 K	120 K
Required accuracy	<0.030 K	<0.120 K
Sample variation	0.087 K	0.404 K
Instrumentation uncertainty	0.022 K	0.060 K
Thermal cycling stability	0.006 K	0.003 K
B-field uncertainty	0.087 K	0.064 K
Installation uncertainty	0.001 K	0.001 K
Combined Uncertainty	0.125 K	0.413 K

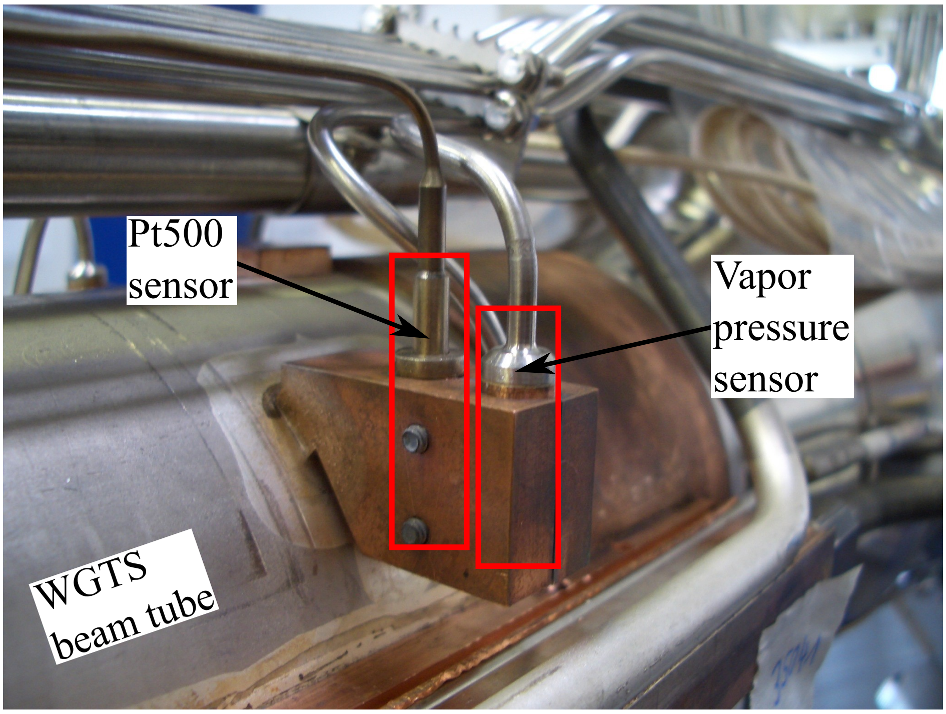

Figure 2.13.: Sensor block on beam tube. A copper block containing a Pt500 and a vapor pressure sensor is brazed to the WGTS beam tube. Image adapted with permission from S. Grohmann.

bursts will necessitate warming the entire cryostat up. Therefore, constant operation of the vapor pressure sensors is a constant risk. In addition, Pt500 sensors can be read-out via a multiplexer, while constant vapor pressure measurement would necessitate an equal number of high accuracy pressure transducers as there are sensors, which would be expensive.

By employing these vapor pressure sensors only as a means to calibrate the Pt500 sensors, these points can be avoided. The calibration of a Pt500 sensor is done in principle by simultaneous measurement of the Pt500 resistance and the pressure inside the vapor pressure sensor. The measured pressure can then be translated into a temperature via the saturation pressure curve of the used substance figure 2.10. The Pt500 resistance can then be identified with this temperature, correcting any deviations due to sample variation or influence of the magnetic field. The detailed procedure of the calibration is explained in section 3.2 and the resulting calculation uncertainties calculated in section 3.3.

The placement of 24 sensors according to the configuration shown in figure 2.14 allows for a temperature profile of the WGTS beam tube to be calculated. This profile can then be used to improve the accuracy of calculations of the density profile of tritium inside the beam tube. It is also is needed to calculate the other temperature related effects detailed in subsection 2.3.2. As such, the temperature data gained by this system is immensely important for accurate measurement of the neutrino mass, which makes detailed knowledge of all related uncertainties an absolute necessity.

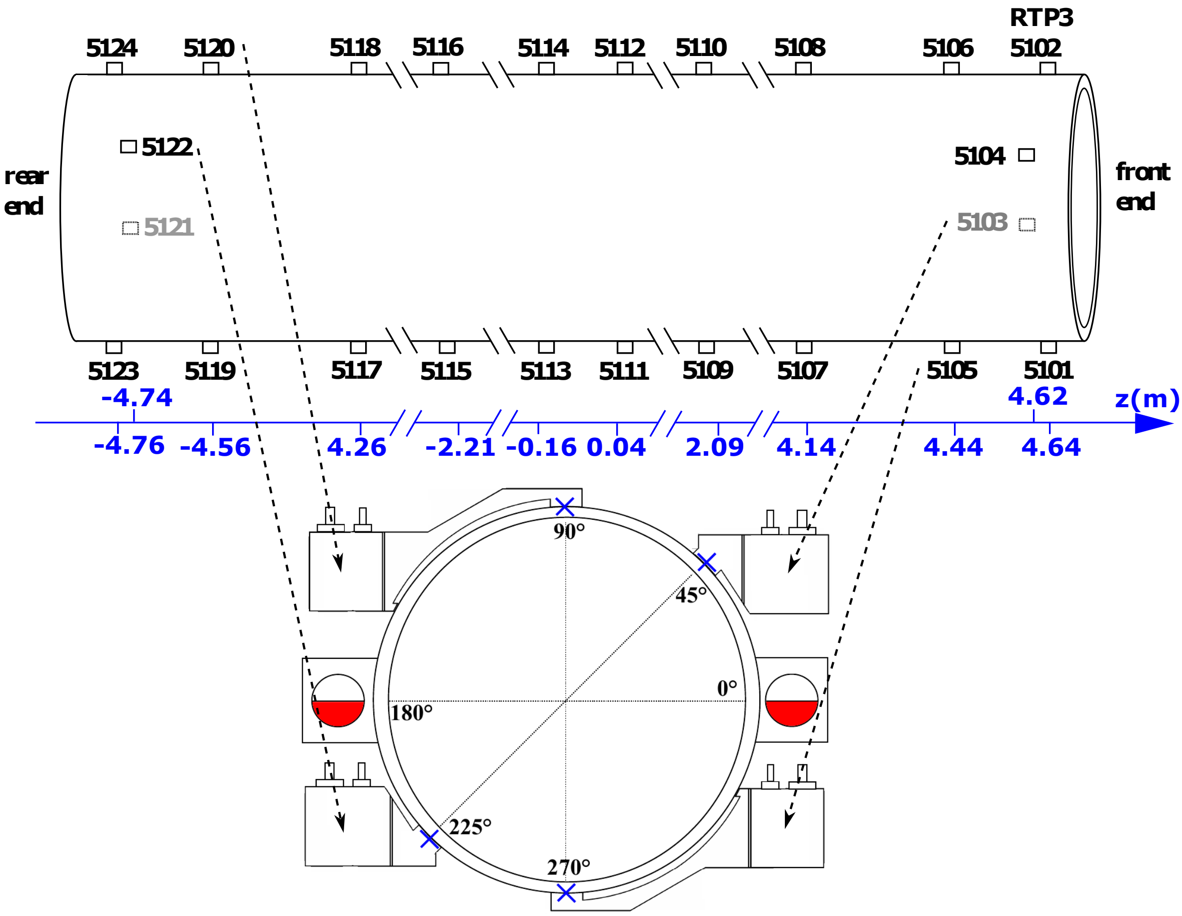

Figure 2.14.: Temperature sensor distribution along the beam tube. Along the length of the WGTS beam tube, 24 sensor blocks containing pairs of a Pt500 and a vapor pressure sensor have been brazed to it. The gas supply and readout for the vapor pressure sensors as well as the readout of the Pt500 sensors is situated outside of the WGTS cryostat. The vapor pressure sensors are connected to the pressure transducers and gas supply via small capillaries of 1 mm inner diameter. These capillaries are connected to the outer shield (see subsection 2.4.1) to minimize the heat load on the beam tube. The sensors are named after the KATRIN internal naming scheme, **RTP** indicating a platinum temperature sensor. Image drawn after [Höt12].

2.5. Objectives of this thesis

The performance of the WGTS beam tube cooling system has already been shown to be viable through measurements with the Demonstrator (see subsection 2.4.2), in which a temperature stability fulfilling, as well as a temperature inhomogeneity violating the KATRIN requirements have been observed. The calibration principle of the Pt500 temperature measurement system has also been tested with liquid nitrogen.

Based on this prior research, the focus of this work is (i) the detailed investigation of the Pt500 calibration procedure as it is implemented in and used for the operation of KATRIN with all related uncertainties, (ii) the measurement of the temperature stability of and homogeneity along the WGTS beam tube in its final configuration. In detail these objectives comprise the following:

Pt500 calibration

A detailed calibration procedure for the Pt500 measurement system in the final instrumentation for nominal KATRIN operation has to be developed. All uncertainties on this temperature measurement have to be identified and quantified as they are crucial for the sensitivity of KATRIN. It needs to be investigated whether the uncertainties allow for the measurement of the temperature stability and homogeneity with the necessary relative accuracy of better than 0.1 %. The impact of drift over time and the influence of external magnetic fields on the calibration factors obtained has to be investigated. This is necessary to ensure the validity of the temperature measurement over the duration of a KATRIN measurement run of 60 d. In case this is not given, it is necessary to derive a time frame after which the system has to be recalibrated.

Measurement of the temperature stability and homogeneity

With the calibrated temperature measurement system, the stability and homogeneity of the WGTS beam tube have to be investigated.

The achievement of the temperature stabilization to be better than ±30 mK/h has to be shown.

The homogeneity of the WGTS beam tube temperature has to be measured and the achievement of the specification of less than ±30 mK temperature difference along the beam tube has to be verified. In case of an inhomogeneity, as observed in the Demonstrator, it has to be quantified and its impact on the KATRIN sensitivity considered.

3. Calibration of the Pt500 sensors with an accuracy better than 10^{-3}

To measure the temperature stability and homogeneity of the WGTS beam tube, the Pt500 sensors mounted along it need to be calibrated due to the reasons detailed in subsection 2.4.3. The calibration procedure is detailed in this chapter and its validity for KATRIN operation is investigated.

One important part of the beam tube temperature measurement is the data acquisition system responsible for reading out the Pt500 sensors. It is called *Temperaturerfassungssystem* (TES) and its components and data flow are described in section 3.1. The following section 3.2 describes the calibration procedure developed over the course of this thesis. The uncertainties on the temperature measurement with the calibrated Pt500 via this procedure are presented in section 3.3. Measurements of the calibration factors to determine their stability over time and stability in response to outside magnetic fields are presented in section 3.4. Finally, the implications of the the achieved results for KATRIN are discussed in section 3.5.

3.1. Description of the Pt500 calibration and data acquisition system

The *Temperaturerfassungssystem* (TES) is the software responsible for controlling the components used for calibrating and reading out all Pt500 sensors which measure the beam tube temperature. It controls and monitors the following hardware components:

- the 24 Pt500 sensors mounted on the beam tube and 4 Pt500 sensors mounted on the pump ports,
- 1 digital multimeters with 2 multiplexer cards,
- 1 power supply,
- 2 precision resistors at $10\,\Omega$ and $150\,\Omega$,
- the vapor pressure sensor cavities, called *bulbs*, next to the Pt500 sensors,
- 5 valve blocks which connect the bulbs to the
- 15 pressure transducers (3 transducers per valve block), as well as to

- the gaseous neon supply.

Datasheets for the digital multimeter, the power supply, and the pressure transducers can be found in Appendix B.

Actually, the TES incorporates more components than the ones just listed above. Those components are mainly used for operative temperature monitoring of the different cooling circuits of the WGTS. These sensors are therefore not relevant for the KATRIN neutrino mass analysis. At the time this thesis is being written, these components are being removed from the TES to decouple cryostat operation from measurements related to the neutrino mass. The reason for this is that a malfunction of the TES does not affect the operational safety of the cryostat.

Details of the components important for the beam tube temperature measurement are described in the following. The uncertainties related to the components are discussed in subsection 3.3.1:

Pt500 sensors The used Pt500 sensors are custom-built and consist of a platinum wire wound around a glass carrier (see figure 2.12). The glass carrier is sheathed by a casing of stainless steel to make the sensors more robust. The platinum wire is contacted in a four-wire configuration for precise resistance read-out.

Digital multimeter The used digital multimeter (DMM) is of the type `Model 2701 Ethernet-Based DMM / Data Acquisition System` made by `Keithley` [Kei03]. Two of the four wires contacting the Pt500 sensors are connected to one input channel on one multiplexer card of the digital multimeter, which measures the resistive voltage drop. As the mulitplexer cards only have 20 channels each, two cards are needed to cover all of the 24 Pt500 sensors along the beam tube and the 4 Pt500 sensors connected to the pump ports.

Power supply The used power supply is of the type `Model 6220 DC Current Source` made by `Keithley` [Kei05]. It is set to constant current mode and connected to the remaining two contacts of all Pt500 sensors in series. This ensures that all resistors are supplied with the same current of $500\,\mu A$. Pt500 sensors assigned to the same digital multimeter are also assigned to the same power supply.

Precision resistors The precision resistors with $10\,\Omega$ and $150\,\Omega$ are connected in series to the Pt500 sensors. The purpose of these precision resistors is that the stability of the power supply can be monitored by measuring the resistive voltage drop of the precision resistors. This is required to reduce the instrumentation uncertainty (for details see subsection 3.3.1).

Bulbs The bulbs are the key element of the vapor pressure sensors used to calibrate the Pt500 sensors. They are cylindrical in form with a height of $22\,mm$ and a radius of $3\,mm$, leading to a volume of $622\,mm^3$. During calibration the bulbs are filled with a gas-liquid two phase mixture of neon, as described in subsection 2.4.3. The temperature of this mixture dictates the pressure inside the capillaries connecting the bulbs to the valve blocks where the pressure is measured by the pressure transducers.

Valve blocks The purpose of the 5 valve blocks is to dynamically connect the 28 bulbs to 12 of the pressure transducers (1 valve block including 3 pressure transducers was intended for additional vapor pressure sensors, which were not included in the final WGTS cryostat design). This is achieved by an array of magnetic valves, which can connect any bulb to any pressure transducer. Furthermore, the valve blocks also contain one mass flowmeter each which is used to measure the amount of gas fed into the bulbs.

Pressure transducers The used pressure transducers are of the type `Cerabar S PMC71` made by `Endress+Hauser` [End17]. The three pressure transducers per valve block are connected to the neon supply, a vacuum line and the waste air system. This leads to a limitation in the calibration procedure, as only one bulb per valve block can be filled at a time with a precise amount of neon as it is needed for calibration.

Neon supply The neon in the vapor pressure sensors is supplied by a gas bottle of N6.0[1] neon connected to the valve blocks. This is the same supply used to fill the two-phase neon cooling system for the beam tube.

TES computer and software The TES computer and the TES software are responsible for aggregating all measured data and controlling the valve blocks for calibration. The digital multimete and power supply are connected to the computer via `Ethernet`. The valve blocks and pressure transducers are connected to the TES computer via `PROFIBUS`. The data of all sensors connected to the TES computer is preprocessed before being transmitted to the `SIMATIC PCS7`[2] process control system of KATRIN via `PROFIBUS`, and finally logged in the central KATRIN ADEI (Advanced Data Extraction Infrastructure [Chi10]). The details of this process are described below.

The TES software uses measurement cycles of 30 s length. This length is required both to process the data and to prolong the lifetime of the multiplexer cards of the digital multimeter, as they are only rated for a finite number of cycles. To illustrate how the TES works, one measurement cycle is described in detail in the following. The associated flowchart can be seen in figure 3.1.

The power supply provide a constant current running through the Pt500 and precision resistors. At the beginning of a measurement cycle, the multiplexer inside the digital multimeter switches through all of its channels, measuring the resistive voltage drop of the Pt500 and precision resistors. This voltage drop U is then used to calculate the resistance of the sensors via $R = U/I$, where I is the current set point of the power supply. In the next step, individual characteristic curves for the sensors are used to calculate temperatures from the resistances. As the characteristic curves are given by supporting points in intervals of 0.1 K, this is done via linear interpolation between two supporting points to get the temperature for any given resistance. The temperatures gained this way are then transmitted from the TES computer to the PCS7 process control system. From there, the temperatures are logged into the ADEI database at intervals of 5 s. This means that during one measurement cycle of the TES system, several data points with the same temperature value are written into the ADEI database, which needs to be considered when analyzing the data.

Only temperatures are transmitted to the ADEI system, while the measured resistances and pressures are not relayed from the TES system to PCS7 and ADEI. Internally, the

[1] N6.0 denotes the purity of the used gas as 99.9999 % pure, meaning it contains only 1 ppm impurities.

[2] For manuals see: `http://w3.siemens.com/mcms/industrial-automation-systems-simatic/en/manual-overview/tech-doc-pcs7/pages/default.aspx`

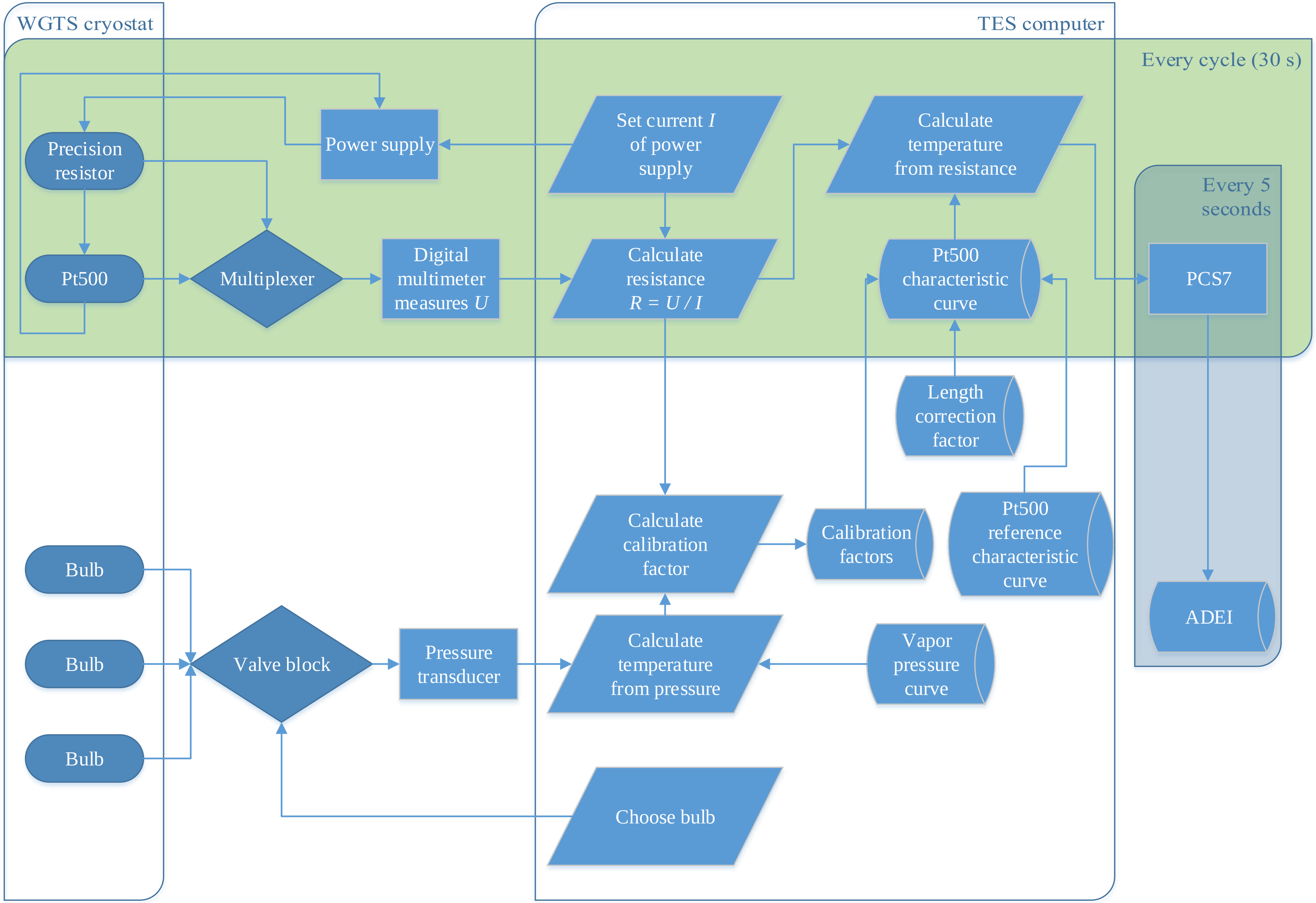

Figure 3.1.: TES Flowchart. Data flow through the TES, from sensor to ADEI database. Pill-shaped boxes represent sensors, rectangular boxes represent physical components, parallelogram-shaped boxes represent actions, and cylindrical boxes represent data. For details see text.

TES system saves all of its sensor data, as well as all calculated temperatures based on that data, once during a measurement cycle into a separate log file. This allows for later reevaluation of the measured data.

The characteristic curves used to calculate the temperatures are based on a reference characteristic curve (for details see subsection 3.3.4). The individual characteristic curve for each sensor is calculated from the reference curve during calibration and includes two corrections. The first is the length correction which accounts for sample variations with regards to the length of the platinum wire inside the Pt500 sensors. Here, the characteristic curve is divided by a factor l. This factor l is given by the quotient of the resistance measured during the triple point measurements of the Pt500 sensors before installing them into the WGTS cryostat, and a reference value of $500\,\Omega$. The purpose of this calculation is to correct the slope of each sensor's characteristic curve to be that of a reference Pt500 with exactly $500\,\Omega$ at $0\,°\mathrm{C}$. The second correction accounts for the offset induced by sample variations as well as due to external magnetic fields and aging of the sensors. Here, the calibration constant obtained by calibration with the vapor pressure sensors is added onto the characteristic curve as an offset.

The detailed procedure of how these calibration factors were obtained is given in the following section 3.2.

3.2. Calibration procedure

The calibration procedure for the Pt500 sensors belonging to the TES system in detail consists of 6 conceptual steps. A complete instruction, including all explicit steps to calibrate all 28 sensors, is given in Appendix A. The conceptual steps for calibrating a single sensor are shown and described in the following. These steps are:

- Preparation of the vapor pressure system,
- Filling of the bulb,
- Thermalization,
- Calibration,
- Emptying the bulb,
- Refilling the bulb with gaseous neon,
- Returning the vapor pressure system to its initial state.

A graph showing the calibration process as a function of time is shown in figure 3.2.

Preparation of the vapor pressure system The valves connecting the neon supply to the valve blocks are opened. The approximate temperature of the beam tube is used to look up the saturation vapor pressure of neon at that temperature (see figure 2.10). The pressure of the incoming neon supply is regulated to an overpressure of about 1 bar in relation to this calculated value.

Filling the bulb The neon supply is connected to one bulb via the mass flowmeter of the bulb's valve block. This also connects the bulb to the supply line pressure transducer. The mass flowmeter is then set to a mass flow of 10 mg/s to 20 mg/s until the vapor pressure temperature displayed by the TES software is about 0.5 K

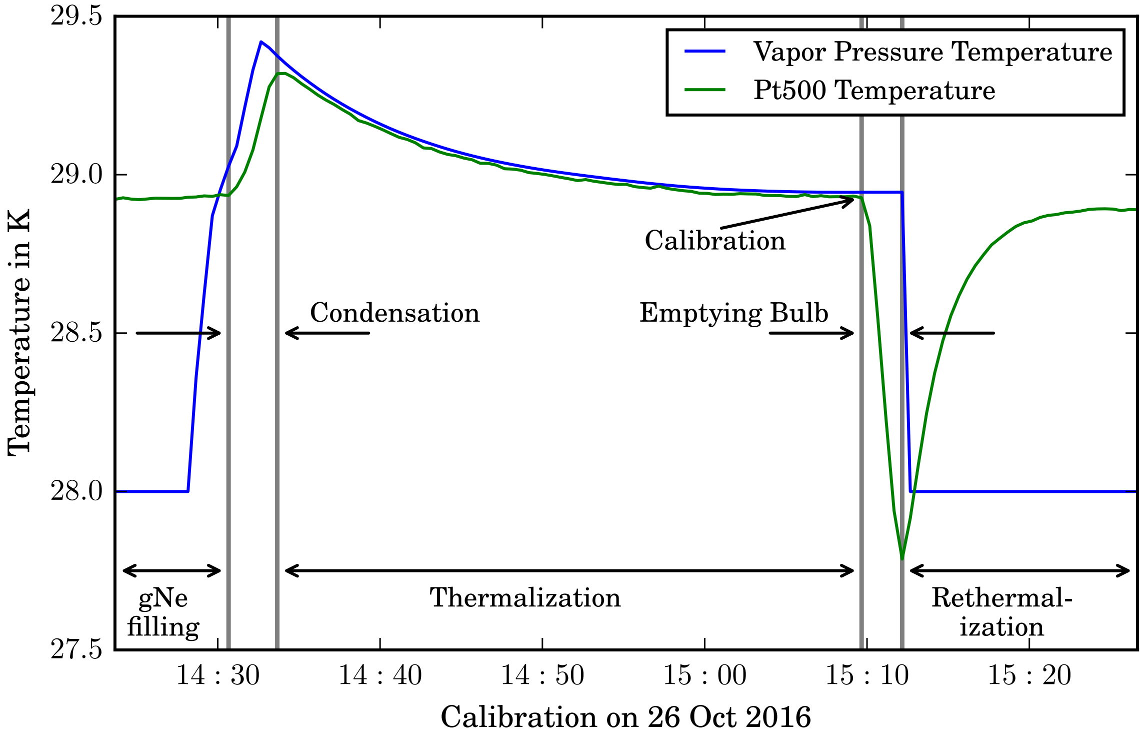

Figure 3.2.: Calibration Procedure of a Pt500 sensor. Shown is the temperature data of a Pt500 and a vapor pressure sensor taken during the calibration of one Pt500 sensor. The Pt500 temperature for the entire graph is calculated with the calibrated characteristic curve (see section 3.1). The labeled steps of the calibration procedure are discussed in the main text.

below the displayed Pt500 temperature. Then, the mass flow is decreased to about 1 mg/s to 5 mg/s. At first, this mass flow increases the pressure of the gaseous neon inside the bulb and capillaries, as seen in the leftmost region of figure 3.2. This continues until the pressure inside the bulb reaches the saturation vapor pressure of the temperature of the bulb. At this point, any additional gaseous neon flowing inside the bulb starts to condensate. After condensation sets in, an additional amount of ∼350 mg neon is filled into the bulb via the flowmeter. This amount equates to a liquid level of approximately half the bulb height. After this amount has been filled into the bulb, the flowmeter is set to 0 mg/s which cuts off the neon supply from the bulb.

The latent heat of condensation heats up the sensor block containing the bulb and Pt500 sensor. This causes the saturation vapor pressure to rise and thus the pressure inside the bulb continues to increase. Therefore the moment in which condensation sets in can not be inferred from the pressure signal. Instead, the point at which the effect of the heat of condensation is visible in the Pt500 signal is chosen as the point where condensation sets in. The uncertainty on the filling of the bulb due to inaccurate knowledge of the starting point of condensation has no serious impact on the calibration. As long as the bulbs are not either completely filled or empty, the impact of the filling level on the temperature measurement is insignificant.

Thermalization As the filling process has heated up the sensor block by several hundered mK, which is significantly more than the target accuracy of $\pm 30\,\mathrm{mK}$, the bulb is left to cool down to the temperature of the beam tube. This thermalization process takes on the order of 30 min, depending on the filling level.

Calibration When the temperature indicated by Pt500 sensor has approximately reached the temperature before the neon condensation, the actual calibration of the Pt500 sensor is done. Upon triggering the calibration in the TES software, the current value of vapor pressure temperature is used to calculate a resistance value via the reference Pt500 characteristic curve. The difference between this calculated resistance and the measured resistance of the Pt500, called *calibration constant* in the following, is then added to the characteristic curve of the Pt500 sensor.

As the system always uses the current value of the pressure for its calculations, the TES calibration function needs to be triggered immediately after the digital multimeter has completed its measurement.

Emptying the bulb After the Pt500 sensor has been calibrated, it is necessary to empty the bulb of liquid neon to eliminate any potential dangers to the cryostat due to rapid evaporation and resulting overpressure. As can be seen from the Pt500 signal in figure 3.2, the emptying of the bulb and the resulting pressure reduction lead to a cooling of the whole sensor block due to the latent heat of vaporization. After the bulb has been emptied, the temperature of the sensor block returns to its prior value before the start of the calibration procedure.

Refilling the bulb with gaseous neon Emptying the bulb has resulted in an underpressure, which could lead to laboratory air entering into the system through leaks. As the air would freeze inside the cryostat and could form blockades, this constitutes a safety hazard. Therefore, after the bulbs have been emptied of liquid neon, they are filled again with gaseous neon to achieve an overpressure in comparison to the atmospheric pressure. For beam tube temperatures below around 28 K, care has to be taken not to reach the saturation vapor pressure and start condensating neon again.

Returning the vapor pressure system to its initial state After refilling the bulbs, all valves inside the valve block and all valves connecting the valve block and neon supply are closed.

The above steps, except the first and the last, which can be done once at the beginning and end of a calibration run, have to be done for each of the 28 Pt500 sensors. With this procedure, one sensor per valve block can be calibrated at a time, resulting in a parallel calibration of a maximum of 4 Pt500 sensors at once. As the sensors are not evenly split between valve blocks, achieving the maximum of 4 sensors at once is not possible for an entire calibration run of all 28 sensors. In this procedure, only the pressure transducers connected to the neon supply line are used to measure the vapor pressure.

The time needed to calibrate a single sensor is mainly dictated by the time it takes to fill and empty a sensor. During the thermalization of the neon inside the bulb, sensors on a different valve block can be filled and emptied. With the procedure described the filling 4 sensors, one on each valve block, with neon so that the neon inside the bulb filled first has just thermalized by the time the 4th sensor has been filled, has been achieved.

The shortest calibration runs that have been achieved in the course of this thesis had a duration of around one workday for 25 sensors (three were out of work). Therefore two workdays should be considered as a realistic time needed for a calibration run for planning purposes.

3.3. Determination of calibration uncertainties

By following the procedure in the previous section, calibration constants for the temperature measurement with the Pt500 sensors are gained. To be able to measure whether the stability and homogeneity of the beam tube temperature are within the requirement of 0.1 %, the uncertainty of the temperature measurement has to be much better than 0.1 %. For the nominal beam tube operation temperature of 30 K, the uncertainty on the temperature measurement needs to be below ±10 mK [Ram08]. The uncertainties on the temperature measurement are detailed in this section.

In subsection 3.3.1, the instrumentation uncertainties of the Pt500 power supply and digital multimeter as well as the uncertainty of the pressure transducer are discussed. More details on the systematic effects of the vapor pressure sensors are given in subsection 3.3.2. The uncertainty on the temperature due to the linear interpolation of characteristic curves used by the TES software is calculated in subsection 3.3.3. This is followed by a discussion of the uncertainty of the used Pt500 reference characteristic curve in subsection 3.3.4. Finally in subsection 3.3.5, all of the uncertainties are combined, and uncertainties for the relative and absolute temperature measurement in chapter 4 are given.

All uncertainty considerations in this section are based on the *Guide to the Expression of Uncertainty in Measurements* (GUM) [BIP08]. In particular, this means that for type B uncertainties, encompassing all uncertainties not derived via statistics, a rectangular distribution is assumed if not stated otherwise. This leads to a contribution of a factor $\sqrt{\frac{1}{3}}$ when converting upper and lower limit uncertainty specifications into standard uncertainties.

3.3.1. Uncertainties due to instrumentation

In this subsection the instrumentation uncertainties on the temperature measurement after calibration are calculated.

Pt500 Sensors

The uncertainties on the temperature measurement originating from the Pt500 readout electronics are given by the uncertainty of the digital multimeter and that of the power supply. Below, the uncertainties according to the data sheets are listed and resulting uncertainties for the KATRIN boundary conditions are calculated. Following boundary conditions were used for the calculations:

- a current set point of 500 µA,
- a temperature of 35 °C inside the TES cabinet,

- a resistance of the Pt500 sensors of $10\,\Omega$, which equates to a temperature of around 30 K.

The temperature value for the inside of the TES cabinet is based on a pyrometer measurement. The resistance value of the Pt500 sensor is an approximation based on the characteristic curve produced in [Gro11]. After testing at currents 100 µA, 250 µA, and 500 µA, the current set point of 500 µA has been chosen as a compromise between a desirably high voltage drop –an therefore low noise– and minimization of self-heating. For a resistance of $10\,\Omega$ and a current of 500 µA, $2.5 \cdot 10^{-6}$ W of electric energy are turned into heat. Due to the good thermal coupling between sensor and sensor mount on the beam tube, however, this heat is quickly dissipated and the effect on the measured temperature is negligibly small [Gro11].

Digital multimeter

The used digital multimeter is a `Model 2701 Ethernet-Based DMM/Data Acquisition System` made by `Keithley`. For the given values of current and resistance, the measured voltage is 5.0 mV. Therefore the intresting measurement range is that up to 100 mV. The data sheet values for this range are [Kei03]:

- in the measurement range up to 100 mV:
  - an accuracy per 24 h of $15\,\text{ppm} \cdot rdg + 3.0 \cdot 10^{-3}\,\text{mV}$,
  - a temperature coefficient of $1\,\text{ppm} \cdot rdg + 0.5 \cdot 10^{-3}\,\text{mV}$ per K outside the temperature range $(23 \pm 1)\,°\text{C}$,

With the voltage of 5.0 mV and an operation temperature of 35 °C this leads to an uncertainty of:

$$\sigma_{\text{dmm}} = \Bigg(\frac{1}{3} \cdot (15\,\text{ppm} \cdot 5.0\,\text{mV} + 3.0 \cdot 10^{-3}\,\text{mV})^2 + \frac{1}{3} \cdot (35 - 24)^2 \cdot (1\,\text{ppm} \cdot 5.0\,\text{mV} + 0.5 \cdot 10^{-3}\,\text{mV})^2\Bigg)^{\frac{1}{2}} \;, \tag{3.1}$$

$$\sigma_{\text{dmm}} = 3.7 \cdot 10^{-3}\,\text{mV} \;, \tag{3.2}$$

$$\frac{\Delta \text{V}}{\text{V}} = \frac{3.7 \cdot 10^{-3}\,\text{mV}}{5.0\,\text{mV}} = 0.07\,\% \;. \tag{3.3}$$

Power supply

The used power supply is a `Model 6220 DC Current Source` made by `Keithley`. The appropriate current range for the measuring current of 500 µA is that up to 2 mA. The data sheet values for this range are [Kei05]:

- accuracy per year: $(0.05\,\% \cdot rdg + 1\,\mu\text{A})$,
- temperature coefficient: $(0.005\,\% \cdot rdg + 2 \cdot 10^{-2}\,\mu\text{A})$ per K outside the temperature range $(23 \pm 5)\,°\text{C}$.

For the current of 500 µA and the operation temperature of 35 °C this leads to the following uncertainty:

$$\begin{aligned}\sigma_{\text{sup}} =& \Big(\frac{1}{3}\cdot(0.05\,\%\cdot 500\,\mu\text{A} + 1\,\mu\text{A})^2 \\ & +\frac{1}{3}\cdot(35-28)^2\cdot(0.005\,\%\cdot 500\,\mu\text{A} + 2\cdot 10^{-2}\,\mu\text{A})^2\Big)^{\frac{1}{2}}\ ,\end{aligned} \tag{3.4}$$

$$\sigma_{\text{sup}} = 0.74\,\mu\text{A}\ , \tag{3.5}$$

$$\frac{\Delta I}{I} = \frac{0.74\,\mu\text{A}}{500\,\mu\text{A}} = 0.15\,\%\ . \tag{3.6}$$

This uncertainty on the absolute value of the supplied measuring current as well as the uncertainty on the voltage measurement are above the required accuracy of 0.033 % ($\widehat{=}$10 mK). Measurements of a precision resistor, however, have shown that the precision of the resistance readout combining digital multimeter and power supply is at least one order of magnitude better than 0.033 %. The trueness requirement of the temperature measurement can be fulfilled by the vapor pressure calibration alone as long as the resistance readout is precise enough that the combined uncertainty of vapor pressure measurement and resistance readout is below the requirement of 0.033 %. Therefore the following method of uncertainty estimation of the relative resistance measurement was developed.

Uncertainty minimization with precision resistors

To confirm the stability and quantify the precision of the resistance measurement, two precision resistors – one for tritium and one for krypton mode – are connected in series to the Pt500 sensors. The resistance measurement of these resistors shares the same systematic effects as the Pt500 resistance measurement. With 10 Ω resistance, the precision resistors are comparable to the Pt500 sensors at 30 K, but with a stability of better than 0.01 %/yr, so they can be considered as constant for the relevant measurement durations of 1 h up to 60 d. The accurate absolute value of their resistance is irrelevant for comparison with the Pt500, as only the precision and stability of the readout needs to be considered. The resistance of the precision resistors is processed just like the measured resistance of the Pt500 (see section 3.1) and results in a temperature signal. The standard deviation of this signal over the same duration as the measurement is then taken as the uncertainty of the electronic readout of the Pt500 sensors.

With measurements based on this approach, the uncertainty on the relative Pt500 read out could be estimated to be below

$$\sigma_{\text{Pt500}} = 0.5\,\text{mK}\ . \tag{3.7}$$

Compared with the uncertainty on the absolute temperature measurement derived from the data sheet values of $\sigma_{\text{datasheet}} \sim 50\,\text{mK}$, the precision resistor measurement has shown that the combination of the used digital multimeter and power supply outperform this uncertainty by two orders of magnitude in terms of precision. Since the precision resistors are measured together with the Pt500 sensors during normal operation, the uncertainty on the Pt500 resistance measurement can be calculated for any desired time interval.

Vapor pressure sensors

Another source of uncertainty are the used pressure transducers of type `Cerabar S PMC71` made by `Endress+Hauser`. According to the data sheet [End17], the pressure transducer has an accuracy of 0.05 % Full Scale of the range 0 bar to 4 bar [Gro11], leading to a half-width of 2 mbar under assumption of a rectangular distribution. The saturation pressure curve for neon [Lin05] is used to calculate the pressure at 30 K. Then the temperatures for pressures ±2 mbar around that value are calculated, resulting in the following temperature differences of

$$\Delta T_{+} = +2.14\,\mathrm{mK}\ , \tag{3.8}$$

$$\Delta T_{-} = -2.05\,\mathrm{mK}\ . \tag{3.9}$$

Assuming a rectangular distribution, this leads to a standard uncertainty on the temperature measurement due to the uncertainty of the pressure transducer of:

$$\sigma_{\mathrm{transducer}} = \sqrt{\frac{1}{3} \cdot \left(\frac{(2.14\,\mathrm{mK} - (-2.05\,\mathrm{mK}))}{2}\right)^2}\ , \tag{3.10}$$

$$\sigma_{\mathrm{transducer}} = 1.21\,\mathrm{mK}\ . \tag{3.11}$$

3.3.2. Uncertainties due to vapor pressure related systematic effects

Beside the uncertainty on the vapor pressure measurement due to the uncertainty of the pressure transducer, several other systematic effects also contribute to the uncertainty of the temperature measurement via the vapor pressure sensors.

Thermomolecular effect

The temperature difference between room temperature at the pressure transducers' position in the cabinet and around 30 K inside the bulb causes a static pressure difference due to the thermomolecular effect [Wat67]. For the geometry of the WGTS cryostat vapor pressure system, the systematic effect on the measured vapor pressure temperature due to the thermomolecular effect has been calculated in [Gro11]:

$$\Delta T_{\mathrm{mol}} = 0.7\,\mathrm{mK}\ . \tag{3.12}$$

Under the assumption of a rectangular distribution, this results in a standard uncertainty of:

$$\sigma_{\mathrm{mol}} = \sqrt{\frac{1}{3} \cdot \left(\frac{0.7\,\mathrm{mK}}{2}\right)^2}\ , \tag{3.13}$$

$$\sigma_{\mathrm{mol}} = 0.2\,\mathrm{mK}\ . \tag{3.14}$$

Aerostatic pressure differences

The effects of aerostatic pressure differences have been calculated in [Gro11]. These effects are due to unknown density profiles inside the capillaries in a vertical section of 0.3 m length, which result in a maximum temperature difference of

$$\Delta T_{\mathrm{aero,max,1}} = 0.6\,\mathrm{mK}\ . \tag{3.15}$$

Two further contributions originate from differing heights of the individual bulbs of up to 0.06 m and a height difference between the beam tube and the position of the pressure transducers of about 1 m:

$$\Delta T_{\text{aero,max,2}} = 0.2\,\text{mK} \ , \tag{3.16}$$

$$\Delta T_{\text{aero,max,3}} = 0.3\,\text{mK} \ . \tag{3.17}$$

It is assumed that the influence of the beam tube temperature on these effects is insignificant. These systematic effects introduce an additional standard uncertainty of

$$\sigma_{\text{aero}} = \sqrt{\frac{1}{3} \cdot \left(\left(\frac{0.6\,\text{mK}}{2}\right)^2 + \left(\frac{0.2\,\text{mK}}{2}\right)^2 + \left(\frac{0.3\,\text{mK}}{2}\right)^2 \right)} \ , \tag{3.18}$$

$$\sigma_{\text{aero}} = 0.2\,\text{mK} \ , \tag{3.19}$$

which contributes to the vapor pressure temperature measurement.

Temperature gradient in the sensor bulbs

The effect of temperature gradients inside the sensor bulbs has been calculated in [Gro11] to be below 1 mK for the bulb with the largest heat load at 30 K. In accordance with this value, one gains a standard uncertainty of:

$$\sigma_{\text{gradient}} = \sqrt{\frac{1}{3} \cdot \left(\frac{1.0\,\text{mK}}{2}\right)^2} \ , \tag{3.20}$$

$$\sigma_{\text{gradient}} = 0.29\,\text{mK} \ . \tag{3.21}$$

Uncertainty on vapor pressure curve

The used saturation pressure curve $f(T)$ is based on data from [Lin05]. According to NIST, the curve is known with a relative accuracy of $\frac{\Delta p}{p} = 0.2\,\%$. This uncertainty can be translated into an uncertainty on the temperature as follows:

$$p = f(T) \ , \tag{3.22}$$

$$\Delta p = \left|\frac{\partial f(T)}{\partial T}\right| \cdot \Delta T \ , \tag{3.23}$$

$$\Delta T = \Delta p \cdot \left|\frac{\partial f(T)}{\partial T}\right|^{-1} \ , \tag{3.24}$$

$$\Delta T = 0.2\,\% \cdot p \cdot \left|\frac{\partial f(T)}{\partial T}\right|^{-1} \ . \tag{3.25}$$

The derivative of the saturation pressure curve $\frac{\partial f(T)}{\partial T}$ has been computed numerically by forming the difference quotient between two supporting points of the saturation pressure curve. For 30 K the derivative has a value of 0.545 mbar/mK. As can be seen in figure 3.3, the uncertainty on the absolute temperature depends on the pressure and thus on the temperature itself. For 30 K and the resulting saturation pressure of 2230 mbar, this leads to an uncertainty of the absolute temperature of

$$\sigma_{\text{curve}} = 8.14\,\text{mK} \ . \tag{3.26}$$

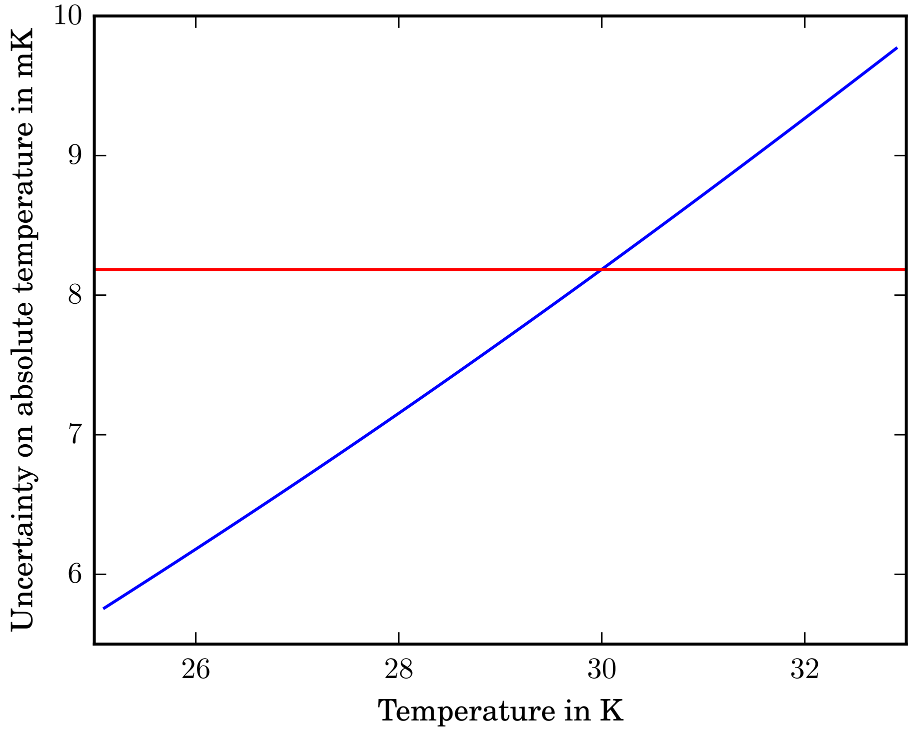

Figure 3.3.: Uncertainty on the saturation vapor pressure curve. The uncertainty on the saturation vapor pressure curve is explicitly dependent on the temperature. The red line shows the uncertainty at 30 K.

3.3.3. Uncertainties due to interpolation of Pt500 characteristic curves

The TES software uses linear interpolation to calculate temperatures for resistance values between the supporting points of the Pt500 characteristic curves. As the characteristic curves are not linear, this leads to an error. This error can be estimated as follows [Kle05]:

$$e(x) \leq \frac{\max(f''(x))}{2} \cdot |(x - x_n) \cdot (x - x_{n-1})| \ , \tag{3.27}$$

with

- the true underlying function f of the characteristic curve,
- the maximum of the second derivative of f in the range of x_{n-1} to x_n,
- and the supporting points x, x_{n-1} and x_n.

As the true function f of the characteristic curve is unknown, its second derivative is estimated by looking at the surrounding supporting points. One can see from figure 3.4 that the Pt500 characteristic curve is given by a strictly increasing function. For such a function the maximum of the second derivative is always at the upper limit of any interval. Therefore the maximum of f'' in $[x_{n-1}, x_n]$ is $f''(x_n)$:

$$\max(f''(x)) = f''(x_n) \ , \tag{3.28}$$

which can be used to approximate $e(x)$ as:

$$e(x) \leq f''(x_n) \cdot |(x - x_n) \cdot (x - x_{n+1})| \ . \tag{3.29}$$

The second derivative $f''(x_n)$ is calculated as a difference quotient:

$$h_1 = |x_{n-1} - x_n| \ , \tag{3.30}$$
$$h_2 = |x_{n+1} - x_n| \ , \tag{3.31}$$
$$\max(f''(x)) = f''(x_n) \tag{3.32}$$
$$= \frac{1}{2} \cdot \left((y_{n-1} - y_n) \cdot \left(\frac{1}{h_1^2} + \frac{1}{h_1 h_2} \right) + (y_{n+1} - y_n) \cdot \left(\frac{1}{h_2^2} + \frac{1}{h_1 h_2} \right) \right) \ . \tag{3.33}$$

In the present case, the x are the resistances and the y the temperatures of the characteristic curve. The supporting points of the Pt500 characteristic curves are spaced equally in steps of 0.1 K. For the used characteristic curves, this leads to an error of less than

$$\Delta T_{\mathrm{int}} = 0.63\,\mathrm{mK} \tag{3.34}$$

on the temperature measurement in the range of 28 K to 32 K. Under assumption of a rectangular distribution of the error, this leads to a standard uncertainty of

$$\sigma_{\mathrm{int}} = 0.18\,\mathrm{mK} \ . \tag{3.35}$$

3.3.4. Uncertainties due to uncertainty on Pt500 characteristic curves

The reference Pt500 characteristic curve used in the TES system has been produced by [Gro11]. It has been created by calibrating five sensors twice before installation into the WGTS cryostat. They have been calibrated over a temperature range of 20 K to 300 K. Cubic splines were fitted to the values obtained through this calibration, and finally the splines were averaged to obtain a reference Pt500 characteristic curve.

As neither an uncertainty on this curve nor the raw data of the calibration are available, the uncertainty on the Pt500 characteristic curve has to be estimated reliably.

3.3.5. Summary and discussion of uncertainties

The unkown uncertainties due to the Pt500 characteristic curves are an open problem that needs to be addressed. As a first step towards ammending this issue, the in-situ measurement of individual Pt500 characteristic curves has been tested.

In-Situ measurement of characteristic curves

The procedure for the in-situ measurement is an extension of the calibration procedure described in section 3.2. The same steps are taken until the bulbs have been filled with a two-phase gas-liquid mixture of neon. In this state, the temperature of the WGTS beam tube is lowered at a slow rate on the order of ∼0.5 K/h. During this process, the TES system is continuously measuring both resistance of a Pt500 sensor and the pressure of the corresponding vapor pressure sensor in 30 s intervals. This procedure is referred to as ***Slope Method*** in the following. The complementary ***Supporting Point Method*** is an approach where the temperature decrease is stopped at several temperatures to

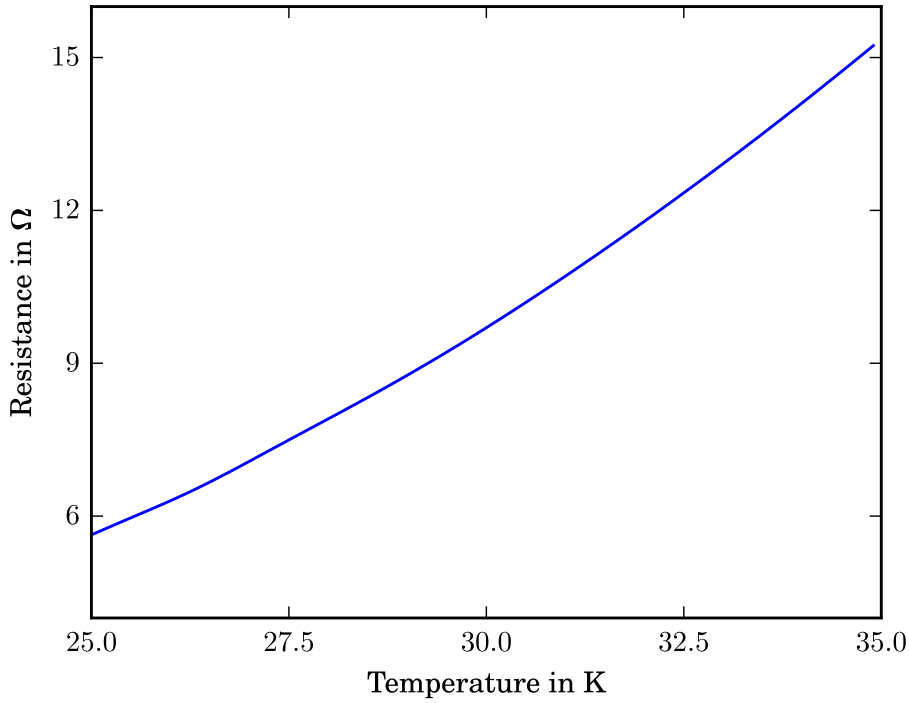

Figure 3.4.: Characteristic curve of a Pt500 in a region around the nominal beam tube temperature of 30 K. The the characteristic curve can is strictly increasing. Based on data mentioned in [Gro11].

wait for the system to thermalize, and measure at that discrete temperature. This allows for conditions inside the sensor block to be closer to those during normal operation.

Similar to the calibration procedure, a characteristic curve for a maximum of 4 sensors can be taken simultaneously. As these methods take more time than the simple calibration at a stationary temperature and require changing the beam tube temperature, they have only been tested with three sensors. These three sensors were **RTP-3-5102**, **RTP-3-5113**, and **RTP-3-5123** (for their positions on the beam tube see figure 2.13). These sensors are chosen because they are located at both ends and in the center of the beam tube. Their associated vapor pressure sensors are also connected to different valve blocks and thus their characteristic curves can be measured simultaneously.

Slope Method

Due to time constraints, only three slopes could be measured, one at 0.0 T and two at 0.7 T. The taken data for sensor **RTP-3-5102** can be seen in figure 3.5. The uncertainty on the vapor pressure temperature is given by the uncertainties described in subsections 3.3.1 and 3.3.2, while the uncertainty on the resistance measurement is given by the standard deviation of the reference precision resistor. This choice is due to the fact that the aim is not the measurement of a universally valid characteristic curve, but one for the use in the TES system. Therefore the characteristic curve only needs to be precise as long as the TES Pt500 readout is stable over a long period of time. With this choice the use of the data sheet values in subsection 3.3.1 with their gross overestimation of the achievable precision can be avoided.

A bootstrap fit of a linear function to the data with these uncertainties has been done for all three sensors. This yielded relative uncertainties on the slope of the function

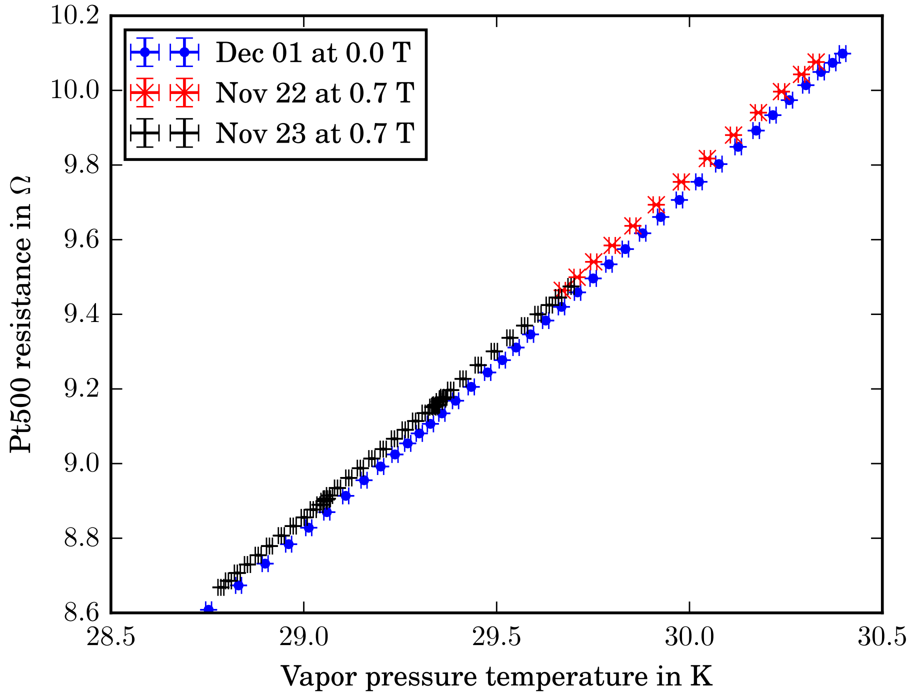

Figure 3.5.: Characteristic curve of RTP-3-5102 measured with Slope Method. Shown are data points from three days at two different magnetic field strengths 0.0 T and 0.7 T. For visualization purposes only every 10th data point is shown. A linear fit has been applied to the data points. The two fits at 0.7 T are in good agreement with each other. Fit parameters can be found in table 3.1

on the order of a few 0.1 %, and relative uncertainties on the y-axis intersect slightly below 1 %. For a Pt500 sensor calibrated at 30 K and a beam tube temperature of 30 K which fluctuates by ±30 mK the largest calculated uncertainty would add an uncertainty of 0.11 mK on the temperature at the outermost points of 30.03 K and 29.97 K to the absolute temperature uncertainty.

Supporting Point Method

Due to time constraints, measurements could only be taken at five temperatures. All measurement points were taken with an external magnetic field of 0.7 T. The taken supporting points calculated for sensor **RTP-3-5102** can be seen in figure 3.6. Each shown supporting point is the average of all resistance data points over the average of all temperature data points taken on one stop at one beam tube temperature. The uncertainty on the temperature of the supporting points are again given as the combined uncertainty of the vapor pressure related effects from subsection 3.3.2 and the standard uncertainty of the averaged temperature. The uncertainty on the resistance of the supporting points is given by the standard uncertainty of the averaged resistance.

For this method a linear bootstrap fit as well as a worst case estimation has been done for all three sensors. The bootstrap fit resulted in a relative uncertainty on the order of 0.3 % on the slope and 0.5 % on the y-axis intersect. The worst case estimation resulted in a relative uncertainty on the order of 1.3 % on the slope and 2.1 % on the y-axis intersect.

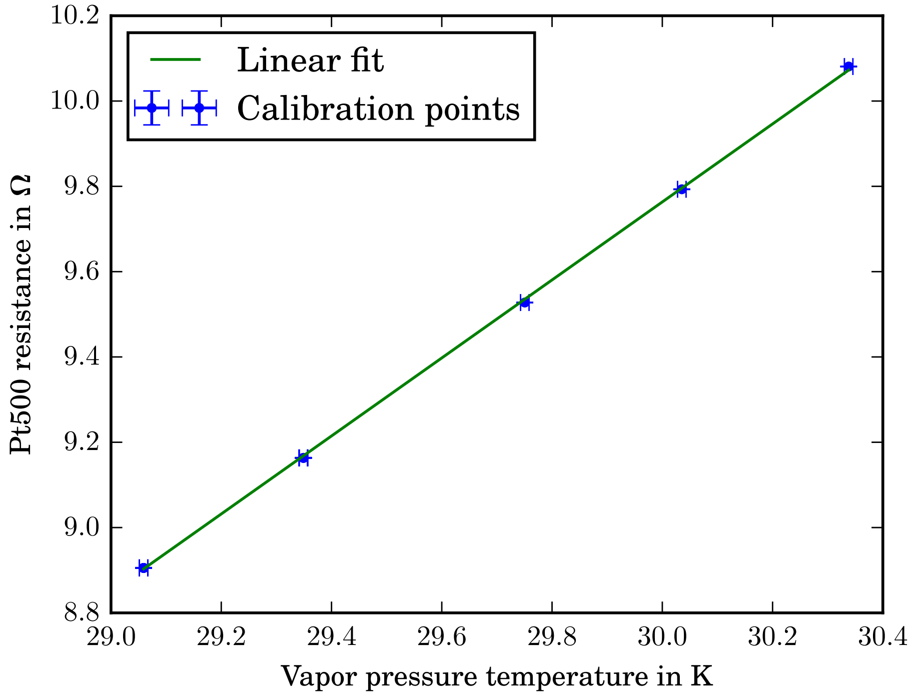

Figure 3.6.: Characteristic curve of RTP-3-5102 measured with Supporting Point Method. Shown are 5 data points which could be taken over the course of two days. A linear fit has been applied to the data points. Fit parameters can be found in table 3.1

During the measurements using the supporting point method, a systematic effect related to the dwell time at one temperature has been observed. As can be seen in figure 3.7, the measured resistance of the Pt500 sensor drops when the beam tube temperature stabilizes at one temperature. This behaviour has been observed for all three tested sensors. The cause for this might be a delay between a change of temperature in the vapor pressure sensor and Pt500 sensor due to different thermal contact to the beam tube.

This effect needs to be considered as a systematic effect for the slope calibration method. As no kinks indicating this effect are observed when the temperature is lowered without stops, the effect manifests itself there as an offset of the temperature which needs to be accounted for. The impact on the slope of the characteristic curve however does not appear to be influenced by this effect, as the fit results of both the slope and the supporting point method agree with each other as can be seen in table 3.1.

In summary, taking in-situ characteristic curves for the Pt500 sensors connected to the beam tube appears to be a feasible approach to gain reliable uncertainties on the Pt500 characteristic curves, but the details in regards to the procedure and systematic effects have to be considered in more detail. A worst case estimation of the uncertainty due to the Pt500 characteristic curve leads to an additional uncertainty on the temperature measurement of 0.4 mK.

Uncertainty on the absolute temperature measurement

The uncertainty on the absolute temperature measurement is calculated from the uncertainties detailed above by building the quadratic sum according to the GUM under

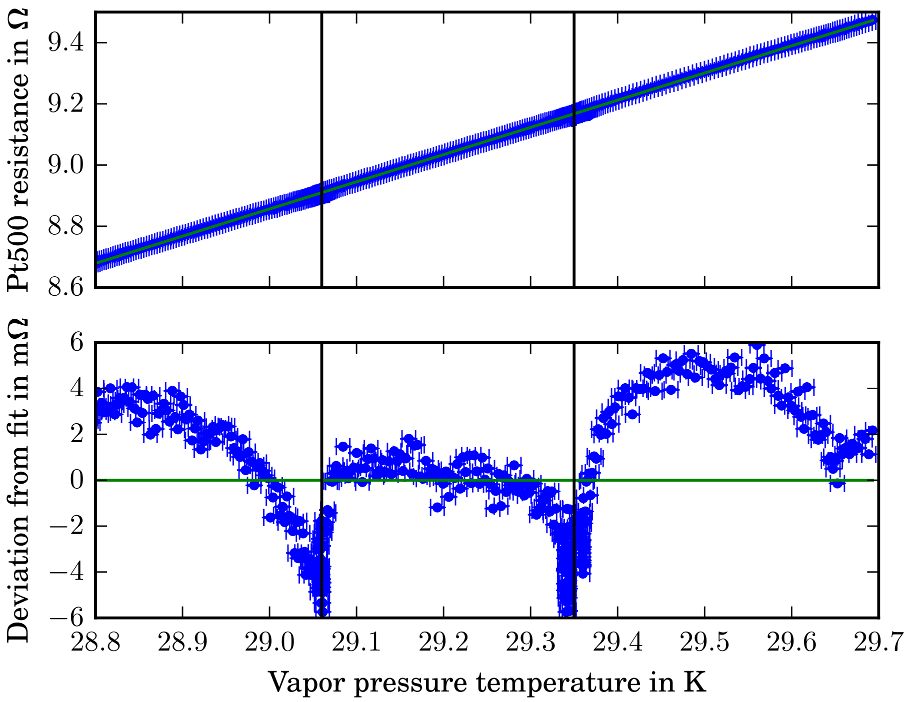

Figure 3.7.: Observed dwell time effect during characteristic curve measurement. Shown at the top is the fitted characteristic curve of sensor **RTP-3-5102**. Below that is the deviation of the data points from the fit. The temperatures at which the beam tube temperature was stabilized are shown as black vertical lines.

Table 3.1.: Results of linear fits to measured characteristic curves. Shown are the fit results for the linear fits to sensor **RTP-3-5102**. Considering the calculated uncertainties, all three approaches lead to compatible fit parameters.

Parameter	RTP35102
Slope y-intersect in Ω	-17.763 ± 0.042
Slope slope in Ω/K	0.916 ± 0.001
Supporting Point y-intersect in Ω	-17.657 ± 0.084
Supporting Point slope in Ω/K	0.914 ± 0.003
Worst case y-intersect in Ω	-17.807 ± 0.357
Worst case slope in Ω/K	0.919 ± 0.012

Table 3.2.: Absolute temperature calibration uncertainty. The combined uncertainty on the absolute temperature measurement achieved by quadratic summation of all component uncertainties according to the GUM fulfills the uncertainty requirement of $\sigma < 10\,\mathrm{mK}$.

Source of uncertainty	Uncertainty in mK
Pt500 instrumentation	0.50
Vapor pressure instrumentation	1.21
Thermomolecular effect	0.20
Aerostatic systematic effects	0.20
Temperature gradient	0.29
Uncertainty of saturation vapor pressure	8.14
Interpolation uncertainty	0.18
Pt500 characteristic curve uncertainty	0.40
Combined Uncertainty	8.27

the assumption of uncorrelated uncertainties:

$$\sigma_{\mathrm{tot}} = \sqrt{\sigma_1^2 + ... + \sigma_n^2}\ . \tag{3.36}$$

Summarizing all uncertainties in this way leads to a combined uncertainty of

$$\sigma_{\mathrm{abs}} = 8.27\,\mathrm{mK}\ . \tag{3.37}$$

This is below the requirement on the accuracy of 10 mK, and is therefore capable of measuring the beam tube temperature for nominal KATRIN operation. As one can easily see from table 3.2, the major uncertainty contributing to the accuracy of the absolute temperature measurement is the uncertainty of the saturation vapor pressure curve. Without this uncertainty, the combined uncertainty is reduced to 1.38 mK. As the TES saves the raw resistance data of the Pt500 sensors and pressure of the pressure values of the transducers, it is in principle possible to recalibrate the data at a later point in time if a saturation pressure curve with better accuracy becomes available. Similarly, temperatures can be recalculated with a Pt500 characteristic curve with lower uncertainty if it becomes available or is measured.

Uncertainty on the relative temperature measurement

Most of the uncertainties listed in table 3.2 only have an impact on the calibration constant which is implemented as an offset on the measured temperature. Therefore, they need not to be considered for the relative temperature measurement. Hence, the uncertainty on the relative temperature measurement is dominated by the instrumentation uncertainty of the Pt500 read out and, the linear interpolation of the characteristic curve, and the characteristic curve itself. This leads to a combined uncertainty of

$$\sigma_{\mathrm{rel}} = 0.67\,\mathrm{mK} \tag{3.38}$$

on the relative temperature measurement. Compared to the requirement of 10 mK precision, this achieved precision is better by about a factor of 15.

Summary

The KATRIN requirement on the temperature measurement are fulfilled and surpassed. The relative temperature measurement can be done with a precision about 15 times better than required. While the absolute temperature measurement also fulfills the requirements, it does so without much uncertainty budget left. The impact of the estimated uncertainty on the Pt500 curve, even as a worst case estimation, does not significantly contribute to this uncertainty.

If a saturation pressure curve or Pt500 characteristic curve with lower uncertainty will be available in the future, these can be also be applied to already taken data. This theoretically allows for a post measurement reduction of the uncertainty down to 1.37 mK for curves with insignificant uncertainties.

3.4. Reproducibility of calibration

The Pt500 sensors of the TES need to be calibrated according to section 3.2 to achieve the required accuracy to measure te beam tube temperature (see section 3.3). For the operation of KATRIN, it is important to determine how stable the calibration constants gained by the calibration procedure are and how often a recalibration of the system is necessary.

To investigate this stability, the Pt500 sensors have been calibrated several times. Inbetween, the temperature of the beam tube has not been changed. Potential hysteresis effects due to the magnetic field in the source cryostat are examined and the findings described in subsection 3.4.1. The stability over time is investigated in subsection 3.4.2. The results are then discussed in subsection 3.4.3.

3.4.1. Influence of external magnetic fields on the stability of the calibration factors

The high magnetic fields of up to 3.6 T and 5.5 T inside the WGTS cryostat have a significant effect on the Pt500 sensors, which has been studied in [Ram12] and is illustrated in figure 3.8. This is one of the main reasons why an in-situ calibration is necessary.

What has not been researched yet in prior works is the possibility of hysteresis effects. To investigate whether hysteresis effects exist, which affect the calibration factors, two calibration runs of all Pt500 sensors have been done, the first on 15. Nov 2016 and the second on 21. Nov 2016. Between both calibration runs, the temperature set point of the beam tube has not been changed, but the magnetic field has been increased from 20 % at the first calibration to 30 % for 1 d before returning to 20 % at the second calibration.

To compare both calibration runs, the difference between the calibration constants of each sensor have been plotted into the histogram seen in figure 3.9. If the outlier at $-8\,\mathrm{m}\Omega$ is disregarded as a result of a calibration mistake, the resulting distribution has a mean of -0.66 mK and a standard deviation of $1.75\,\mathrm{m}\Omega$. This means that the measurement is in good agreement with a vanishing effect due to hysteresis or drift. The spread of the distribution can be explained mostly by the combined uncertainty on the measurement due to the Pt500 and vapor pressure of $1.24\,\mathrm{m}\Omega$.

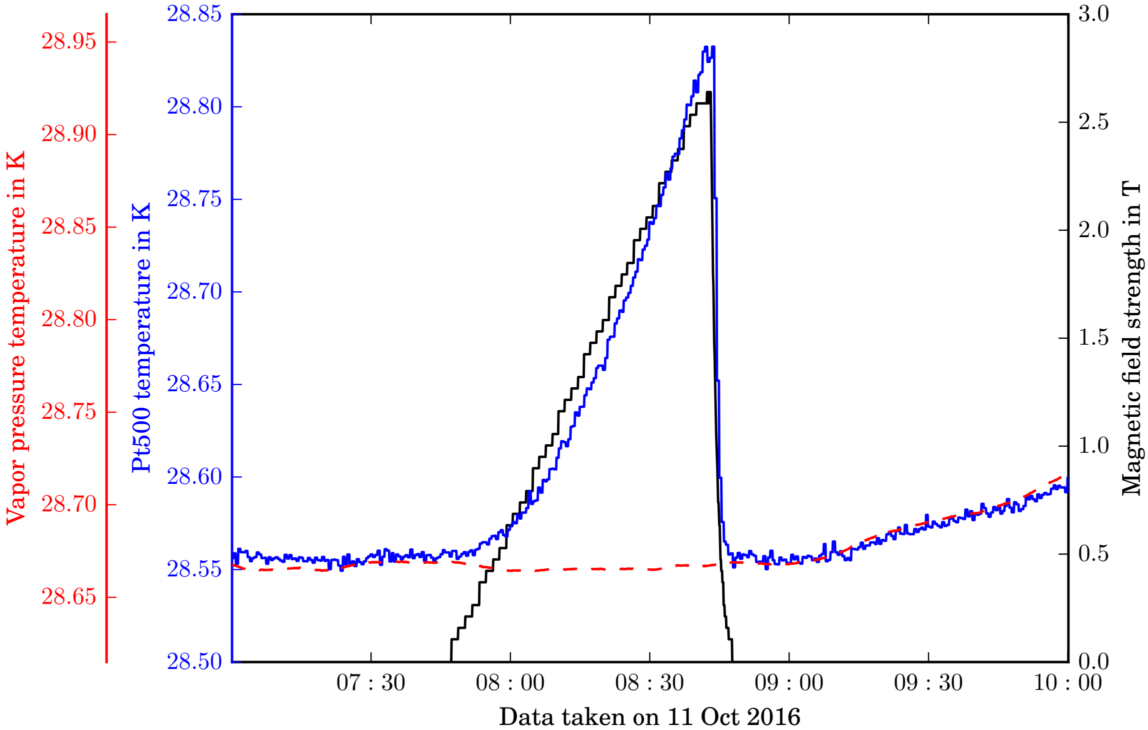

Figure 3.8.: Influence of external magnetic on Pt500 temperature measurement. Shown are the temperatures measured both via an uncalibrated Pt500 sensor (blue) and via a vapor pressure sensor (red) in the external magnetic field (black) of the WGTS cryostat. The temperature measured by the Pt500 sensor and the vapor pressure sensor behave similarly until a magnetic field is applied. The magnetic field causes a rise in the Pt500 temperature by increasing the sensor's resistance via magnetoresistance. As soon as the magnetic field is shut down, the Pt500 sensor temperature returns to the previous level. During the entire duration of the rise in Pt500 temperature the vapor pressure temperature does not change significantly. Hence, the temperature of the beam tube did not change, only the resistance of the Pt500 sensor at this temperature.

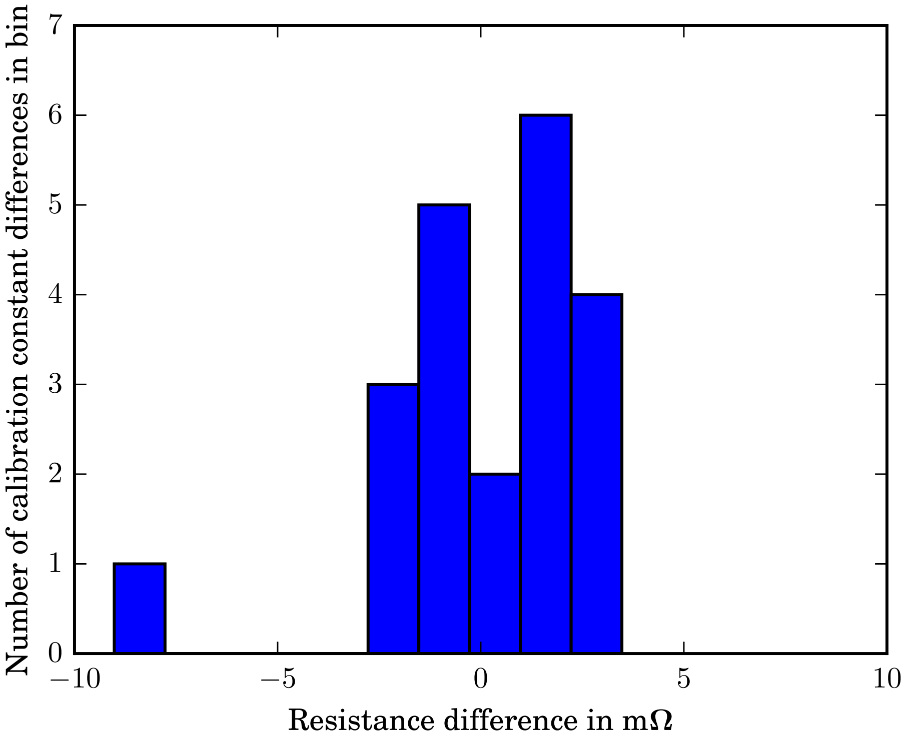

Figure 3.9.: Hysteresis of calibration constants. Shown are the differences between calibration constants of two calibration runs. No significant hysteresis effects nor any drift over time can be observed.

3.4.2. Stability of calibration factors over time

Due to time constraints during measurement phase, especially with regard to the magnetic field of the WGTS cryostat, long term stability measurements of the calibration constants without a magnetic field were not feasible.

An upper boundary on the drift of calibration constants over time can be gained despite this by analyzing the data from subsection 3.4.1 once more. Again, disregarding the outlier data point in figure 3.9, the mean of the distribution of calibration constant shifts is at $0.65\,\mathrm{m}\Omega$, which at $30\,\mathrm{K}$ leads to a shift in temperature of $(-0.66 \pm 2.77)\,\mathrm{mK}$.

The two calibration runs used for this analysis were separated by a duration of $6\,\mathrm{d}$, which leads to an average shift of $(-0.11 \pm 0.46)\,\mathrm{mK/d}$. With this value in combination with the remaining uncertainty budget calculated from the requirement of $10\,\mathrm{mK}$ and the uncertainty on the absolute temperature measurement of $8.27\,\mathrm{mK}$, one can derive an estimation of the number of days until a recalibration becomes necessary:

$$t_{\mathrm{recalibration}} = \left| \frac{\sqrt{(10\,\mathrm{mK})^2 - (8.27\,\mathrm{mK})^2}}{-0.08\,\mathrm{mK/d}} \right| \;, \tag{3.39}$$

$$t_{\mathrm{recalibration}} = (51.1 \pm 214.4)\,\mathrm{d} \;. \tag{3.40}$$

3.4.3. Discussion of calibration factor stability

Measurements have shown that no significant effect on the calibration constants of the Pt500 sensors due to hysteresis is observed. This indicates that switching between different WGTS cryostat magnetic fields at which prior calibrations exist, could be possible without recalibration, although a more detailed investigation into the effect of higher magnetic field strengths and longer durations is necessary to make a conclusive statement.

An estimate of time stability has been derived, which necessitates a recalibration every (51.1 ± 214.4) d. As the uncertainty on this value is very big a more thourough investigation is needed to decide whether recalibration during a KATRIN measurement run is necessary.

As the constraints of the KATRIN measurement campaign have only allowed for investigation of small time scales and low magnetic fields in comparison to a nominal KATRIN measurement run, it would be preferrable to verify the results presented in this chapter under nominal conditions and confirm or disprove the need for recalibration during a measurement run.

3.5. Conclusion and implications for KATRIN

A calibration procedure for the Pt500 sensors via the TES system has been devised and tested. It allows for the repeatable calibration of all 24 sensors on the beam tube and 4 sensors in the pump ports in a time span of just two workdays.

The calibration constants obtained with this procedure are possibly stable over time on the scale needed for a KATRIN measurement run and show no hysteresis effects due to changing external magnetic fields. Therefore further research is necessary to confirm whether recalibration of the TES system is only necessary between measurement runs. This is important as a confirmations means that no measurement time is used up for calibration. It also allows changing the magnetic field strength during a measurement run without need for recalibration, as long as a calibration at the target magnetic field has been done before the start of the measurement run.

All associated uncertainties of the Pt500 calibration are within the specifications of 10 mK for the beam tube temperature measurement. It is therefore possible to reliably measure the beam tube temperature and verify whether the homogeneity and stability requirements are met. With the confirmation of this fact, the research done in chapter 4 is based on a solid foundation.

4. Measurement of temperature stability and homogeneity of beam tube

With the calibrated temperature measurement system described in the previous chapter 3 the temperature of the WGTS beam tube can be measured with an accuracy of better than 10 mK on the absolute temperature and an accuracy of 0.67 mK on the relative temperature measurement. The temperature data gained with these sensors over the course of the KATRIN measurement campaign Aug 2016 - Dez 2016 is analyzed using SciPy [Jon01] and discussed in this chapter.

The measurement method together with the boundary conditions of WGTS cryostat parameters necessary for measurements are described in section 4.1. In section 4.2 the stability of the WGTS beam tube is calculated, remaining temperature fluctuations analyzed, and correlations to other WGTS cryostat components investigated. A similar focus is placed on the temperature homogeneity of the WGTS beam tube in section 4.3. The results of these two sections are then discussed in section 4.4 and their impact on KATRIN presented in section 4.5.

4.1. Description of the measurement and boundary conditions

In order to be representative for nominal KATRIN operations, several boundary conditions have to be fulfilled for the measurements of temperature stability and homogeneity of the beam tube:

- Beam tube cooled down,
- Two-phase heater regulation activated,
- Stable the gHe supply,
- Stable magnetic field.

For the detailed description of the components, see subsections 2.4.1 and 2.4.2. The concrete requirements on the above mentioned boundary conditions are described in detail in the following.

Beam tube cooled down The WGTS beam tube has to be in the temperature region of ~27.2 K to ~36.8 K for calibration of the Pt500 sensors to be possible. Below

~27.2 K, the two-phase mixture in bulbs and evaporator tubes would be in danger of underpressure compared to the outside atmosphere, allowing air to leak into the systems. At high pressures the bulb capillaries might burst and are thus protected by burst-disks, which open at pressures above 9 bar, corresponding to a temperature of ~36.8 K. Furthermore, to get representative results for nominal KATRIN operation the temperature should be in the nominal temperature range of 28 K to 32 K (see subsection 2.3.2). This requirement already limits the usable data to the time span from 15. Oct 2016 to 1. Dec 2016. The time range this requirement is fulfilled for is marked by the red box in figure 4.1.

Two-phase heater regulation activated The 4 heaters with 2 W maximum power respectively, located inside the evaporator tubes brazed to the WGTS beam tube, are essential for the temperature regulation of the beam tube. Their importance for the stability can be seen immediately in figure 4.2 as after the activation of their regulation on the 28. Oct 2016 the temperature is almost constant.

Stability of the gHe supply As the gHe circuit is used to cool the neon condensers of the two-phase neon cooling system, temperature fluctuations of this circuit cause temperature fluctuations of the beam tube. It is therefore necessary that the gHe circuit is sufficiently stable. This point is discussed in more detail in subsection 4.2.3.

Stable magnetic field The magnetic field strength inside the cryostat has to be stable as the temperature signal of the Pt500 sensors changes with the external magnetic field. To measure accurate results, the Pt500 sensors have to be calibrated at each new combination of temperature and magnetic field strength. As the calibration procedure takes on the order of two days the magnetic field strength needs to be stable over at least this period before measurements can be taken. The projected stability of the magnetic field according to the KATRIN design report is 0.2 %, resulting in fluctuations of up to 7.2 mT. Considering the behavior of the Pt500 sensors as observed in figure 3.8, the specified stability of the magnetic field should not lead to a significant effect on the temperature measurement.

For the analysis in the following sections only data that fulfills the above mentioned criteria has been chosen. The concrete intervals used for the analysis are marked in figure 4.2.

All data used in the analysis is taken from the KATRIN ADEI system unless explicitly stated otherwise. Besides the data from the ADEI database, there is also the data logged internally by the TES system. This data contains values which are not transmitted to the ADEI database such as the raw Pt500 resistance or the bulb vapor pressure. As mentioned in section 3.1, the sampling rate of the TES is 1/30 Hz while the ADEI logs values at a frequency of around 1/5 Hz. Furthermore, the TES and the ADEI system are not synchronized. Therefore mixing data from both systems in a single analysis has been avoided.

The choice of focusing on data recorded in the ADEI system is based on the fact that ADEI contains data from more sensors than those covered by the TES. Among this additional data are more temperature sensors throughout the WGTS cryostat, the current in the superconducting solenoids, the power of the beam tube heaters, and the pressure inside the two-phase beam tube cooling system. This allows for the

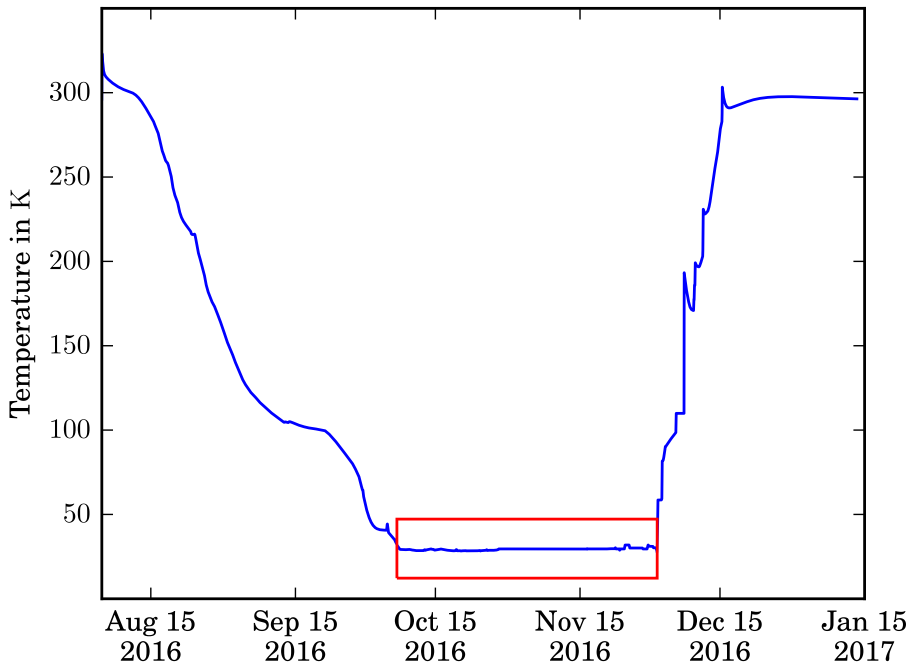

Figure 4.1.: Overview of temperature data of measurement campaign. Representative data of one Pt500 sensor at the beam tube of complete data set taken during the measurement campaign from Aug 2016 to Dez 2016. The interval that satisfied the minimum requirement of a beam tube temperature in the range of 28 K to 32 K is marked by the red box. The small temperature peak to the left of the red box is caused by the filling of the two-phase evaporator tubes on the beam tube. As can be seen, the cooldown of the WGTS beam tube takes significantly longer than the warmup phase. This is, in part, due to comissioning tests, such as the leak tests at around 100 K after the mid of September, being done.

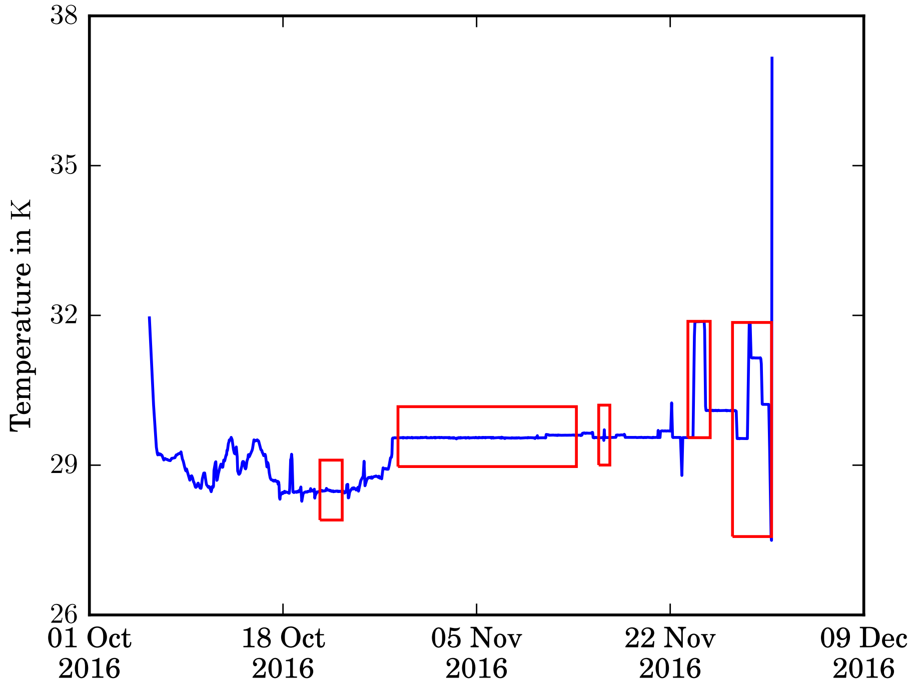

Figure 4.2.: Overview of temperature data used for analysis. Shown is a magnification of the marked area in figure 4.1. Intervals that were used for analysis in the following chapters are marked in red.

analysis of correlations between the sensors along the beam tube and other sensors, e.g. temperature sensors of other cooling circuits, inside the WGTS cryostat.

A problem with using the ADEI data for analysis of the beam tube temperature is the digital oversampling due to the differing logging frequencies of ADEI and TES which leads to steps of around 6 data points with identical temperature values in the ADEI data. When calculating the mean or standard deviation of the temperature the impact of these additional data points is limited to the borders of the chosen data interval. Inside the interval a duplication of all data points does not change the mean or standard deviation. Depending on the choice of the interval, however, not all ADEI data points representing one TES data point are included. For an interval with a duration of 1 h, a temperature randomly distributed around 30 K with a standard deviation of 1 mK / 10 mK this effect can lead to a deviation of the mean on the order of 10^{-2} mK / 10^{-2} mK. The effect on the standard deviation is on the order of 10^{-2} mK / <0.15 mK. Not considering this effect in analysis would lead to an increase of less than 1 % in the uncertainty on the relative temperature measurement and an increase on the order of 10^{-5} in the uncertainty on the absolute temperature measurement for both 1 mK and 10 mK. It is therefore disregarded in the following. For longer time periods the effect becomes even less significant.
Care has to be taken, however, when computing the standard uncertainty of the mean, as here the number of data points n enters the equation with $1/\sqrt{n}$. In this case, the number of ADEI data points has to be divided by 6 in order to get the true number of measured data points.

4.2. Measurement of temperature stability

The KATRIN requirement on the temperature stability of the WGTS beam tube is ±30 mK/h [Ang05]. This stability needs to be calculated from the temperature measurement with the Pt500 sensors. For each sensor, the stability is defined as the standard deviation of the temperature data points.

With this definition, the method used to evaluate the data will be described in subsection 4.2.1. The results of this analysis are then presented in subsection 4.2.2. Finally, it is looked at the reproducibility of the achieved stability in subsection 4.2.3, as it is essential that the stability requirement can be met over the duration of a KATRIN measurement phase of 60 d.

4.2.1. Method of data evaluation

To determine the temperature stability of the WGTS beam tube temperature, time spans in which the conditions listed in section 4.1 are fulfilled are chosen. The Pt500 temperature data of these time spans is taken from the ADEI system. A time period of 1 h, as specified for KATRIN operation, is chosen and the standard deviation of the temperature data for each sensor calculated and taken as the stability over the 1 h time frame. This standard deviation was calculated using the NumPy function `numpy.std` [Jon01]. The uncertainty on this stability is given by the uncertainty on the relative temperature measurement σ_{rel} calculated in section 3.5.

4.2.2. Achieved temperature stability

The results of the achieved temperature stability are presented in this subsection. The data used for this analysis was taken on the 28th of November 2016 from 22:00 until 23:00 where the operational parameters of the WGTS cryostat were set to the following values:

- a heater set point of 2 bar corresponding to a temperature of 29.56 K,
- an average temperature of the gHe-circuit used to cool the two-phase neon cooling system condenser of 27.8 K measured at the inlet of the gHe-circuit with sensor **RTT-2-3118**,
- and a current of around 62 A in the central WGTS cryostat superconducting solenoids measured with sensor **REI-5-3111**, corresponding to a magnetic field of around 0.7 T.

Exemplary results for sensor **RTP-3-5102** with regard to the 1 h measurement interval as specified for nominal KATRIN operation can be seen in figure 4.3. The stability as described in subsection 4.2.1 for this sensor is (1.10 ± 0.59) mK/h which is at worst a factor of 17.8 better than the requirement.

Similar results hold true for all sensors along the beam tube as can be seen from their stabilities listed in table 4.1. The temperature stability for all sensors during the selected 1 h period is in the range of 0.80 mK/h to 1.21 mK/h. This is at least a factor of 24 better than the required ±30 mK/h.

With this, the capability of the two-phase beam tube cooling system to achieve a temperature stability better than ±30 mK/h has been proven. In the next subsection it is investigated how representative the achieved stability of the evaluated time slot is.

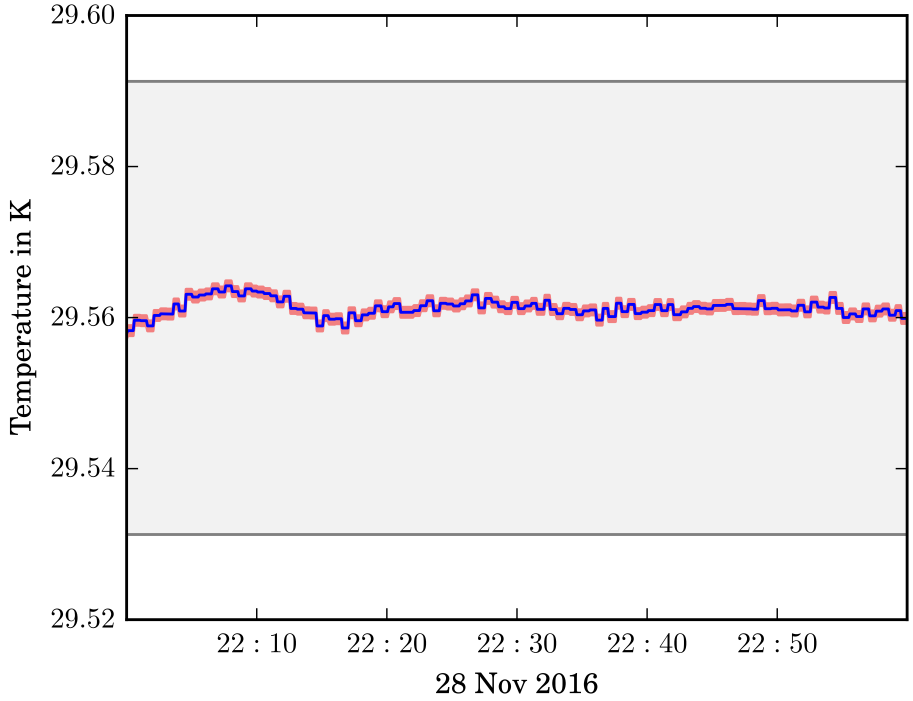

Figure 4.3.: Temperature stability of RTP-3-5102 over the time period of 1 hour. Shown is the temperature of sensor **RTP-3-5102** over the timespan from 22:00 to 23:00 on Nov 28 2016. The uncertainty on the temperature measurement is depicted as a red error band around the temperature signal. The stability requirement of $\pm 30\,\mathrm{mK/h}$ is displayed as a gray boundary around the mean of the temperature signal.

Table 4.1.: Temperature stability of all beam tube temperature sensors. Sensors **RTP-3-5106**, **RTP-3-5109**, and **RTP-3-5114** are defect and are thus not used for this analysis.

Sensor	Temperature stability in mK/h	Sensor	Temperature stability in mK/h
RTP-3-5101	1.15 ± 0.59	RTP-3-5113	0.82 ± 0.59
RTP-3-5102	1.10 ± 0.59	RTP-3-5115	1.01 ± 0.59
RTP-3-5103	0.99 ± 0.59	RTP-3-5116	1.02 ± 0.59
RTP-3-5104	1.21 ± 0.59	RTP-3-5117	1.05 ± 0.59
RTP-3-5105	1.08 ± 0.59	RTP-3-5118	1.05 ± 0.59
RTP-3-5107	1.04 ± 0.59	RTP-3-5119	0.95 ± 0.59
RTP-3-5108	1.09 ± 0.59	RTP-3-5120	0.99 ± 0.59
RTP-3-5110	1.06 ± 0.59	RTP-3-5121	1.12 ± 0.59
RTP-3-5111	0.84 ± 0.59	RTP-3-5122	1.01 ± 0.59
RTP-3-5112	0.80 ± 0.59	RTP-3-5123	1.01 ± 0.59
		RTP-3-5124	1.06 ± 0.59
		Range:	$(0.80–1.21) \pm 0.59$

4.2.3. Examination of the reproducibility of the achieved stability

For a KATRIN measurement phase of 60 d length, the results achieved in the previous subsection need to be achieved consistently over the duration of this 60 d period. To research this, the stability for 1 h periods has been calculated for the 16 d time span from 29. Oct 2016 to 13. Nov 2016. This span has been chosen as comparatively few changes to the operational parameters have been made during this period. It encompasses a total of 384 h of measurement time under nearly stationary conditions with the following settings for the operational parameters of the WGTS cryostat:

- a heater set point of 2 bar corresponding to a temperature of 29.56 K,
- three different settings for the gHe-circuit temperature with average temperatures measured with sensor **RTT-2-3118** of 28.3 K, 26.8 K and 27.8 K,
- and a current of around 62 A in the central WGTS cryostat superconducting solenoids measured with sensor **REI-5-3111**, corresponding to a magnetic field of around 0.7 T.

A histogram showing the results can be seen in figure 4.4. The average stability achieved during the analyzed 16 d time span was (3.28 ± 1.68) mK/h with a worst observed stability of 18.92 mK/h. As the average stability is a factor of 9.15 and even the worst observed stability at least a factor of 1.5 better than the requirement of 30 mK/h, the possibility of long term operation of the WGTS beam tube within the stability requirements for KATRIN measurement is highly probably. To confirm this, a measurement run under realistic conditions e.g. duration, stability of other WGTS components, would be preferable, but could not be performed in the scope of this thesis.

To research the impact of the fluctuations in the gHe-circuit which cools the two-phase neon condenser the time period between 09:00 and 19:00 on the 16. Nov 2016 has been evaluated. The operational parameters of the WGTS cryostat during this period were:

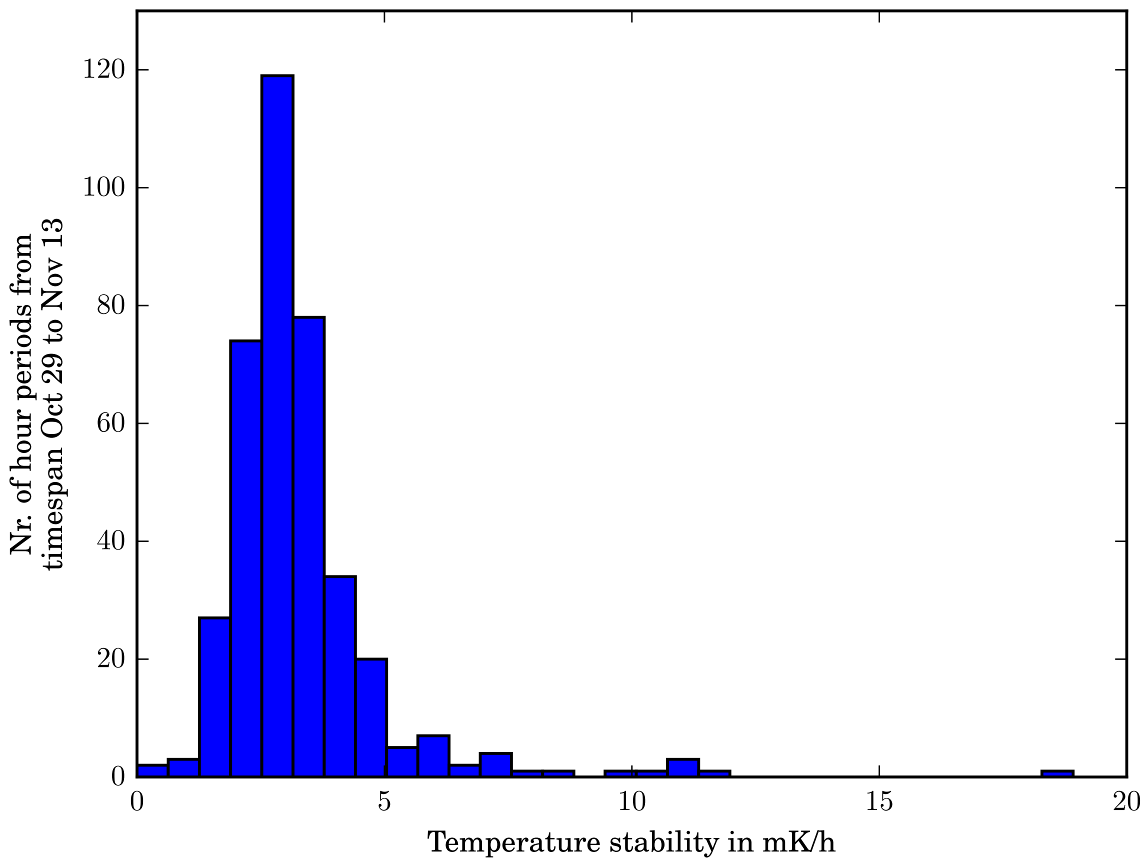

Figure 4.4.: Long-term temperature stability of the beam tube. Shown is a histogram of calculated stabilities for 1 h slices of the temperature data of **RTP-3-5102** between 29. Oct 2016 and 13. Nov 2016. A total of 2 data points are excluded from the analysis and not shown in the above graph. This is due to changes to the TES system a default value of 0 K was recorded.

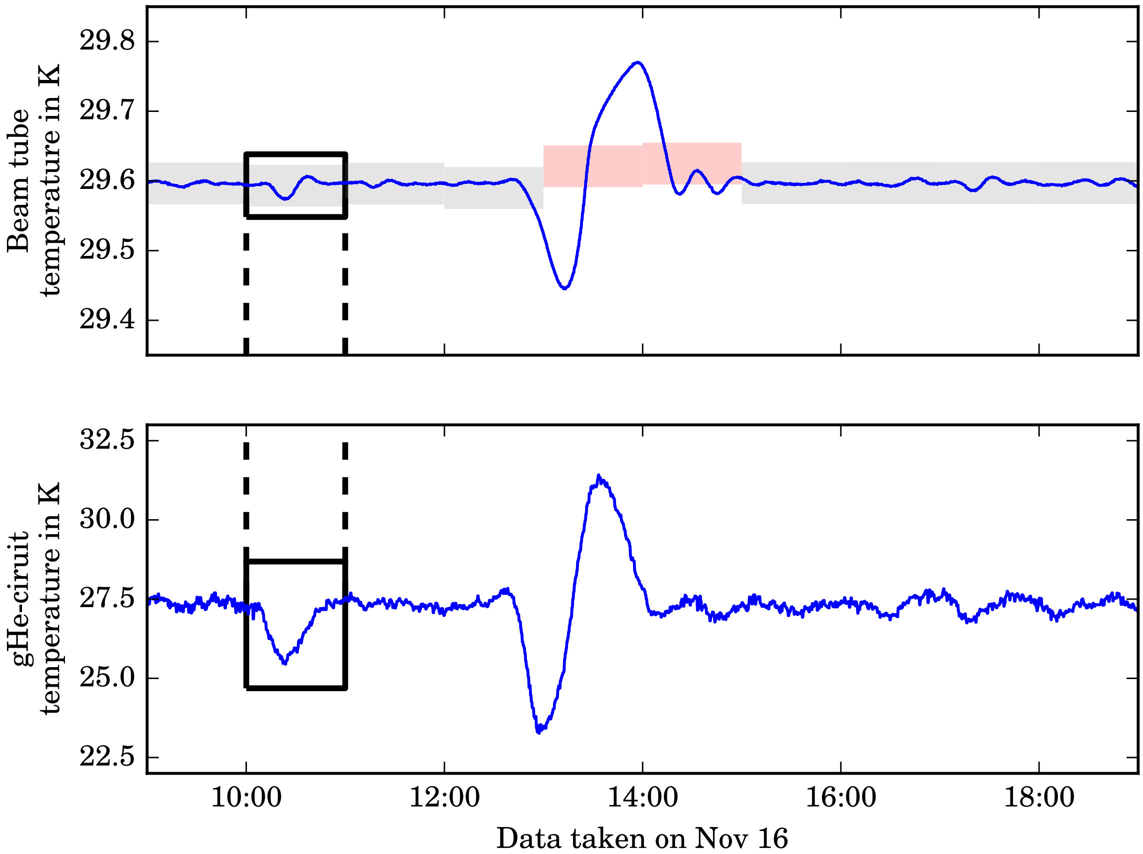

Figure 4.5.: Influence of gHe-circuit fluctuations on the temperature stability. Shown is the temperature of the beam tube (**RTP-3-5102**) at the top and that of the gHe-circuit (**RTT-2-3118**) at the bottom. The stability requirement for the specified 1 h measurement periods are marked in the top graph. Time periods where the requirement of 30 mK/h is met are colored gray while the periods where the requirements are violated are colored red. A large fluctuation in the gHe-circuit and the corresponding beam tube temperature fluctuation are framed in black. This time frame contains a large fluctuation, much above average, and is specifically selected to better show the effect the gHe-circuit has on the beam tube temperature.

- a heater set point of 2 bar corresponding to a temperature of 29.56 K,
- an average gHe-circuit temperature measured with sensor **RTT-2-3118** of 27.5 K,
- and no current in the central WGTS cryostat superconducting solenoids corresponding to no magnetic field.

The results can be seen in figure 4.5. The temperature fluctuation in the gHe circuit with a maximal deviation of 1.92 K during the 1 h period from 10:00 to 11:00 causes the stability to worsen to 8.59 mK/h, but does not result in a violation of the beam tube temperature stability requirements. In the period from 10:00 to 11:00, however, the temperature fluctuation with a maximal deviation of 3.95 K causes a fluctuation of 124 mK/h which is more than a factor of 4 worse than the requirement of 30 mK/h.

4.3. Measurement of temperature homogeneity

The KATRIN requirement on the temperature homogeneity of the WGTS beam tube is ±30 mK along 95 % of the beam tube [Ang05]. This means that the temperature between the center of the WGTS beam tube and each end must differ less than 30 mK. The method used to calculate the homogeneity is described in subsection 4.3.1. The results are presented in subsection 4.3.2.

4.3.1. Method of data evaluation

To determine the temperature homogeneity of the WGTS beam tube, the temperature signal of all Pt500 sensors from the ADEI is taken. An interval of 1 h is selected for easy comparability with the temperature stability. The temperature is then averaged over this 1 h interval.

For each temperature value gained this way the uncertainty is calculated according to section 3.3. The temperature values are then plotted against the sensor position along the beam tube. Furthermore, the maximum temperature differences between the n sensors in the center of the beam tube and the m sensors at one end of the beam tube are calculated for both front and rear side:

$$\Delta T_{\mathrm{max,front}} = \max\left(|T_{\mathrm{center},n} - T_{\mathrm{front},m}|\right) \ , \tag{4.1}$$

$$\Delta T_{\mathrm{max,rear}} = \max\left(|T_{\mathrm{center},n} - T_{\mathrm{rear},m}|\right) \ . \tag{4.2}$$

These differences are then compared to the homogeneity requirement of 30 mK. The uncertainty on these temperature differences are strongly correlated, as can be seen later in section 4.4. Therefore, simple quadratic addition of the uncertainties would neglect the correlation terms and underestimate the uncertainty. By adhering to the rules for uncertainty propagation the following equation for the total uncertainty σ_{tot} is valid:

$$\sigma_{\mathrm{tot}} = \sqrt{\sigma_{\mathrm{x}}^2 + \sigma_{\mathrm{y}}^2 + 2 \cdot \mathrm{Cov(X,Y)}} \ . \tag{4.3}$$

Here Cov(X, Y) is the covariance matix, given by

$$\mathrm{Cov(X,Y)} = \begin{pmatrix} \sigma_{\mathrm{x}}^2 & \rho_{\mathrm{x,y}} \cdot \sigma_{\mathrm{x}} \cdot \sigma_{\mathrm{y}} \\ \rho_{\mathrm{x,y}} \cdot \sigma_{\mathrm{y}} \cdot \sigma_{\mathrm{x}} & \sigma_{\mathrm{y}}^2 \end{pmatrix} \ . \tag{4.4}$$

Due to the high correlation between different sensors ($\rho_{\mathrm{x,y}} \sim 1$, for details see section 4.4, in particular figure 4.14), the off-diagonal entries of Cov(X, Y) can be approximated as $\sigma_{\mathrm{x}} \cdot \sigma_{\mathrm{y}}$. This approximation transforms the above term to

$$\sigma_{\mathrm{tot}} = \sqrt{\sigma_{\mathrm{x}}^2 + \sigma_{\mathrm{y}}^2 + 2 \cdot \sigma_{\mathrm{x}} \cdot \sigma_{\mathrm{y}}} \ , \tag{4.5}$$

$$\sigma_{\mathrm{tot}} = \sqrt{(\sigma_{\mathrm{x}} + \sigma_{\mathrm{y}})^2} \ , \tag{4.6}$$

$$\sigma_{\mathrm{tot}} = \sigma_{\mathrm{x}} + \sigma_{\mathrm{y}} \ . \tag{4.7}$$

Therefore, the uncertainty on the temperature homogeneity is given by

$$\sigma_{\mathrm{hom}} = \sigma(T_{\mathrm{center},n}) + \sigma(T_{\mathrm{front/rear},m}) \ . \tag{4.8}$$

At this point it important to keep in mind, that the two constituent uncertainties are defined as magnitudes of the deviation from the respective means, therefore no cancellations can occur.

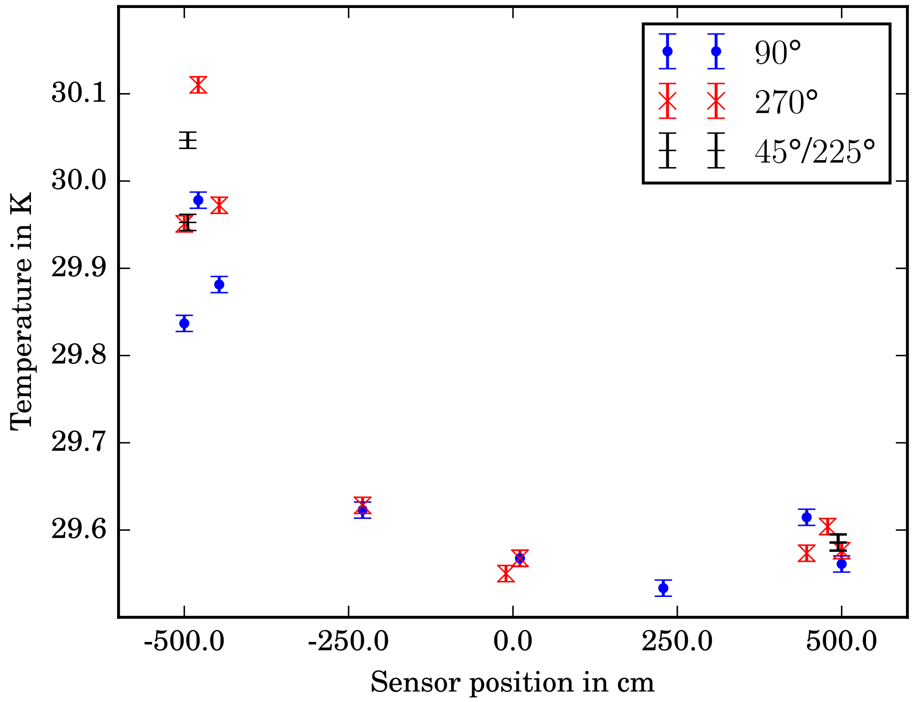

Figure 4.6.: Average temperature along beam tube. Shown is the average temperature over a duration of 1 h on Nov 28. The different colors indicate different azimuthal mounting points of the temperature sensors. For details on the sensor positions see figure 2.14.

4.3.2. Achieved homogeneity

The achieved results of the temperature homogeneity are presented in this subsection. The same data intervals as those used in section 4.2 are used in this analysis. In particular, the time period of 1 h on the 28th of November 2016 from 22:00 until 23:00, as well a part of the time period used to investigate long-term temperature stability from 29. Oct 2016 to 13. Nov 2016. For the operational parameters of the WGTS cryostat during these periods see subsection 4.2.2 and subsection 4.2.3 respectively.

For the temperature data taken on the 28th of November, the averaged temperature values can be seen in figure 4.6. The temperature measured with the sensors mounted on the rear side of the beam tube is systematically higher than the temperature measured in the center and towards the front side. The maximal deviation between center and rear side is (560.7 ± 16.2) mK, whereas the deviation between the center and the front side is only (64.1 ± 15.9) mK. The temperature difference between center and rear side is one order of magnitude higher than the requirement of ± 30 mK on the beam tube temperature homogeneity. In comparison the temperature difference between center and front side of the beam tube is only a factor of 1.8 above the homogeneity requirement.

The above analysis has been done for two time periods lasting 3 d during 29. Oct 2016 to 13. Nov 2016 in which the gHe-circuit temperature has not been changed. Both periods and the associated operational gHe temperature parameter of the WGTS cryostat are listed in the following.

- Period 1 from 29. Oct 2016 to 1. Nov 2016 at a gHe-temperature of 28.3 K,
- Period 2 from 4. Oct 2016 to 7. Nov 2016 at a gHe-temperature of 26.8 K.

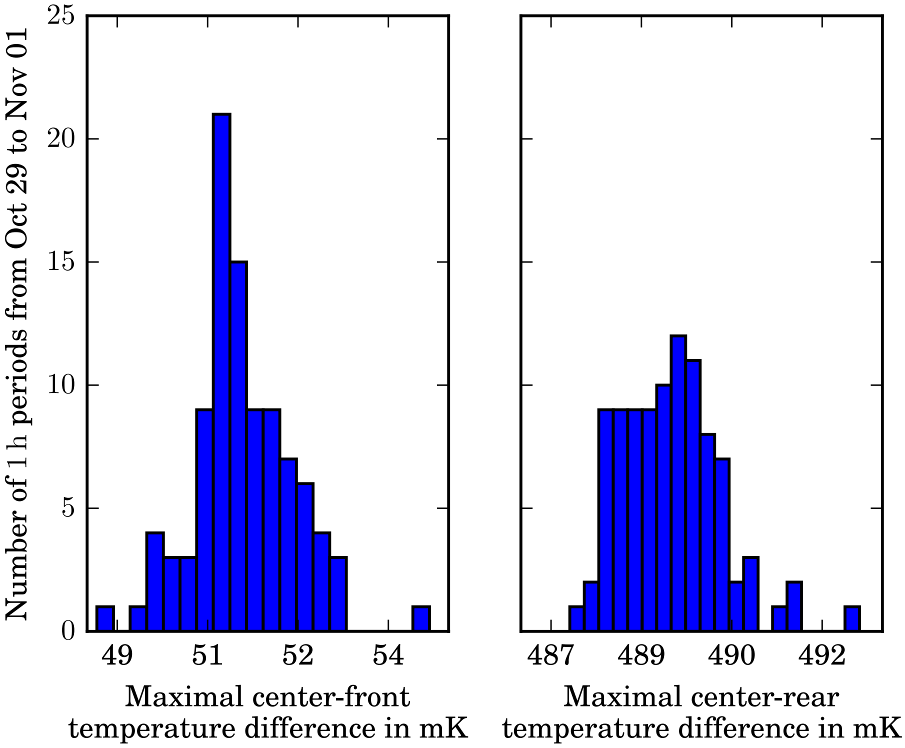

Figure 4.7.: Temperature homogeneity Oct 29 to Nov 1. Shown are histograms for the temperature difference between the center of the beam tube and both front and rear side.

The results for both time periods can be seen in figure 4.7 and figure 4.8 respectively. During period 1 an average maximal center to front inhomogeneity of (51.58 ± 0.84) mK and an average maximal center to rear inhomogeneity of (489.49 ± 0.83) mK have been found. These values are above the specified maximal deviation of 30 mK by a factor of 1.72 and 16.32. On top of the uncertainty on the values just given for the average inhomogeneity which includes the electronic readout noise of the Pt500 sensors, there is also a systematic effect of around 16 mK due to the uncertainty on the saturation vapor pressure curve (see subsection 3.3.2). This also holds true for the following results from period 2. During period 2 an average maximal center to front inhomogeneity of (48.26 ± 0.94) mK and an average maximal center to rear inhomogeneity of (558.01 ± 1.25) mK have been found. These values are above the specified maximal deviation of 30 mK by a factor of 1.61 and 18.60. These results show that the inhomogeneity of the beam tube temperature is consistently above the specified maximal allowed deviation between center and both ends. The difference between the values for the inhomogeneity during period 1 and 2 will be discussed in detail in section 4.4.

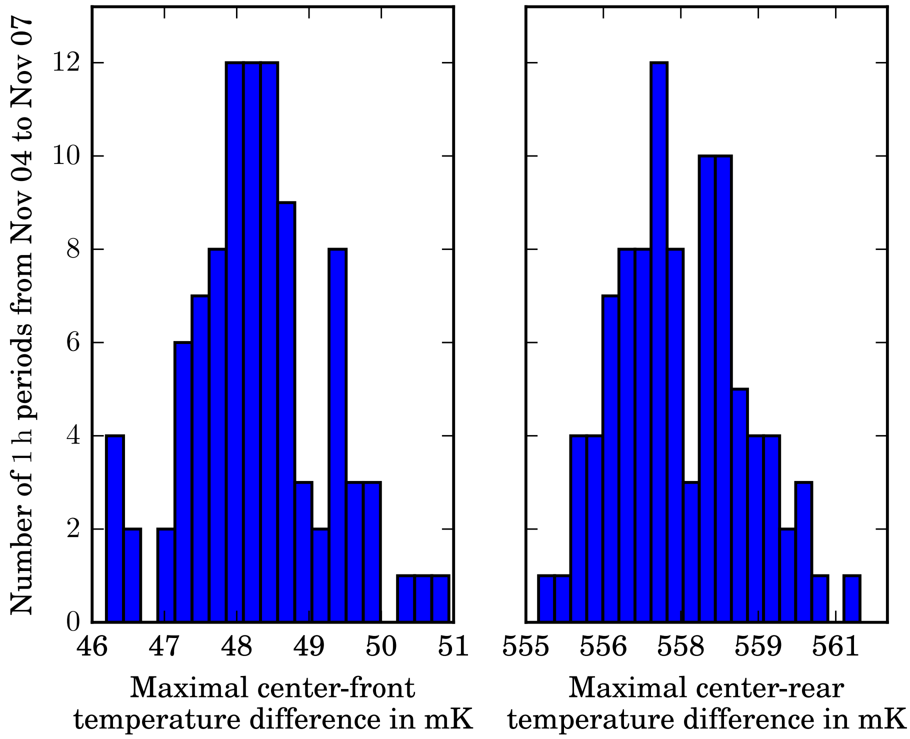

Figure 4.8.: Temperature homogeneity Nov 4 to Nov 7. Shown are histograms for the temperature difference between the center of the beam tube and both front and rear side.

4.4. Discussion of temperature stability and homogeneity results

In this section the results derived in the previous sections 4.2 and 4.3 are discussed in detail. The first paragraph addresses once more the temperature stability with regards to long term measurements. In the second paragraph, the influence of outside disturbances on the temperature stability is looked at and put into the context of correlations between different parts of the WGTS cryostat in the third paragraph. The fourth paragraph discusses the observed temperature inhomogeneity and puts it into the context of the prototype experiment Demonstrator. Paragraph five is a discussion of the observed dependence of temperature stability and homogeneity on the operational parameters of the WGTS cryostat. In the sixth paragraph the limitations on future measurements of the beam tube temperature are discussed.

Temperature stability

As presented in subsection 4.2.2, the KATRIN requirement of a temperature stability of the beam tube of better than 30 mK/h can be achieved reproducibly over time scales of days. Therefore, it is investigated whether the stability requirement of 30 mK can be met over time periods larger than 1 h. Following that the importance of the electrical heaters for the temperature stability is discussed.

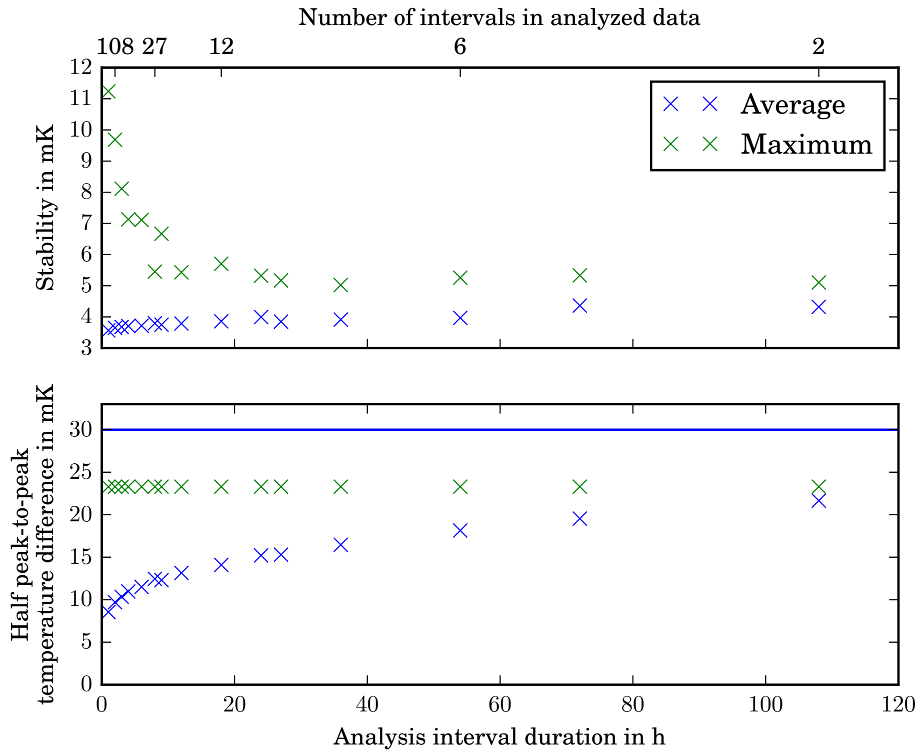

Figure 4.9.: Temperature stability dependence on measurement interval durations. Shown are the average over all intervals, as well as the maximum of all intervals of one analysis setting, of both the temperature stability and peak-to-peak temperature difference. These values are plotted as a function of the interval duration of each analysis setting. For easy comparison with the KATRIN stability requirement of ±30 mK, the peak-to-peak value is halved before plotting.

Longer measurement durations than 1 h

The time period from Oct 29 2016 to Nov 06 2016, containing a total measurement time of 216 h, is chosen for this analysis. This choice is made due to the stable operation during this period, as mentioned in subsection 4.2.3. The data is analyzed in a similar fashion for differing measurement interval lengths of whole hours, so that the interval length divides the measurement time of 216 h without remainder, leading to interval lengths ranging from the 1 h KATRIN specification up to 108 h, where only two intervals are included in the data. For each such analysis setting, an average stability value and the maximum (worst) observed stability is calculated.

For large interval durations, the temperature stability as defined over the standard deviation could hide violations of the 30 mK requirements. To address this issue, the peak-to-peak temperature value for each interval of each analysis setting has been calculated in addition to the standard deviation. The maximum of these peak-to-peak values serves as a worst case estimation of the stability. As can be seen in the results shown in figure 4.9, not only the stability, but also the maximum peak-to-peak value fulfill the temperature stability requirement for all chosen interval durations.

The average stability gets worse towards longer interval durations used for analysis up to a maximum of a factor of 1.22 above the value for 1 h intervals. The maximum (worst) stability drops towards longer intervals, which can be traced back to the above mentioned effect of the standard deviation calculation smoothing out fluctuations which are short compared to the measurement interval. Therefore, consideration of the peak-to-peak values becomes necessary. Whereas the average peak-to-peak temperature value gradually increases towards longer interval durations, the maximum peak-to-peak temperature value stays constant. The gradual increase is caused by a slow drift of about 5 mK over the course of 4 d, followed by a 10 mK kink over the duration of 2 d, which is suspected to be caused by a shift in the gHe-circuit temperature. On the other hand, the fact that the maximum peak-to-peak value stays constant means that the temperature fluctuation event with the biggest amplitude occurs on a timescale smaller than 1 h, and thus can be seen as a singular occurrence.

It can thus be assumed that for stationary operation of the WGTS cryostat, without changes to the operational parameters, the average stability and average peak-to-peak temperature value are independent on the measurement interval duration, with deviations from the mean caused by external influences. Furthermore, it can be concluded from these results, that from standpoint of the beam tube temperature stability KATRIN measurement cycles much longer than 1 h are possible without a significant impact on the systematic uncertainties compared to the design values.

Impact of two-phase heater on the temperature stability

In subsection 2.4.2 it has been stated that, due to its thermodynamic properties, a two-phase mixture of a liquid and gaseous substance is capable of self-regulating its temperature via an equilibrium of condensation and vaporization. In real applications this self-regulation is limited by an increase in pressure as liquid evaporates, caused by the finite size of the system. The active regulation via electrical heaters inside the evaporator tubes further improves upon this self-regulation by keeping the heat load on the system constant, thereby keeping the pressure constant and thus effectively creating an ideal two-phase system as shown in figure 2.9. To achieve this, the set point of the heater regulation combined with the temperature of the gHe-circuit need to allow for the heater power to never run into its limits of 0 W and 2 W per heater. If either limit is reached, the heater regulation cannot sustain the ideal two-phase system, thus negatively impacting the temperature stability.

This regulation is necessary to reach the KATRIN stability requirements on the beam tube temperature, as can be seen in figure 4.10. Without the heater regulation, the temperature of the beam tube is much less stable and directly affected by fluctuations of the gHe-circuit. Due to the importance of the heater regulation for the temperature stability, its correlation to the beam tube temperature will be discussed in detail in the following paragraph.

Temperature correlations

In order to investigate fluctuations of the temperature and determine their cause, a correlation analysis as well as a Fourier analysis of the temperature signal is done. A correlation analysis between two sensors X and Y is done by forming the Pearson product-moment correlation coefficient $\rho_{\mathrm{X,Y}}$. It is defined as follows [Hal15]:

$$\rho_{\mathrm{X,Y}} = \frac{\mathrm{Cov}(X,Y)}{\sigma_{\mathrm{X}} \cdot \sigma_{\mathrm{Y}}} \ , \tag{4.9}$$

$$\rho_{\mathrm{X,Y,r}} = \frac{\sum_{i=1}^{n}(x_i - \bar{x})(y_i - \bar{y})}{\sqrt{\sum_{i=1}^{n}(x_i - \bar{x})^2} \cdot \sqrt{\sum_{i=1}^{n}(y_i - \bar{y})^2}} \ , \tag{4.10}$$

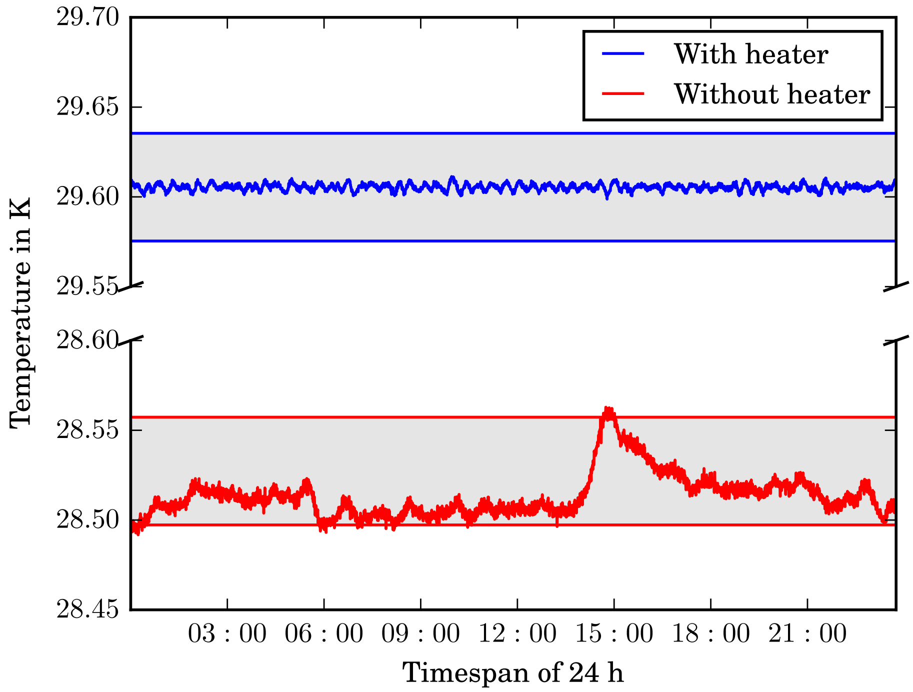

Figure 4.10.: Temperature stability due to heater regulation. Shown is temperature data from Oct 22 2016 where the heater regulation is not activated and temperature data from Nov 12 2016 where the heater regulation is active. As can be seen, the temperature stability is significantly worse without the heater regulation. The KATRIN requirement of ±30 mK is shown in gray, but only needs to be fulfilled for intervals of 1 h length. As the stability can be heavily influenced by outside influences such as the gHe-circuit, an entire day was evaluated for the sake of proper representation of the average behavior.

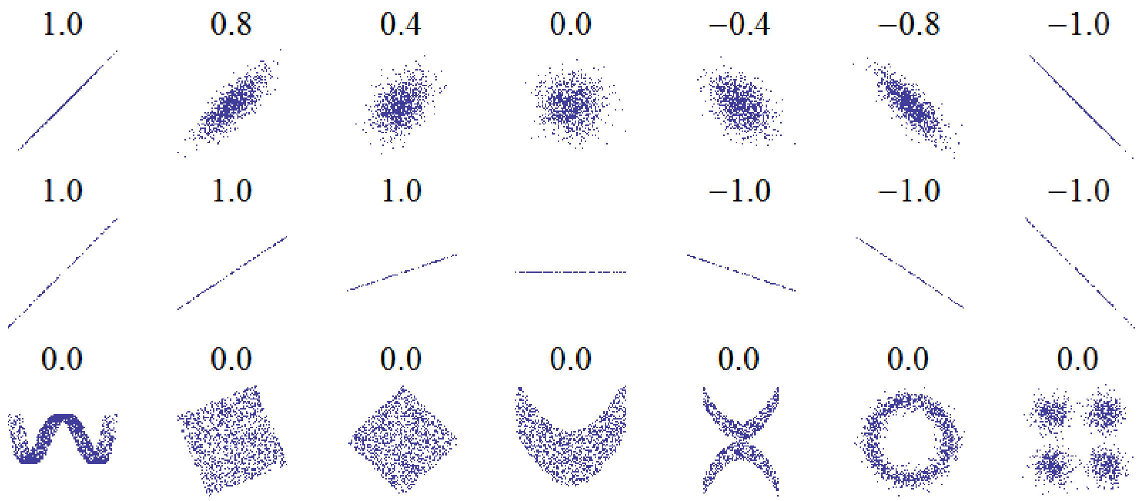

Figure 4.11.: Graphical interpretation of the Pearson product-moment correlation coefficient. Shown are several distributions of data points and their associated correlation coefficient. The Pearson correlation coefficient is only representative for the correlation between two quantities in case of linear correlation. Image from [Ima08] (public domain).

with:

- the covariance $\mathrm{Cov}(X,Y) = \frac{1}{n}\sum_{i=1}^{n}(x_i - \bar{x})(y_i - \bar{y})$ of X and Y,
- the standard deviations σ_{X} and σ_{Y} of X and Y given by $\sigma = \sqrt{\frac{1}{n}\sum_{i=1}^{n}(z_i - \bar{z})}$,
- the data points x_i and y_i of X and Y taken at the same time,
- and the empirical correlation coefficient $\rho_{\mathrm{X,Y,r}}$.

This coefficient is a way to quantify the linear correlation between two quantities. The closer the correlation coefficient is to 1, the more two quantities are correlated. The closer the correlation coefficient is to -1, the more two quantities are anti-correlated. If the correlation coefficient is 0, the two quantities are not linearly correlated. The calculation of the correlation coefficient is done with the the NumPy function `numpy.corrcoef` [Jon01]. As can be seen in figure 4.11, this correlation coefficient is not able to reflect complex, non-linear dependencies between two quantities.

Correlation along the beam tube

To investigate the correlation of the temperature along the beam tube, the time period from Nov 24 to Nov 25 has been used. In this chosen interval, the temperature of the beam tube has been changed from to 29.56 K up to 31.85 K and down to 30.10 K again. This choice is made due to the fact that during stationary operation the temperature stability of the beam tube is on the same order as the Pt500 read out noise. Under this condition, even for a perfect linear correlation between the underlying physical temperatures, corresponding to a correlation coefficient of $\rho = 1$, analysis of the measured temperature data will result in a lower correlation coefficient ρ_{r} as can be seen in figure 4.12.

An exemplary correlation plot for the analyzed time period between sensors **RTP-3-5102** and **RTP-3-5123** on opposite ends of the beam tube is shown in figure 4.13. The associated correlation coefficient for this data is $\rho_{\mathrm{r}} = 0.9999$ with a p-value, meaning

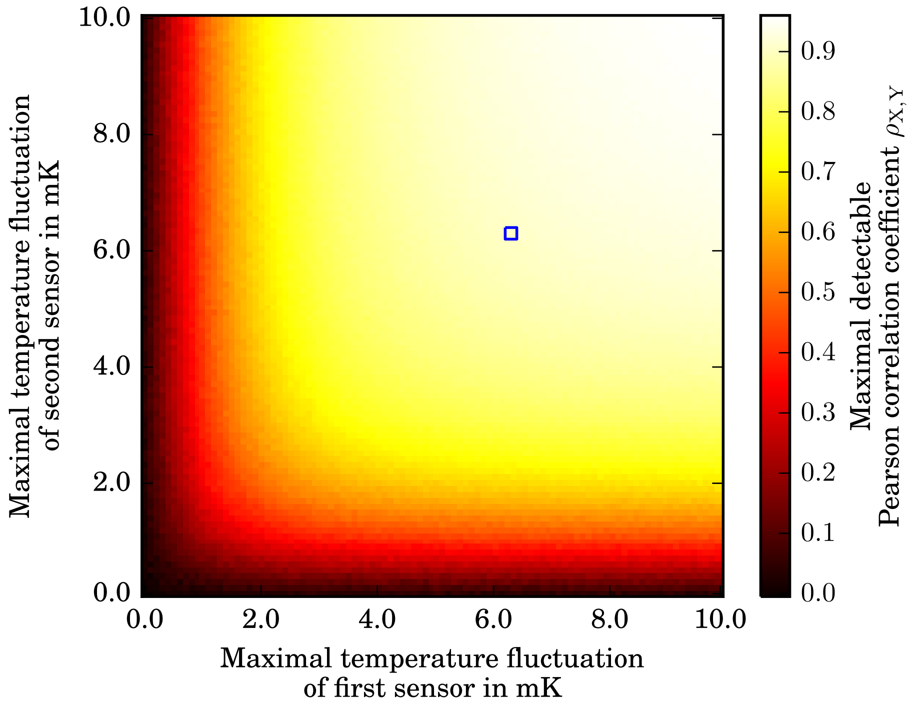

Figure 4.12.: Limit on detectable correlation coefficient. Shown is the average maximal detectable correlation coefficient for two perfectly linear correlated temperatures measured with an uncertainty on each temperature of 0.6 mK as a function of the maximal temperature difference covered by fluctuations. The blue square shows the maximum detectable correlation coefficient of 0.91 for the sensors **RTP-3-5102** and **RTP-3-5123** during the 1 h time period investigated in subsection 4.2.2 over the range of their temperature flutcuations of around 6 mK.

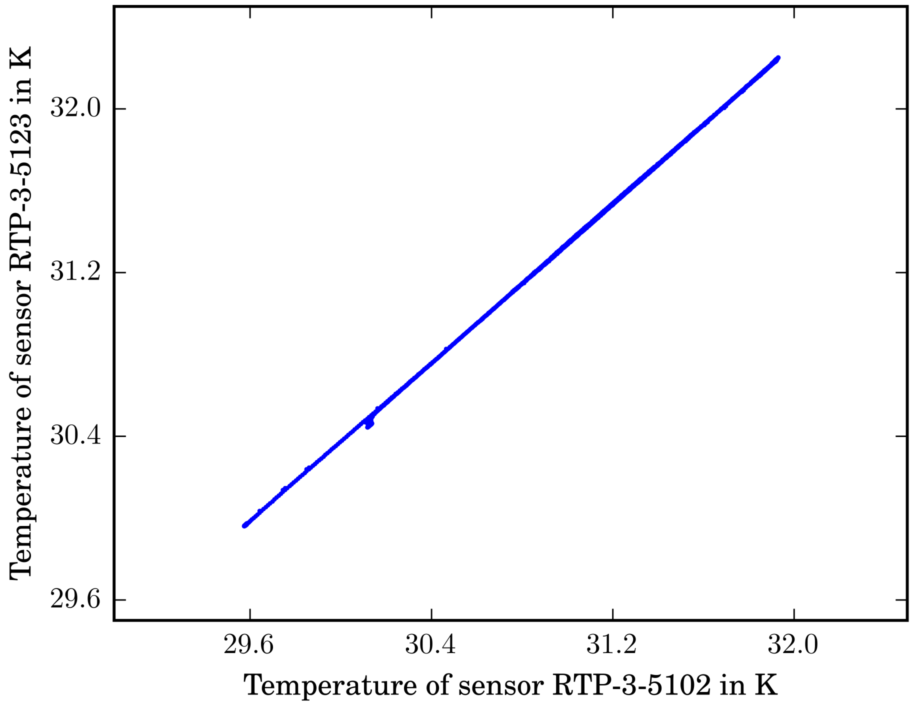

Figure 4.13.: Temperature correlation scatter plot. Shown is the correlation of measured temperatures between sensors **RTP-3-5102** and **RTP-3-5123**. The shown data was taken from Nov 24 and Nov 25 2016 for a total measurement time of 48 h equating to 5760 data points. Due to the high correlation of $\rho_\mathrm{r} = 0.9999$ and the amount data points, individual data points overlap in this graph.

the probability of this result being due to statistical fluctuations and not correlation, smaller than $1 \cdot 10^{-324}$. A visualization of all correlation coefficients between the beam tube temperature sensors can be found in figure 4.14.

As the lowest coefficient calculated in figure 4.14 is at $\rho_\mathrm{r,min} = 0.9996$, it can be concluded that the temperature along the beam tube is almost perfectly linearly correlated. This indicates that the thermal coupling between the sensors and the beam tube is very similar for all sensors. Differences in thermal coupling between sensor and beam tube would make themselves apparent as increasingly elliptic point clouds for data taken during a cyclic change in the temperature. Furthermore, horizontal or vertical distributions of the points will result from stopping a temperature change at one temperature.

Correlation between beam tube and two-phase heaters

As the heaters are used to regulate the temperature they are a candidate for causing fluctuations in the beam tube temperature and are therefore of special interest in the analysis. The correlation between the regulation of the heater power and the beam tube temperature can only be investigated during stationary operation as a change of the temperature on the scale of 100 mK already causes the heater regulation to utilize the maximal power of 2 W or turn off entirely.

As one can see in figure 4.15, the beam tube temperature and the heater power are linearly anti-correlated with a correlation coefficient of $\rho_\mathrm{r} = -0.66$. This anti-correlation is due to the fact that the regulation tries to compensate a decrease of the temperature by increasing the heater power.

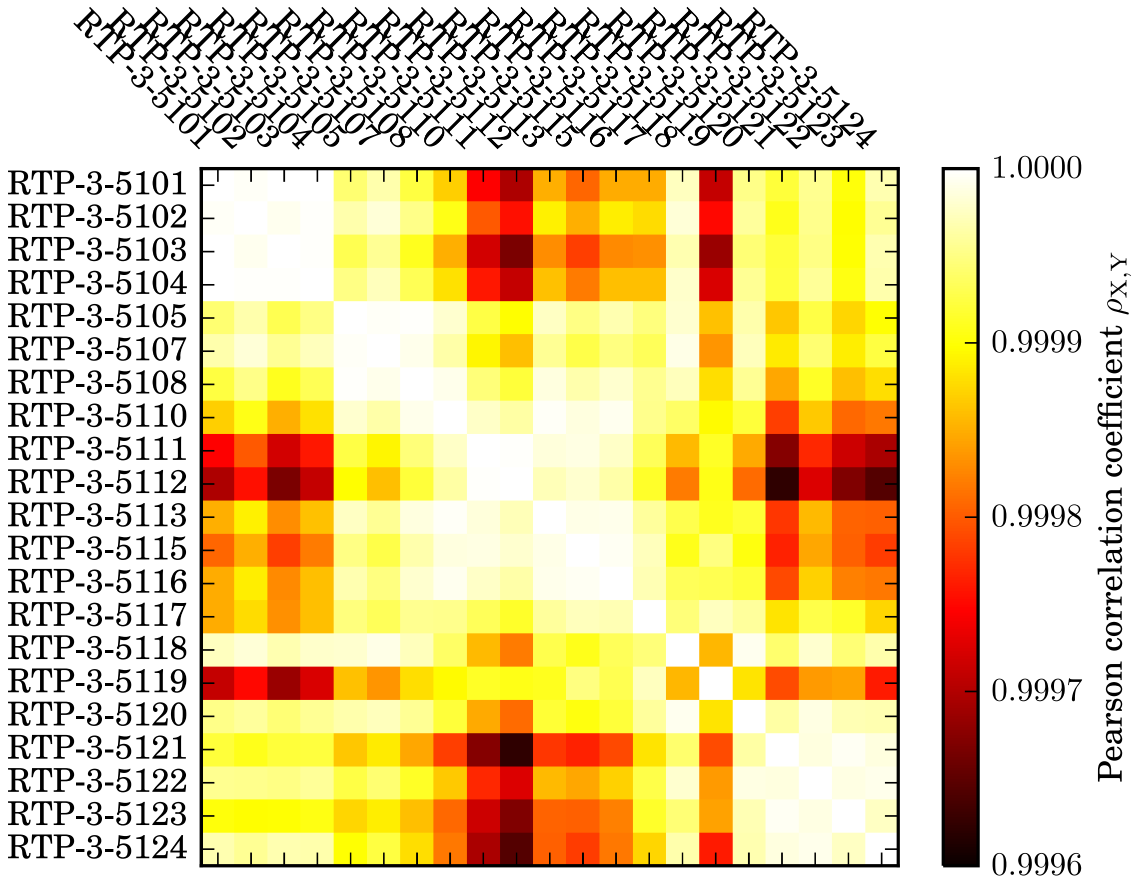

Figure 4.14.: Pearson correlation coefficient matrix. Shown are the Pearson correlation coefficients between all sensors along the beam tube. Three malfunctioning sensors have been excluded from the analysis (**RTP-3-5106**, **RTP-3-5109**, **RTP-3-5114**). The shown data was taken from the same time interval as used in figure 4.13.

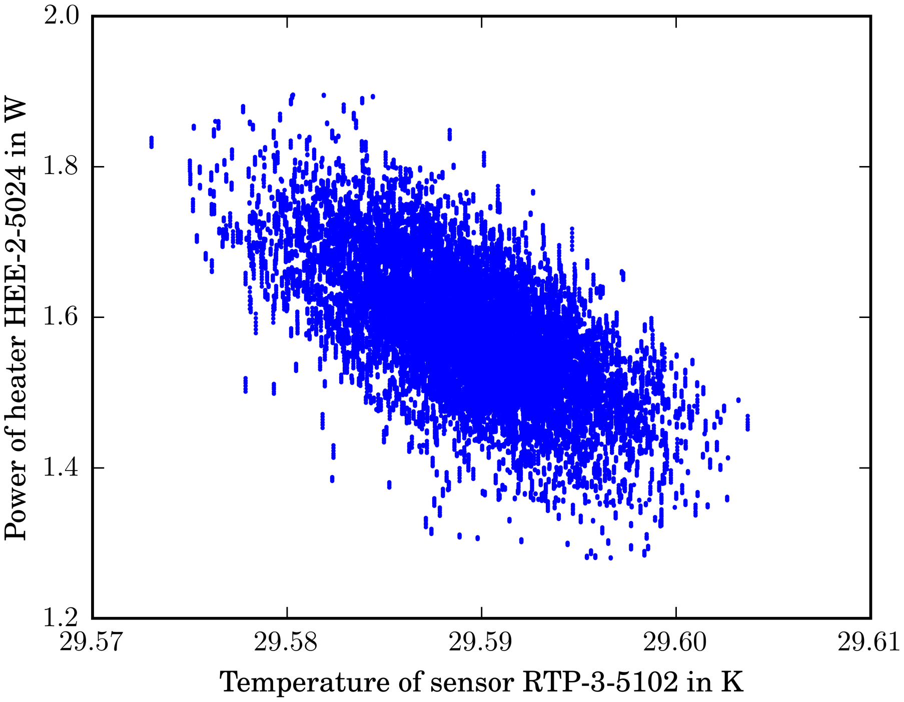

Figure 4.15.: Temperature correlation scatter plot. Shown is the correlation of the temperature measured with sensor **RTP-3-5102** and the heater power of heater **HEE-2-5024**. The shown data was taken from the time interval from Nov 4 2016 to Nov 7 2016, equating to a total number of 8640 data points.

As the changes in temperature are small during stationary operation, the above mentioned problem of the impact of readout noise on the correlation needs to be considered. In addition, a delay between temperature changes in the two-phase tubes where the heaters are situated, and the Pt500 sensor mounts should lead to a non-linearity of the system which cannot be quantified with the Pearson correlation coefficient (see figure 4.11, third row, second to last column). Therefore a frequency analysis of the temperature and heater power signals is presented in the following.

To cover the more complex, periodical correlations a Fourier analysis of signals is done by computing a discrete Fourier transform of the data points. For the discrete Fourier transform the NumPy implementation of Fast Fourier Transform for real input values `numpy.fft.rfft` [Jon01] was used. The highest physically meaningful frequency in the obtained spectrum according to the Nyquist–Shannon sampling theorem [Sha49] is 16.6 mHz corresponding to twice the measurement frequency of 1/30 Hz. Higher frequencies are artifacts due to the digital oversampling of the ADEI system.

As the frequency analysis of the signals does not suffer from the readout noise in the same fashion as the calculation of Pearson correlation coefficients, it can be used to investigate the correlation between the beam tube temperature and heater regulator even for small temperature fluctuations. This is of special interest as a confirmation of correlation for even small fluctuations as observed in subsection 4.2.2 would imply further room for improvement. Due to this, the frequency analysis has been done for the time period specified in subsection 4.2.2.

The frequency analysis of the temperature sensor **RTP-3-5102** and heater **HEE-2-5024** can be found in figure 4.16. For frequencies below 4 mHz, representing fluctuations

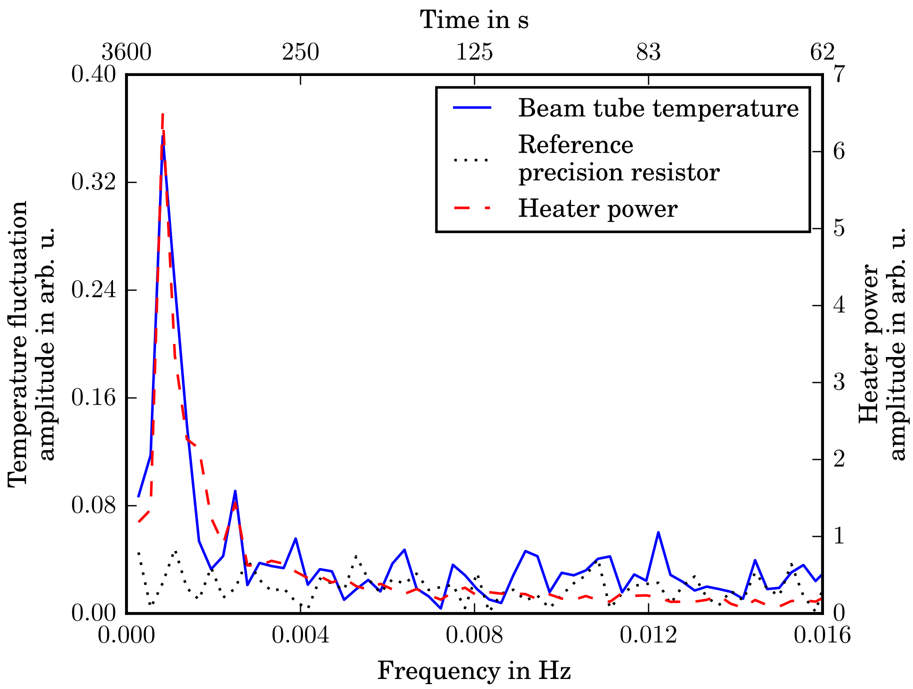

Figure 4.16.: Frequency spectrum of the beam tube temperature. Shown are the frequency spectra of the temperature data of sensor **RTP-3-5102** and the heater **HEE-2-5024** during the period of 1 h depicted in figure 4.3. The data of the 10 Ω reference precision resistor used to determine the Pt500 readout noise is plotted in green for comparison.

with periods longer than 5 min, the peak positions and relative peak intensities of both frequency spectra are in very good agreement. For high frequencies the frequency spectrum of **RTP-3-5102** is comparable to that of the precision resistor which indicates that fluctuations on small time scales are on a level below the electronic readout noise of around 0.5 mK

This strongly indicates that even for temperature fluctuations of around 1 mK/h the heater power is correlated to the beam tube temperature. It is therefore possible that the temperature stability of the WGTS beam tube can be improved towards the sub-mK level by fine-tuning the temperature regulation.

Correlation between beam tube and the remaining source cryostat

Due to the fact that the beam tube is thermally isolated from most other components of the WGTS cryostat, the largest correlation between beam tube and any other component is that between beam tube and the gHe-circuit. The cause of this correlation lies with the neon condenser of the two-phase beam tube cooling system, as it is cooled by the gHe-circuit. To investigate whether the gHe-circuit and the beam tube temperatures are correlated, temperature data from the above used time interval from Nov 4 to Nov 7 is analyzed.

In figure 4.17 three stationary phases and two transitions between them are shown. The lower average gHe-circuit temperature at a beam tube temperature of 29.6 K is due to a change in operational parameters and thus not an effect due to correlation. When looking only at the stationary phases, a slight correlation between both temperatures

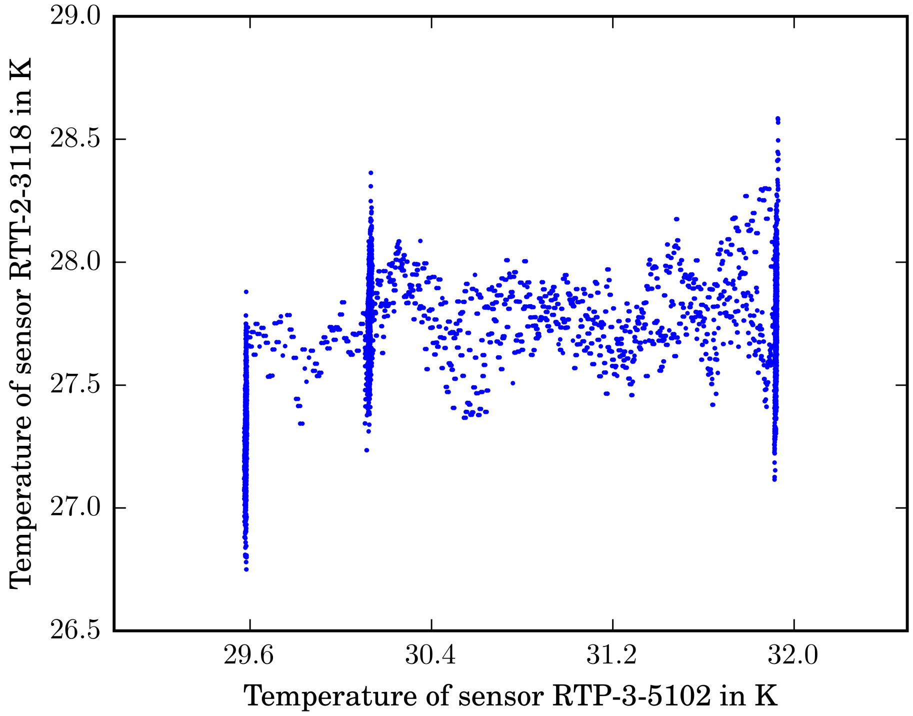

Figure 4.17.: Correlation between beam tube and gHe-circuit. Shown are the temperatures of the gHe-circuit sensor **RTT-2-3118** over the beam tube temperature measured with sensor **RTP-3-5102**. The three dense vertical point clouds are the results of measurements at one gHe-circuit temperature. Between these three clouds are data points taken during the change of the gHe-circuit temperature. The shown data was taken from Nov 24 and Nov 25 2016, the same time interval as used in figures 4.13 and 4.14.

below $\rho = 0.4$ is present. This value and the correlation between the two-phase heaters and beam tube temperature are directly related as the gHe-circuit temperature has a direct impact on the temperature and pressure inside the two-phase tubes which is the regulation parameter for the heaters. It is therefore expected that a decrease of the correlation between heater power and beam tube temperature due to fine tuning of the regulation parameters will be accompanied by a decrease of the correlation between gHe-circuit and the beam tube temperature.

Correlations with other components of the WGTS cryostat have been investigated, but no significant correlations have been found. This indicates that the beam tube is in very good approximation thermally decoupled from the rest of the source cryostat with any correlations due to thermal radiation being insignificant compared to the correlation between the beam tube temperature and the two-phase heaters and the gHe-circuit respectively. Therefore the stability of the beam tube temperature can be viewed as a quantity which only depends on the parameters of the two-phase heaters and the gHe-circuit. Hence, the impact of these parameters on the temperature stability and homogeneity is of interest for finding optimal operation parameters. It is thus discussed in detail after the following paragraph on the temperature homogeneity.

Temperature inhomogeneity towards Rear Section

In subsection 4.3.2 an inhomogeneity of the beam tube temperature is reported, which violates the KATRIN requirements as stated in the design reports. This inhomogeneity is stable on the order of the average stability over long time periods as can be seen in figure 4.7 and figure 4.8. Possible causes and the impact of this inhomogeneity are therefore addressed in the following.

Comparison with Demonstrator

The present temperature inhomogeneity of the beam tube has already been observed during the WGTS prototype experiment Demonstrator [Gro13] with values of $\Delta T_{\mathrm{max},1} = \leq 850\,\mathrm{mK}$ for the temperature gradient between center and front side and $\Delta T_{\mathrm{max},2} = \leq 300\,\mathrm{mK}$ between center and rear side. The higher inhomogeneity towards the front side during Demonstrator measurements was suspected to be the result of the vapor pressure capillaries carrying a heat load towards the beam tube. Due to this it was decided to turn the beam tube around, switching front and read side between the Demonstrator and the final configuration. Furthermore, the vapor pressure capillaries were thermally contacted to the outer shield (see subsection 2.4.1) in order to minimize any heat load into the cryostat. Due to this configuration change $\Delta T_{\mathrm{max},1}$ needs to be be compared to $\Delta T_{\mathrm{max,rear}}$ and $\Delta T_{\mathrm{max},2}$ to $\Delta T_{\mathrm{max,front}}$ from subsection 4.3.2.

With this in mind, the final configuration has achieved an inhomogeneity between center and front around 3 times better than the Demonstrator while the inhomogeneity between center and rear side has been improved by a factor of around 1.5. The fact that the larger inhomogeneity has switched sides accordingly with turning around the beam tube is a strong argument for the fact that the observed temperature inhomogeneity is the result of a heat load being induced through the vapor pressure capillaries.

Impact on KATRIN

Despite the improvement in comparison to the Demonstrator values, the homogeneity of the beam tube temperature is still significantly outside of the KATRIN requirements of $\pm 30\,\mathrm{mK}$ as stated in the Design Report [Ang05]. However, this inhomogeneity can be included in the modelling of the gas density inside the WGTS, thereby minimizing the systematic uncertainty on the neutrino mass measurement caused by it [Kuc16].

Additionally, the temperature inhomogeneity is most pregnant in the section of the beam tube closest to the rear side. As shown in figure 4.18, the gas density inside the WGTS quickly falls off towards the pump ports. Therefore, only a small percentage of the tritium is in contact with the warmer parts of the beam tube before decaying. Furthermore, the electrons produced by tritium β-decay in the rearward section of the beam tube need to pass the entire tritium gas column before exiting the WGTS towards the spectrometer. During their way through the WGTS, these electrons have a longer path to cover on which they can scatter with gas molecules, thereby losing more energy on average than electrons emitted in the front section of the WGTS. This diminishes the overall effect of electrons emitted in the rearward section of the WGTS on the neurino mass when compared to those emitted in the front section.

To summarize, the influence of the beam tube temperature inhomogeneity can be included into the WGTS gas models to dimish its impact on the neutrino mass, and the location of the inhomogeneity affects only electrons who contribute comparatively

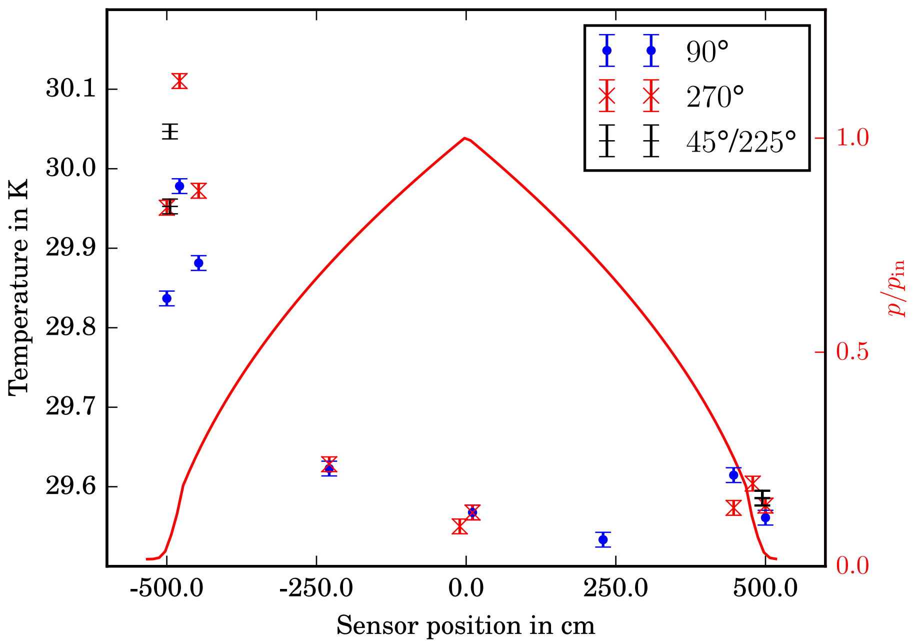

Figure 4.18.: The temperature inhomogeneity of the beam tube and the gas density profile of the WGTS. Shown is the content of figure 4.6 together with the normalized gas density profile inside the WGTS. The gas density falls off sharply towards the pump ports, causing only a small portion of the tritium molecules to be affected by the temperature inhomogeneity.

little to the neurino mass measurement. Therefore, the observed inhomogeneity poses no insurmountable problem for the neutrino mass measurement with KATRIN.

Regardless, it is favorable for the temperature inhomogeneity to be as small as possible to minimize its effect as best as possible. Therefore, an investigation of the influence of the operational parameters on the temperature inhomogeneity as observed in subsection 4.3.2 is presented in the following paragraph.

Impact of operational parameters on the temperature stability and homogeneity

The dependence of the temperature inhomogeneity on the operational parameters observed in subsection 4.3.2 indicated that an optimization of the operational parameters can improve the temperature homogeneity. Therefore an investigation of the dependence of both temperature stability and homogeneity on the temperature of the gHe-circuit and the absolute beam tube temperature is done in the following.

This investigation was done by changing heater power and gHe-circuit temperature to different settings and calculating the corresponding stability and homogeneity. Time constraints allowed only for 5 different parameter combinations to be tested, but a trend is already visible in these few data points. In figure 4.19, the dependence of the temperature homogeneity is shown. While no significant change is visible for the inhomogeneity between center and front, the inhomogeneity between center and rear decreases by about 116 mK by increasing the beam tube temperature from 29.56 K to 31.15 K. It further improves by another 15 mK when going to 32.00 K, for a total of 141 mK improvement compared with 29.56 K. This change in temperature homogeneity

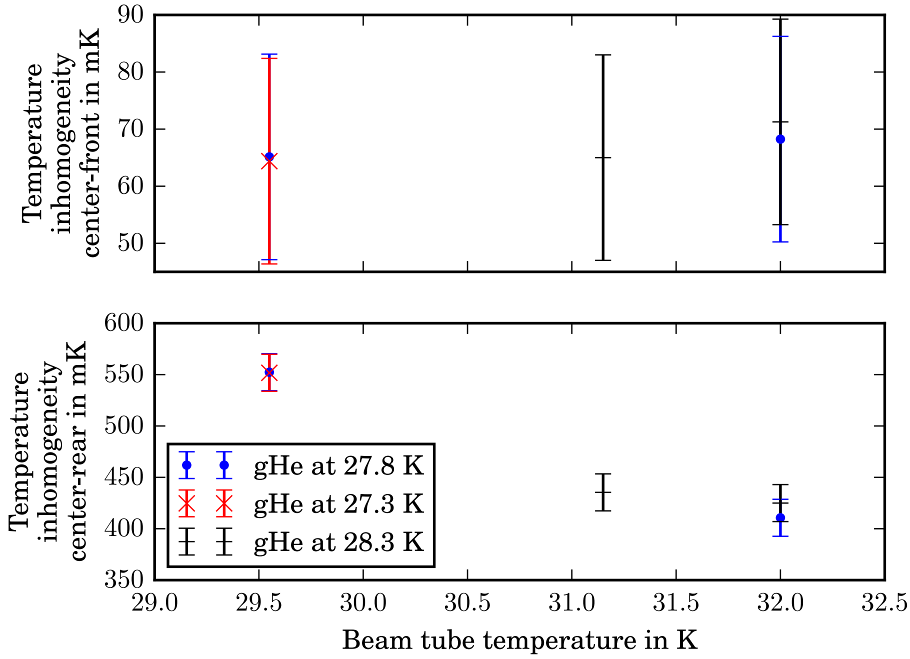

Figure 4.19.: Dependence of temperature homogeneity on operational parameters. The shown temperature inhomogeneites are the maximal temperature differences between the center of the beam tube and either side. The temperature of the gHe-circuit was measured with sensor **RTT-2-3118**. As can be seen, the inhomogeneity between center and front side of the beam tube does not significantly depend on the beam tube temperature, while the inhomogeneity between center and read side decreases significantly towards higher beam tube temperatures.

appears to be dominated by the absolute beam tube temperature while the influence of changing the gHe temperature only causes a slight variation in the temperature homogeneity.

The temperature stability, however, as can be seen in figure 4.20, shows a trend towards better stability at higher gHe temperatures while the absolute beam tube temperature does not appear to be influencing the stability significantly. In the investigated intervals the stability of the gHe-circuit was at 156 mK/h for 27.3 K whereas at 28.3 K the stability was at 97 mK/h.

This behavior can be explained by the nature of the fluctuations of the gHe-circuit (see subsection 2.4.1). The gHe used for cooling the two-phase neon condensers is produced by mixing two streams of gHe at around 6 K and 60 K. The mixing process causes temperature fluctuations whose intensity is the greatest for a mixture of equal parts colder and warmer gHe. Moving away from this point of equality towards warmer or colder temperatures of the gHe-circuit therefore improves the stability of the gHe-circuit which in turn improves the beam tube stability.

The conclusion of this preliminary investigation of the dependences of temperature stability and homogeneity of the beam tube is that a higher absolute beam tube temperature and a higher gHe temperature are favorable for better homogeneity and stability. One disadvantage to this change in operational parameters would be the need for an increased throughput of tritium through the WGTS. However, this choice would have the additional advantage of decreasing the possibility for tritium clusters to form

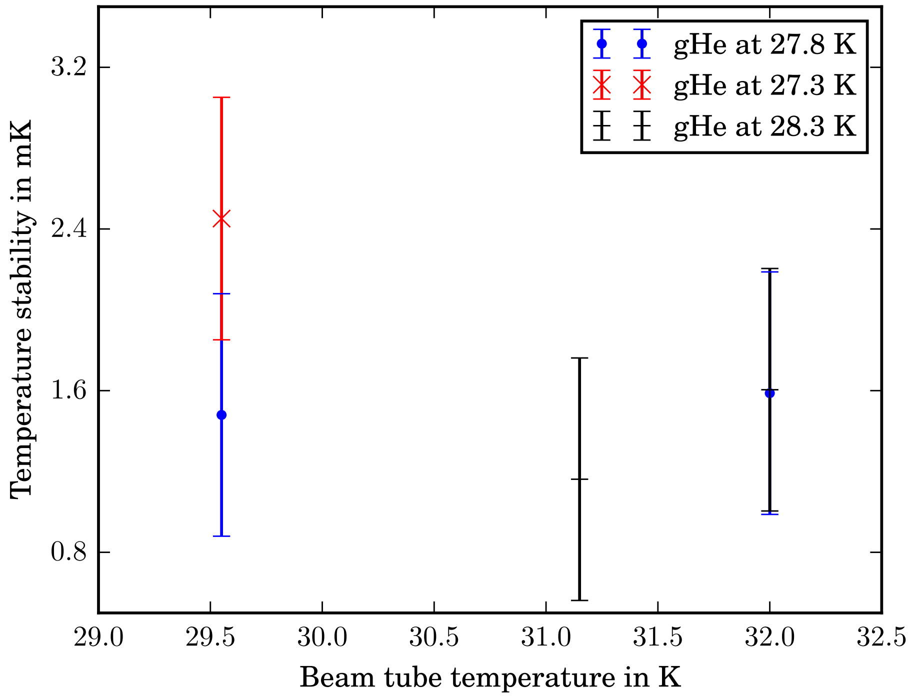

Figure 4.20.: Dependence of temperature stability on operational parameters. Shown is the temperature stability of 1 h of temperature data at the respective operational parameters. The beam tube temperature does not appear to have a significant influence on the temperature stability. On the other hand, raising the gHe-circuit temperature from 27.3 K to 27.8 K or 28.3 K appears to have a positive influence.

(see subsection 2.3.2) and thereby reduce the related systematic effect introduced by them. By quantifying the contibution of each of these effects in detail, the presented excellent temperature stability and usable homogeneity could be further improved by optimization of the WGTS operation parameters. As this optimization would only require a change in parameters for a significant potential improvement, additional measurements and a more thorough investigation of this topic are recommended.

Approaching the limit of the current measurement system

In the previous paragraphs the possibility for further improvements of the temperature stability have been discussed. As the already observed stability is on the order of 1 mK for optimal conditions, further improvements mean that the capability for sub-mK temperature measurement is necessary to reliably quantify the temperature stability. This poses a problem as currently the uncertainty due to the electronic readout of the Pt500 sensors already contributes an uncertainty of around 0.5 mK (see table 3.2). Therefore, measuring a better beam tube stability than what has already been achieved necessitates changes in the configuration of the temperature measurement system.

One possibility is to increase the measuring current. This results in a higher voltage drop over the Pt500 sensors, leading to a better signal to noise ratio of the digital multimeter. An increase of the current from 500 µA to 2 mA should reduce the noise by a factor of four which would mean a precision of around 0.1 mK. A problem with this approach is the unquantified self-heating of the Pt500 sensors which increases quadratically with the measuring current [Ber69]. Therefore, this change in configuration necessitates simulations to estimate at which current the self-heating leads to unacceptable systematic uncertainties.

Another approach is to exchange the used equipment with higher performance equipment. A possible choice would be a combination of the `Model 2182/2182A Nanovoltmeter` [Kei03] with the `Model 7001 Switch System` [Kei01], both made by `Keithley`. This combination should be capable of reaching a precision on the order of 0.01 mK.

Looking at both approaches for improving the relative temperature measurement, the first one is strongly favored. It does not necessitate any changes to the hardware and software and only needs its viability to be verified via simulations. The second approach, on the other hand, would make significant changes to both hardware and software necessary in order to realize the full measuring potential, as the uncertainty contributions due to linear interpolation and the Pt500 characteristic curves (see subsection 3.3.5) become dominant. The hardware components on their own would already cost a high four digit number in euros without even considering installation and changes to the TES software.

As a conclusion, a possible improvement of the precision of the relative temperature measurement should be done by increasing the measuring current. If even better precision is needed a change of hardware becomes necessary.

4.5. Conclusion and implications for KATRIN

Measurements of the KATRIN WGTS beam tube temperature stability and homogeneity have been done with the sensor system described in chapter 3.

The requirement of $\pm 30\,\mathrm{mK/h}$ on the temperature stability as specified in the KATRIN design report has been fulfilled and surpassed by more than one order of magnitude. This holds true even for longer measurement periods than the specified 1 h intervals. For the longest investigated interval duration of 108 h, a worst case estimation of the temperature stability is still better than the KATRIN requirement of $\pm 30\,\mathrm{mK}$ by 5 mK. Therefore, provided a stable operation of the system, the WGTS should be capable of continuous measurement during one entire measurement run of 60 d when solely looking at the temperature stability. Remaining fluctuations of the beam tube temperature have been investigated and found to be a result of the interaction between beam tube, gHe-circuit and two-phase heaters, which makes further improvement of the temperature stability by optimization of the heater regulation an interesting prospect.

As already observed in the former Demonstrator measurements [Gro13], a temperature inhomogeneity along the beam tube, violating the specified requirement of $\pm 30\,\mathrm{mK}$, has been observed. However, in comparison to the Demonstrator the inhomogeneity has been reduced by up to a factor of 1.5. It has been shown that the temperature inhomogeneity is stable over long time scales and thus only causes static inhomogeneities of the tritium gas density profile which can be accounted for during analysis. Therefore the temperature inhomogeneity does not have a negative impact on the neutrino mass measurement with KATRIN.

To further improve the achieved results, the influence of operational parameters of the WGTS cryostat on the temperature stability and homogeneity has been investigated. The derived results indicate that higher temperatures of the beam tube ($>30\,\mathrm{K}$) and the gHe-circuit are favorable for both stability and homogeneity and are therefore recommended for further operation of the WGTS cryostat.

While the achieved results have shown capabilities beyond the specifications, surpassing the requirements does not necessarily lead to an immediate improvement of the neutrino mass shift due to systematic effects of the WGTS gas column density, as the temperature is only one of its deciding parameters. Detailed analyses of the stability of the gas composition as well as inlet and outlet pressure have to be done when the WGTS is commissioned with gas. It is expected that the achieved results translate also in a lower uncertainty linked to the final states distribution, but since new theoretical calculations are ongoing at the moment the associated theoretical uncertainty is unknown. Therefore, the magnitude of this effect cannot be quantified yet. The observed tendency of better temperature stability of the beam tube at higher temperatures is an issue when looking at the uncertainty caused by the Doppler effect as well as the increased throughput of tritium trhough the WGTS. On the other hand, this tendency is promising as the formation of tritium clusters, and therefore the systematic uncertainty they cause, decreases with rising temperature. A conclusive recommendation for the operating temperature on the basis of these effects cannot be given currently, as the effect due to tritium cluster formation is not quantified. However, as the Doppler effect is well understood in comparison to the tritium cluster formation and can be modeled accurately, a preliminary recommendation favors higher operating temperatures of the beam tube.

5. Summary and outlook

The existence of a non-vanishing neutrino mass has been discovered by a multitude of neutrino oscillation experiments. Since this mass is an indicator for physics beyond the standard model as well as an important factor during the structure formation in the early stages of our universe, a multitude of experiments have tried to directly measure the neutrino mass. The best upper limit for the neutrino mass of $2\,\mathrm{eV}/c^2$ 95 % C. L has been found by the Mainz and Troitsk experiments. Succeeding both these experiments, the KATRIN experiment aims to improve the sensitivity on the neutrino mass by one order of magnitude, allowing for a $5\,\sigma$ discovery potential of $350\,\mathrm{meV}/c^2$ and an upper limit of $200\,\mathrm{meV}/c^2$ 90 % C. L in case of no detected neutrino mass.

To reach this target sensitivity, the experiment needs to increase the statistics while keeping all systematic uncertainties down to an unprecedented level. One big component of these systematic uncertainties results from the Windowless Gaseous Tritium Source providing the 10^{11} β-electrons per second for KATRIN, whose activity needs to be stable to 0.1 %. This activity depends on several factors such as the purity of tritium gas fed into the WGTS beam tube, the pressure the tritium gas is injected and pumped out at, as well as the temperature of the beam tube.

The focus of this thesis was placed on the systematic uncertainties with regards to the temperature. With the final commissioning of the two-phase beam tube cooling system and the beam tube temperature measurement system as a necessity, the main objectives of this thesis were the conception of a calibration procedure for the Pt500 temperature measurement system including the calculation of all related calibration uncertainties, as well as the measurement of the beam tube temperature with this system under realistic conditions for nominal KATRIN operation.

Despite the prior operation of the temperature measurement system with the prototype experiment Demonstrator, improvements such as dedicated precision resistors for determination of the electronic readout noise have been implemented during the final commissioning of the temperature measurement system. With these improvements and the devised calibration procedure, it has been shown that the required accuracy of 10 mK for measurements of the temperature homogeneity and stability of the WGTS beam tube can be achieved repeatably and independently of static external influences such as the magnetic field inside the WGTS cryostat. First inquiries into the long-term stability of the calibration constants gained with this procedure have been made. Promising results indicating no need for recalibration during a KATRIN measurement run of 60 d have been found, however, longer measurement times are necessary to confirm this.

With these results, the temperature stability and homogeneity of the WGTS beam tube could be measured under realistic conditions during the measurement campaign

Aug 2016-Dec 2016. The temperature stability of the WGTS beam tube has been found to exceed the requirement of 30 mK/h by almost one order of magnitude. By analyzing 1 h intervals contained in a measurement duration of 16 d during comparatively stable operation, an average stability of (3.28 ± 1.68) mK/h has been derived (error here given by standard deviation of the 1 h interval values). For time periods with better than average stability, temperature stabilities of up to (0.80 ± 0.59) mK/h could be found. These values approach the detection limit of the temperature measurement system in its current configuration. Furthermore, it could be shown that the temperature stability requirement of ± 30 mK could be met over time periods far exceeding the specified 1 h interval, with a worst case estimation of the stability 5 mK below the requirement for an interval duration of 108 h. The causes for remaining fluctuations of the beam tube temperature have been investigated and could be identified to be due to a remaining correlation with the temperature regulation of the the two-phase cooling system. Therefore, it can be expected that an optimization of the regulation will result in an even better temperature stability.

These values are very promising with regards to opening up some of the planned uncertainty budget for the source activity, which can instead be used by other components of KATRIN or even increase KATRIN sensitivity. The high stability is especially important in the context of the search for sterile neutrinos with the KATRIN experiment as the resulting requirements on the temperature stability are much stricter [Mer17].

In contrast to the temperature stability, the temperature homogeneity has been found to be outside of the specified requirement of ± 30 mK from the center of the WGTS beam tube towards both sides, reaching an inhomogeneity of around 500 mK towards the rear side. This issue has been known from the Demonstrator and has been suspected to be the result of a heat load onto the beam tube via the capillaries of the vapor pressure sensors which are part of the temperature measurement system. Compared to the Demonstrator, the inhomogeneity could be reduced by approximately a factor of 1.5, which is suspected to be the result of thermally contacting the capillaries to the liquid nitrogen shield of the WGTS cryostat. Despite being outside the original specifications, this inhomogeneity can be accounted for in the analysis of the source activity, as the inhomogeneity is stable in time and the individual temperatures are known very accurately [Kuc16]. The inhomogeneity therefore does not have a negative impact on the KATRIN sensitivity on the neutrino mass.

In addition to the above measurements, the dependence of both temperature stability and homogeneity of the WGTS beam tube on the operational parameters of the WGTS cryostat has been investigated. Due to time constraints, only a limited number of measurement parameter combinations could be tested. Therefore, currently only the observation of a trend can be stated. This trend indicates the favorability of a higher operation temperature of both the beam tube and the gHe-circuit. To gather more data with regard to this topic as well as realistic data for the temperature stability and homogeneity over a KATRIN measurement run duration of 60 d at stable conditions, further measurements are necessary.

These measurements, as well as further investigations such as the magnetic field dependence of the Pt500 sensors, can be done in the ongoing single component commissioning phase of KATRIN until summer 2017. This phase will be followed by spectra mesurements of $^{83\mathrm{m}}$Kr, for which the beam tube needs to be at 100 K, necessitating the use of argon instead of neon for the two-phase cooling system, an operation mode that has not been tested yet. Following the krypton measurement, the interplay between the source parameters of injection pressure, gas composition, and beam tube temperature under realistic conditions can be studied in detail during the inactive (without tritium) commissioning of KATRIN and the accompanying measurement phase in fall 2017. With these measurements, an estimation of the stability of the column density can be derived, which will then need to be verified during the active commissioning of KATRIN with tritium in 2018.

Concluding, it has been shown that the WGTS two-phase beam tube cooling system is capable of fulfilling the temperature stability requirement and that the temperature measurement system is capable of verifying this achievement. And while a temperature inhomogeneity has been found, it can be accounted for in analysis, meaning that with regard to the beam tube temperature, the KATRIN experiment is ready for neutrino mass measurement as specified.

A. Detailed calibration procedure

In this section, the calibration procedure outlined in section 3.2 is described in detail with all technical steps that need to be taken. The necessary substeps can be summed into the following 6 steps.

1. Preparation of the vapor pressure system,
2. Filling of the bulb and thermalization,
3. Calibration,
4. Emptying of the bulb,
5. Refilling the bulb,
6. Returning the vapor pressure system to its initial state.

Steps 1 needs to be done once before all calibrations and Step 6 needs to be done after all calibrations have been performed.

In the following description, the procedure is formulated for generalized component numbers with the following placeholders:

- **N** - the number of the valve block,
- **XX** - a number corresponding to the used bulb,
- **YY** - Pt500 sensor number, for a mapping to Pt500 sensors see table A.1,
- **M** - component number of WGTS cryostat part the bulb is attached to. **M** = 5 for all bulbs on beam tube. For bulbs on the front/rear pump ports **M** = 4/6.

Valve block 1 is not in use as it was intended for bulbs attached to the DPS1-F/R-1 sections of the beam tube, which are not included in the final WGTS cryostat configuration. Valve block 5 is only connected to the four pump port bulbs.

General prerequesite: A purged vapor pressure system with all valves closed and all flowmeters set to 0 mg/s is assumed.

Preparation of the vapor pressure system

Prerequesite: Pressure above 20 bar in neon gas cylinder. No significant amount of neon is used during the calibration procedure.

To prepare the vapor pressure system for calibration, the following steps have to be taken:

1. Open valve of neon gas cylinder in gas cylinder cabinet **200-PID-0-3301**.
2. Set neon pressure regulator in gas cylinder cabinet to around 5 bar.
3. Open hand-valve **VMO-30005**.
4. Set pressure regulator **VMO-30006** to around 5 bar.
5. Set pressure regulator **VMO-30007** to around 5 bar.
6. Open hand valves of pressure regulators **VMO-30006** and **VMO-30007**.
7. Open magnetic valves **VMO-30001** and **VMO-30008**.
8. Start vacuum pump **PDF-30003**.
9. Open hand valve **VMO-30063**.

By following this steps the vapor pressure system is now in the base state for Pt500 calibration.

Filling of the bulb and thermalization

Prerequesite: Saturation vapor pressure corresponding to set beam tube temperature calculated.

1. Purging the bulb to remove possible contaminations:
   1.1. Open magnetic valve **VMO-300N8** to vacuum line.
   1.2. Open magnetic valve **VMO-3M0XX0001**.
   1.3. Open magnetic valve **VMO-3M0XX0002**.
   1.4. Wait until pressure on pressure transducer **RPM-3-01N0** has fallen to 1 mbar.
   1.5. Close magnetic valve **VMO-3M0XX0002**.
   1.6. Close magnetic valve **VMO-300N8** to vacuum line.
2. Filling the bulb:
   2.1. Select **RTP-3-M0YY** in TES software to view its temperature by clicking the yellow bulb button (see figure A.1).
   2.2. Open magnetic valve **VMO-3M0XX0004**.
   2.3. Open magnetic valve **VAO-300N4**.
   2.4. Set mass flowmeter **RFC-300N3** to 10 mg/s.
   2.5. Fill bulb until pressure on pressure transducer **RPM-3-01N2** has reached 100 mbar less than the calculated saturation vapor pressure for the beam tube temperature.
   2.6. Set mass flowmeter **RFC-300N3** to 2 mg/s.
   2.7. Fill bulb until temperature of **RTP-3-M0YY** jumps more than 20 mK between two measurement cycles of the digital multimeter.

2.8. Reset counter of flowmeter **RFC-300N3** to 0 mg.

2.9. Fill bulb with 250 mg as counted by the flowmeter **RFC-300N3**.

2.10. Set mass flowmeter **RFC-300N3** to 0 mg/s.

2.11. Close magnetic valve **VAO-300N4**.

3. Thermalization:

   3.1. Wait until temperature of **RTP-3-M0YY** and pressure of **RPM-3-01N2** do not change significantly anymore (ca. 25 min).

Calibration

Prerequesite: Bulb corresponding to Pt500 needs to be filled with neon and is thermalized as described in the previous step.

1. Click on the tool symbol below the bulb to calibrate (see figure A.1). A dialog window as shown in figure A.2 will open.
2. Ensure the vapor pressure radio button is set to **RPM-3-01N2**.
3. Wait until the digital multimeter has just finished one measurement cycle.
4. Click on the *Aktualisieren* button.
5. Close the dialog window.

Emptying of the bulb

Prerequesite: Saturation vapor pressure corresponding to measured beam tube temperature calculated/ saturation vapor pressure value of calibration noted.

Steps 2 and 3 are meant to protect the vacuum pump from overpressure above 1.2 bar. Experience has shown that these steps can be skipped as the small diameter and long length of the capillaries reduce the pressure the vacuum pump has to pump against to a manageble level. This has not been tested for pressures above $\sim$3.5 bar, so these two steps should be considered when calibrating at higher temperatures. Steps 5 and 6 empty the bulb of liquid neon.

1. Close magnetic valve **VMO-3M0XX0004**.
2. 2.1. Open magnetic valve **VMO-300N8** to vacuum line.

   2.2. Pump down vacuum line in valve block until pressure on pressure transducer **RPM-3-01N0** has fallen to 1 mbar.

   2.3. Close magnetic valve **VMO-300N8** to vacuum line.

   2.4. Open magnetic valve **VMO-3M0XX0002**.

   2.5. Close magnetic valve **VMO-3M0XX0002**.
3. Repeat above step until pressure on pressure transducer **RPM-3-01N0** does not rise above 1.2 bar upon opening **VMO-3M0XX0002** to guarantee that the neon in the bulb has fully evaporated.

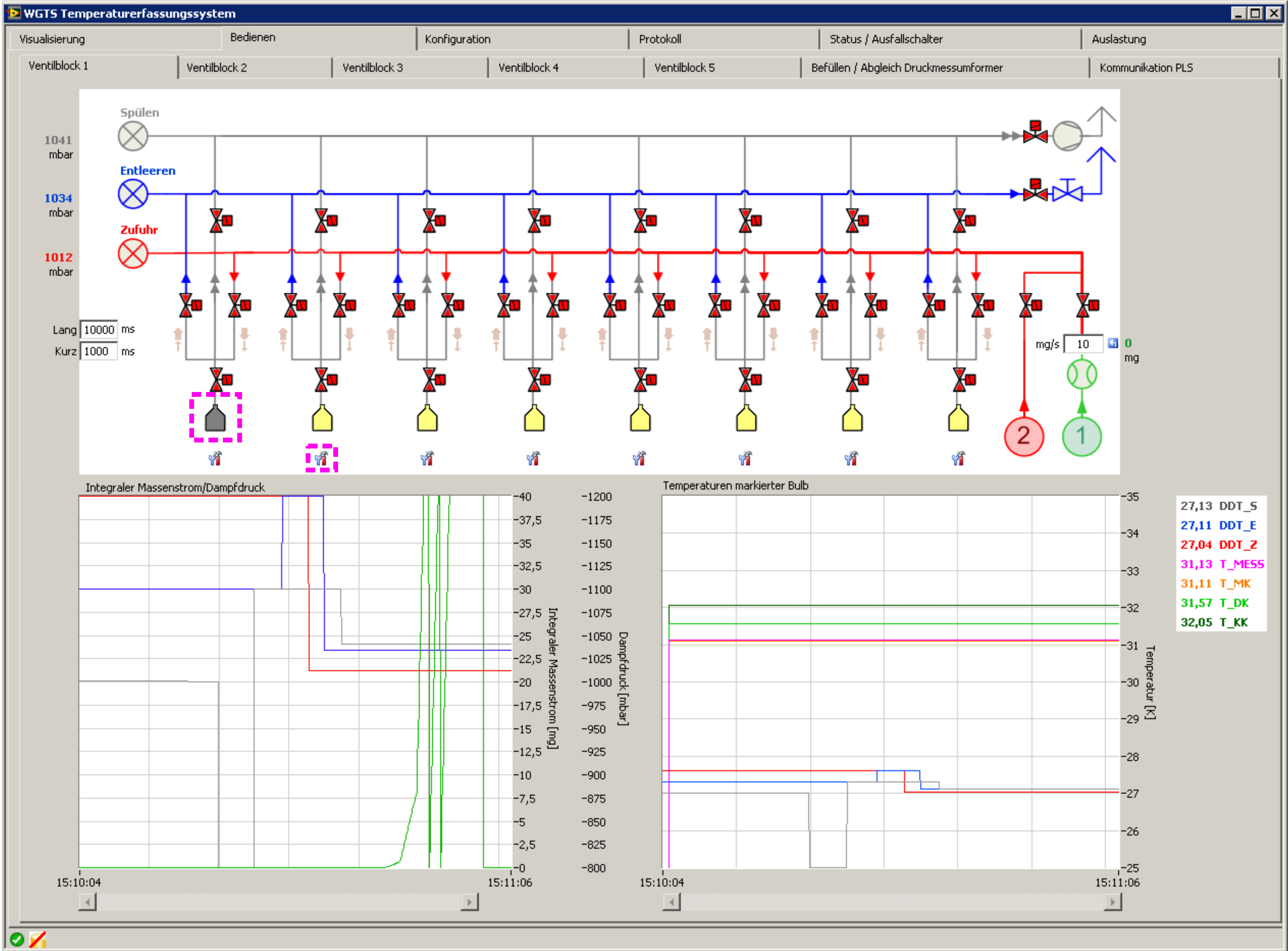

Figure A.1.: TES screenshot. The pink marked bulb is selected anf thus its symbol is grayed out. The live data of the selected sensor is shown in the lower right graph. Pressing on the small tool symbol will open the calibration dialog as can be seen in part in figure A.2.

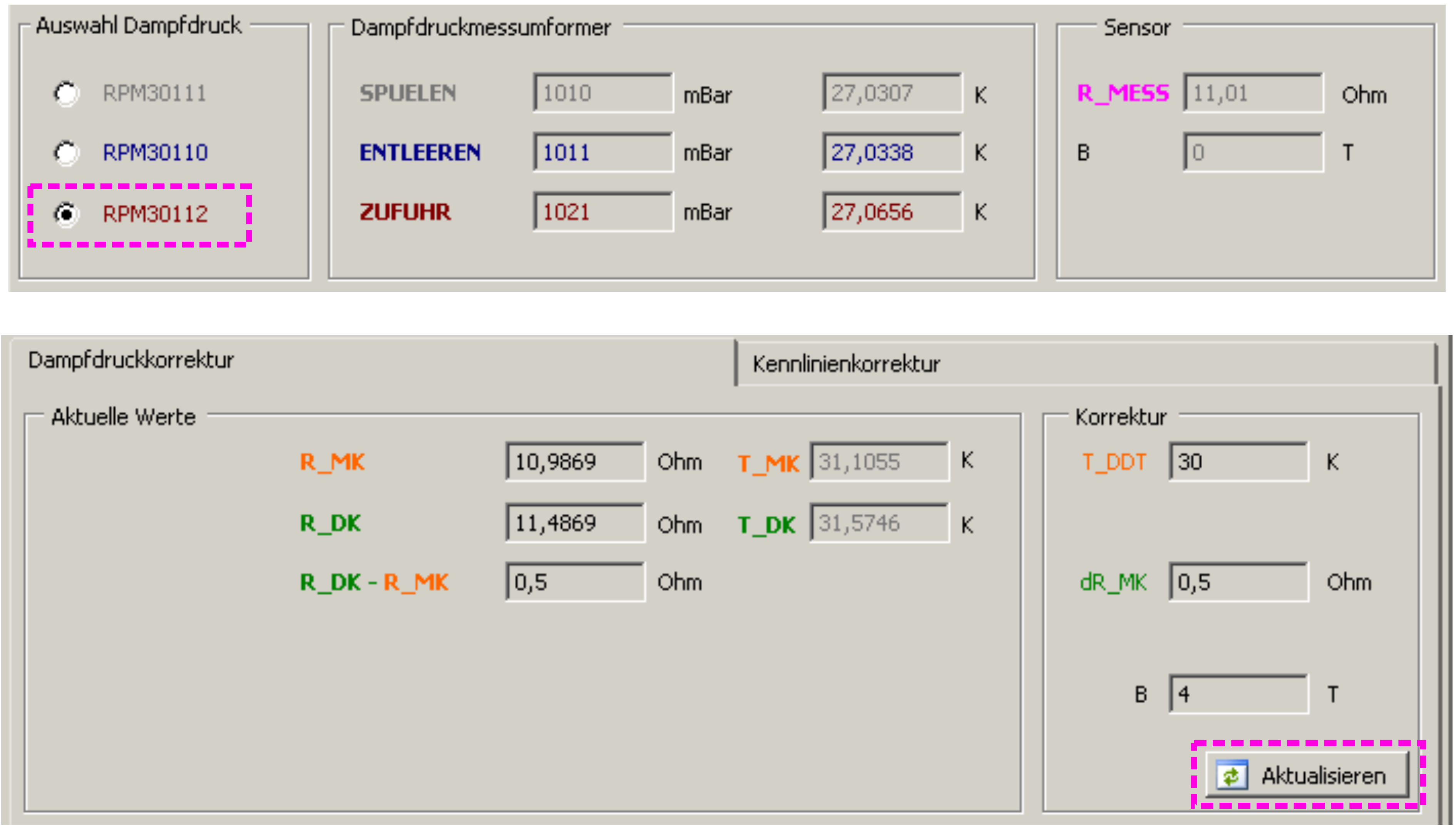

Figure A.2.: Composite screenshot of TES calibration dialog. Care needs to be taken that the correct pressure transducer currently connected to the bulb is selected before calibration. The *Aktualisieren*-button triggers the calibration and should be pushed immediately after the digital multimeter has finshed its measurement cycle.

4. Open magnetic valve **VMO-3M0XX0002**.
5. 5.1. Open magnetic valve **VMO-300N8** to vacuum line.
   5.2. Pump down valve block until pressure on pressure transducer **RPM-3-01N0** has fallen to 1 mbar.
   5.3. Close magnetic valve **VMO-300N8** to vacuum line.
6. Repeat above step until pressure on pressure transducer **RPM-3-01N0** does not rise above the saturation vapor pressure anymore after closing magnetic valve **VMO-300N8**.
7. Close magnetic valve **VMO-300N8** to vacuum line.
8. Close magnetic valve **VMO-3M0XX0002**

Refilling the bulb

Prerequesite: Saturation vapor pressure corresponding to measured beam tube temperature calculated/pressure value of calibration noted.

1. Open magnetic valve **VMO-3M0XX0004**.
2. Open magnetic valve **VAO-300N4**.
3. Set mass flowmeter **RFC-300N3** to 10 mg/s.
4. Fill bulb until pressure on pressure transducer **RPM-3-01N2** has reached around 1100 mbar, but definitely less than the saturation vapor pressure.
5. Set mass flowmeter **RFC-300N3** to 0 mg/s.
6. Close magnetic valve **VAO-300N4**.
7. Close magnetic valve **VMO-3M0XX0004**.
8. Close magnetic valve **VMO-3M0XX0001**.

Returning the vapor pressure system to its initial state

Prerequesite: All bulb valves **VMO-3M0XX0001**-**VMO-3M0XX0004** closed. All mass flowmeters **RFC-300N3** set to 0 mg/s. All magnetic valves **VAO-300N4** to fill line closed. All magnetic valves **VMO-300N8** to vacuum line closed.

1. Close hand valve **VMO-30063**.
2. Stop vacuum pump **PDF-30003**.
3. Close magnetic valves **VMO-30001** and **VMO-30008**.
4. Close hand valves of pressure regulators **VMO-30006** and **VMO-30007**.
5. Relax pressure regulator **VMO-30006**.
6. Relax pressure regulator **VMO-30007**.
7. Close hand-valve **VMO-30005**.
8. Relax neon pressure regulator in gas cylinder cabinet.
9. Close valve of neon gas cylinder in gas cylinder cabinet **200-PID-0-3301**.

Table A.1.: Mapping between bulbs and Pt500 sensors. The sensors **RTP-3-5106**, **RTP-3-5109** and **RTP-3-5114** are defect and thus not included in this table.

Pt500 sensor	Bulb	Valve to bulb
RTP-3-5101	TPB-35031	VMO350310001
RTP-3-5102	TPB-35032	VMO350320001
RTP-3-5103	TPB-35033	VMO350330001
RTP-3-5104	TPB-35034	VMO350340001
RTP-3-5105	TPB-35035	VMO350350001
RTP-3-5107	TPB-35037	VMO350370001
RTP-3-5108	TPB-35038	VMO350380001
RTP-3-5110	TPB-35040	VMO350400001
RTP-3-5111	TPB-35041	VMO350410001
RTP-3-5112	TPB-35042	VMO350420001
RTP-3-5113	TPB-35043	VMO350430001
RTP-3-5115	TPB-35045	VMO350450001
RTP-3-5116	TPB-35046	VMO350460001
RTP-3-5117	TPB-35047	VMO350470001
RTP-3-5118	TPB-35048	VMO350480001
RTP-3-5119	TPB-35049	VMO350490001
RTP-3-5120	TPB-35050	VMO350500001
RTP-3-5121	TPB-35051	VMO350510001
RTP-3-5122	TPB-35052	VMO350520001
RTP-3-5123	TPB-35053	VMO350530001
RTP-3-5124	TPB-35054	VMO350540001

B. Datasheets

In this section, excerpts from the datasheets of the components used in the TES are depicted. All excerpts are printed with permission from their resprective right holders.

Performance characteristics – ceramic process isolating diaphragm

Reference accuracy – PMC71

The reference accuracy comprises the non-linearity (terminal based), hysteresis and non-reproducibility as per IEC 60770. The data refer to the calibrated span.

Measuring cell	Gauge pressure sensor	Absolute pressure sensor
100 mbar (1.5 psi)	• TD 1:1 to TD 10:1 = ±0.075 • TD > 10:1 = ±0.0075 x TD	• TD 1:1 to TD 5:1 = ±0.075 • TD > 5:1 = ±0.015 x TD
250 mbar (4 psi)	• TD 1:1 to TD 15:1 = ±0.075 • TD > 15:1 = ±0.005 x TD	• TD 1:1 to TD 10:1 = ±0.075 • TD > 10:1 = ±0.0075 x TD
400 mbar (6 psi), 1 bar (15 psi), 2 bar (30 psi), 4 bar (60 psi), 10 bar (150 psi)	• TD 1:1 to TD 15:1 = ±0.075 • TD > 15:1 = ±0.005 x TD	• TD 1:1 to TD 15:1 = ±0.075 • TD > 15:1 = ±0.005 x TD
40 bar (600 psi)	• TD 1:1 to TD 10:1 = ±0.075 • TD > 10:1 = ±0.0075 x TD	• TD 1:1 to TD 10:1 = ±0.075 • TD > 10:1 = ±0.0075 x TD
Platinum version: 1 bar (15 psi), 2 bar (30 psi), 4 bar (60 psi), 10 bar (150 psi)	• TD 1:1 = ±0.05	• TD 1:1 = ±0.05

Total performance – PMC71

The "Total performance" specification comprises the non-linearity including hysteresis, non-reproducibility as well as the thermal change in the zero point.
For devices with NBR or HNBR seals, the values must be multiplied by a factor of 3.
All specifications apply to the temperature range –10 to +60 °C (+14 to +140 °F) and a turn down of 1:1.

Measuring cell	PMC71	PMC71 high-temperature version
	% of URL	
100 mbar (1.5 psi), 250 mbar (4 psi), 400 mbar (6 psi)	0.2	0.46
1 bar (15 psi), 2 bar (30 psi), 4 bar (60 psi), 10 bar (150 psi), 40 bar (600 psi)	0.15	0.46

Total error - PMC71

The total error comprises the long-term stability and the total performance.
For devices with NBR or HNBR seals, the values must be multiplied by a factor of 3.
All specifications apply to the temperature range –10 to +60 °C (+14 to +140 °F) and a turn down of 1:1.

Measuring cell	PMC71	PMC71 high-temperature version
	% of URL/year	
100 mbar (1.5 psi), 250 mbar (4 psi), 400 mbar (6 psi)	0.25	0.51
1 bar (15 psi), 2 bar (30 psi), 4 bar (60 psi), 10 bar (150 psi), 40 bar (600 psi)	0.2	0.51

Figure B.1.: Datasheet Endress-Hauser Cerabar S PMC71. Image from [End17], printed with permission from *Endress+Hauser Messtechnik GmbH+Co. KG.*

2701 Ethernet Multimeter/Data Acquisition System

DC SPEED vs. NOISE REJECTION

Rate	Filter	Readings/s[12]	Digits	RMS Noise 10V Range	NMRR	CMRR[14]
10	50	0.1 (0.08)	6.5	<2.5 µV	110 dB[13]	140 dB
1	Off	15 (12)	6.5	<6 µV	90 dB[13]	140 dB
0.1	Off	500 (400)	5.5	<40 µV	-	80 dB
0.006	Off	3000 (3000)	4.5	<300 µV	-	80 dB
0.002	Off	3500 (3500)	3.5	<1 mV	-	60 dB

DC MEASUREMENT CHARACTERISTICS

DC Volts

A-D LINEARITY: 2.0 ppm of reading + 1.0 ppm of range.

INPUT IMPEDANCE:

100mV-10V Ranges: Selectable >10GΩ// with <400pF or 10MΩ ±1%.
100V, 1000V Ranges: 10MΩ ±1%.

EARTH ISOLATION: 500V peak, >10GΩ and <300pF any terminal to chassis.

INPUT BIAS CURRENT: <75pA at 23°C.

COMMON MODE CURRENT: <500nApp at 50Hz or 60Hz.

AUTOZERO ERROR: Add ±(2ppm of range error +5µV) for <10 minutes and ±1°C.

INPUT PROTECTION: 1000V, all ranges, 300V with plug-in modules.

Resistance

MAX 4WΩ LEAD RESISTANCE: 10% of range per lead for 100Ω and 1kΩ ranges; 1kΩ per lead for all other ranges.

OFFSET COMPENSATION: Selectable on 4WΩ 100Ω, 1kΩ, and 10kΩ ranges.

CONTINUITY THRESHOLD: Adjustable 1 to 1000Ω.

INPUT PROTECTION: 1000V, all Source Inputs, 350V Sense Inputs, 300V with plug-in modules.

DC Current

SHUNT RESISTORS: 100mA-3A, 0.1Ω. 20mA, 5Ω.

INPUT PROTECTION: 3A, 250V fuse.

Thermocouples

CONVERSION: ITS-90.

REFERENCE JUNCTION: Internal, External, or Simulated (Fixed).

OPEN CIRCUIT CHECK: Selectable per channel. Open >11.4k ±200Ω.

DC Notes

1. 20% overrange except on 1000V and 3A.
2. Add the following to "ppm of range" uncertainty; 100mV 15ppm, 1V and 100V 2ppm, 100Ω 30ppm, 1k→<1MΩ 2ppm, 10mA and 1A 10ppm, 100mA 40ppm.
3. ±2% (measured with 10MΩ input resistance DMM, >10GΩ DMM on 10MΩ and 100MΩ ranges).
4. Relative to calibration accuracy.
5. For signal levels >500V, add 0.02ppm/V uncertainty for portion exceeding 500V.
6. Specifications are for 4-wire Ω, 100Ω with offset compensation on, 77xx plug-in module with LSYNC and offset compensation on. With offset compensation on OPEN CKT. VOLTAGE is 12.8V. For 2-wire Ω add 1.0Ω to "ppm of range" uncertainty.
7. Must have 10% matching of lead resistance in Input HI and LO.
8. Add the following to "ppm of reading" uncertainty when using plug in modules:

	10 kΩ	100 kΩ	1 MΩ	10 MΩ	100 MΩ
All Modules:				220 ppm	2200 ppm
7701, 7703, 7707, and 7709 Modules:	10 ppm	100 ppm	1000 ppm	1%	10%
7706, 7708 Modules:	5 ppm	50 ppm	500 ppm	5000 ppm	5%
7710 Model 23°C ±5°C:	11 ppm	110 ppm	1100 ppm	1.1%	11%
7710 Model Temp Coeff. >28°C→50°C	0.3 ppm/°C	3 ppm/°C	30 ppm/°C	0.03%/°C	0.3%/°C

9. Add 1.0V when used with plug-in modules.
10. For RATIO, DCV only. For AVERAGE, DCV and Thermocouples only. Available with plug-in modules only.
11. Add 6µV to "of range" uncertainty when using Models 7701, 7703, and 7707, 3µV for Models 7706, 7709, and 7710.
12. Auto zero off.
13. For LSYNC On, line frequency ±0.1%. For LSYNC Off, use 60dB for ≥ 1PLC.
14. For 1kΩ unbalance in LO lead.
15. Speeds are for 60Hz (50Hz) operation using factory defaults operating conditions (*RST). Autorange off, Display off, Limits off, Trigger delay = 0.
16. Speeds include measurements and data transfer out the ethernet (reading elements only). (100BaseT Ethernet, 3 meter RJ-45 crossover cable, PIII-800, Windows version 98 SE, VB version 6.0, direct Winsocket interface).
17. Sample count = 1000 (into memory buffer), auto zero off.
18. Auto zero off, NPLC = 0.002.
19. Additional Uncertainty

Type	Range	7710 Module Using CJC
J	0 to +760°C	1.5°C
K	0 to +1372°C	—
N	0 to +1300°C	0.5°C
T	0 to +400°C	0.5°C
E	0 to +1000°C	0.5°C
R	+400 to +1768°C	0.9°C
S	+400 to +1768°C	0.9°C
B	+1100 to +1820°C	0.9°C

			Plug-In Modules				
Type	Range	Front Terminals Sim. Ref. Junction	7709 Sim. Ref. Junction	7701, 7703, 7707 Sim. Ref. Junction	7700 and 7708 Using CJC	7706 Using CJC	7710 Using CJC
J	-200 to 0°C	0.1	0.1	0.3	0.8	1.6	4.5
K	-200 to 0°C	0.2	0.2	0.4	0.8	1.6	1
N	-200 to 0°C	0.3	0.3	0.6	0.8	1.6	2.5
T	-200 to 0°C	0.2	0.1	0.4	0.8	1.6	2.5
E	-200 to 0°C	-	0.1	0.3	0.8	1.6	2.5
R	0 to +400°C	0.4	0.6	1.2	0.5	1.0	2.2
S	0 to +400°C	0.4	0.6	1.2	0.5	1.0	2.2
B	+350 to +1100°C	0.8	0.3	1.7	0.5	1.0	2.2

20. For lead resistance >0Ω, add the following uncertainty/Ω for measurement temperatures of:

		70°–100°C	100°–150°C
2.2 kΩ	(44004)	0.22°C	1.11°C
5.0 kΩ	(44007)	0.10°C	0.46°C
10 kΩ	(44006)	0.04°C	0.19°C

21. Front Panel resolution is limited to 0.1Ω.

Figure B.2.: Datasheet Keithley Model 2701 Ethernet-Based DMM / Data Acquisition System. Image from [Kei03], printed with permission from *2017 Tektronix, Inc. All rights reserved. Tektronix products are covered by U.S. and foreign patents, issued and pending. TEKTRONIX and the Tektronix logo are registered trademarks of Tektronix, Inc..*

6220 Programmable Current Source

SOURCE SPECIFICATIONS

Range (+5% over range)	Accuracy (1 Year) 23°C±5°C ±(%rdg. + amps)	Programming Resolution	Temperature Coefficient/°C 0°-18°C& 28°-50°C	Typical Noise (peak-peak) /RMS[3,4,5] 0.1Hz-10Hz	Settling Time[1,2] (1% of final value)
2nA	0.4% + 2pA	100fA	0.02% + 200fA	400/80fA	100µs
20nA	0.3% + 10pA	1pA	0.02% + 200fA	4/0.8pA	100µs
200nA	0.3% + 100pA	10pA	0.02% + 2pA	20/4pA	100µs
2µA	0.1% + 1nA	100pA	0.01% + 20pA	200/40pA	100µs
20µA	0.05% + 10nA	1nA	0.005% + 200pA	2/0.4nA	100µs
200µA	0.05% + 100nA	10nA	0.005% + 2nA	20/4nA	100µs
2mA	0.05% + 1µA	100nA	0.005% + 20nA	200/40nA	100µs
20mA	0.05% + 10µA	1µA	0.005% + 200nA	2/0.4µA	100µs
100mA	0.1% + 50µA	10µA	0.01% + 2µA	10/2µA	100µs

ADDITIONAL SOURCE SPECIFICATIONS

OUTPUT RESISTANCE: >$10^{14}\Omega$. (2nA/20nA range)

OUTPUT CAPACITANCE: <10pF, <100pF Filter ON. (2nA/20nA range)

LOAD IMPEDANCE: Stable into 100µH typical.

CURRENT REGULATION: Line: <0.01% of range. **Load:** <0.01% of range.

VOLTAGE LIMIT (Compliance): Bipolar voltage limit set with single value. 0.1V to 105V in 0.01V programmable steps. Accuracy for 0.1V to 20V: 0.1% +20mV, accuracy for 20V to 105V: 0.1% + 100mV

MAX. OUTPUT POWER: 11W, four quadrant source or sink operation.

GUARD OUTPUT:

Maximum Load Capacitance: 10nF.

Maximum Load Current: 1mA for rated accuracy.

Accuracy: ±1mV for output currents <2mA. (excluding output lead voltage drop).

PROGRAM MEMORY: (offers point-by-point control and triggering, e.g. Sweeps)

Number of Locations: 64K.

EXTERNAL TRIGGER: TTL-compatible EXTERNAL TRIGGER INPUT and OUTPUT.

Max Trigger Rate: 1000/s.

6220 – 2182 MEASUREMENT FUNCTIONS

DUT RESISTANCE: Up to 1GΩ (1 nSiemen).

DELTA MODE RESISTANCE MEASUREMENTS and DIFFERENTIAL CONDUCTANCE: Controls Keithley Model 2182A Nanovoltmeter at up to 24Hz reversal rate (2182 at up to 12Hz).

Source Notes

1 Settling times are specified into a resistive load, with a maximum resistance equal to 2V / $I_{\text{fullscale of range}}$. See manual for other load conditions.
2 Settling times to 0.1% of final value are typically <2x of 1% settling times.
3 Noise current into <100Ω.
4 RMS Noise 10Hz-20MHz (2nA – 20mA Range) Less than 1mVrms, 5mVp-p (into 50Ω load).
5 Typical values are non-warranted, apply at 23°C, represent the 50^{th} percentile, and are provided solely as useful information.

Figure B.3.: Datasheet Keithley Model 6220 DC Current Source. Image from [Kei01], printed with permission from *2017 Tektronix, Inc. All rights reserved. Tektronix products are covered by U.S. and foreign patents, issued and pending. TEKTRONIX and the Tektronix logo are registered trademarks of Tektronix, Inc..*

Bibliography

[Aad12] G. Aad et al., *Observation of a new particle in the search for the Standard Model Higgs boson with the ATLAS detector at the LHC*, Phys. Lett. B **716**, 1 (2012) 1–29.

[Aba11] K. Abazajian et al., *Cosmological and astrophysical neutrino mass measurements*, Astropart. Phys. **35**, 4 (2011) 177–184.

[Ada08] P. Adamson et al., *Study of muon neutrino disappearance using the Fermilab Main Injector neutrino beam*, Phys. Rev. D **77**, 7 (2008) 072002.

[Ahm01] Q. R. Ahmad et al., *Measurement of the Rate of $\nu_e + d \to p + p + e^-$ Interactions Produced by ^8B Solar Neutrinos at the Sudbury Neutrino Observatory*, Phys. Rev. Lett. **87** (2001) 071301.

[Alt03] G. Altarelli et al., *Neutrino Mass*, Springer Tracts in Modern Physics, Springer Berlin Heidelberg (2003).

[Ang05] J. Angrik et al., *KATRIN design report 2004*, Wissenschaftliche Berichte FZKA **7090** (2005).

[Ase00] V. Aseev et al., *Energy loss of 18 keV electrons in gaseous T and quench condensed D films*, EPJ D **10**, 1 (2000) 39–52.

[Ase11] V. Aseev et al., *Upper limit on the electron antineutrino mass from the Troitsk experiment*, Phys. Rev. D **84**, 11 (2011) 112003.

[Asn13] D. Asner et al., *ILC Higgs white paper*, arXiv preprint arXiv:1310.0763 (2013).

[Bab12] M. Babutzka et al., *Monitoring of the operating parameters of the KATRIN Windowless Gaseous Tritium Source*, New J. Phys. **14**, 10 (2012) 103046.

[Bel14] G. Bellini et al., *Final results of Borexino Phase-I on low-energy solar neutrino spectroscopy*, Phys. Rev. D **89** (2014) 112007.

[Ber69] T. Bernstein et al., *Calculation of Self-Heating Current for a Resistance Wire Temperature Sensor*, IEEE T IND ELECTRON , 1 (1969) 99–102.

[BIP08] I. BIPM et al., *Evaluation of Measurement Data—Guide to the Expression of Uncertainty in Measurement GUM 1995 with minor corrections*, Joint Committee for Guides in Metrology, JCGM **100** (2008).

[Bod15] L. Bodine et al., *Assessment of molecular effects on neutrino mass measurements from tritium β decay*, Phys. Rev. C **91**, 3 (2015) 035505.

[Bor03] B. Bornschein et al., *Self-Charging of Quench Condensed Tritium Films*, J. Low Temp. Phys **131**, 1 (2003) 69–88.

[Bor06] B. Bornschein, *The closed tritium cycle of KATRIN*, Prog. Part. Nucl. Phys. **57**, 1 (2006) 38–48.

[Cha71] P. Chantry, *Doppler broadening in beam experiments*, J. Chem. Phys. **55**, 6 (1971) 2746–2759.

[Cha12] S. Chatrchyan et al., *Observation of a new boson at a mass of 125 GeV with the CMS experiment at the LHC*, Phys. Lett. B **716**, 1 (2012) 30–61.

[Chi10] S. Chilingaryan et al., *Advanced data extraction infrastructure: Web based system for management of time series data*, in *Journal of Physics: Conference Series*, volume 219, IOP Publishing (2010), p. 042034.

[Dre13] G. Drexlin et al., *Current direct neutrino mass experiments*, Advances in High Energy Physics **2013** (2013).

[Ell04] S. R. Elliott et al., *Double-beta decay*, J. Phys. G **30**, 9 (2004) R183.

[End17] Endress+Hauser Instruments International AG, *Technical Information Cerabar S PMC71, PMP71, PMP75* (2017).

[Fer34] E. Fermi, *Versuch einer Theorie der β-Strahlen. I*, Z. Phys **88** (1934) 161–177.

[Fis11] S. Fischer et al., *Monitoring of tritium purity during long-term circulation in the KATRIN test experiment LOOPINO using laser Raman spectroscopy*, FUSION SCI TECHNOL **60**, 3 (2011) 925–930.

[Fis14] S. Fischer, *Commissioning of the KATRIN Raman system and durability studies of optical coatings in glove box and tritium atmospheres*, Ph.D. thesis, Karlsruhe, Karlsruher Institut für Technologie (KIT) (2014).

[For14] D. Forero et al., *Neutrino oscillations refitted*, Phys. Rev. D **90**, 9 (2014) 093006.

[Fuk98] Y. Fukuda et al., *Evidence for Oscillation of Atmospheric Neutrinos*, Phys. Rev. Lett. **81** (1998) 1562–1567.

[Geh08] R. Gehring et al., *The Windowless Gaseous Tritium Source for the KATRIN Experiment*, IEEE Trans. Appl. Supercond. **18**, 2 (2008) 1459–1462.

[Gre12] W. Greiner et al., *Theoretical Physics Text and Exercise Books: Volume 5: Gauge Theory of Weak Interactions*, Springer Science & Business Media (2012).

[Gro08] S. Grohmann et al., *Cryogenic design of the KATRIN source cryostat*, in *AIP Conference Proceedings*, volume 985, AIP (2008), pp. 1277–1284.

[Gro09] S. Grohmann, *Stability analyses of the beam tube cooling system in the KATRIN source cryostat*, Cryogenics **49**, 8 (2009) 413–420.

[Gro11] S. Grohmann et al., *Precise temperature measurement at 30 K in the KATRIN source cryostat*, Cryogenics **51**, 8 (2011) 438–445.

[Gro13] S. Grohmann et al., *The thermal behaviour of the tritium source in KATRIN*, Cryogenics **56** (2013) 5–11.

[Gro17] R. Groeßle, *Discussion on the temperature regime for tritium dimer clusters*, personal communication (2017).

[Hal15] G. Hall, *Pearson's correlation coefficient*, other words **1** (2015) 9, http://www.hep.ph.ic.ac.uk/h̃allg/UG_2015/Pearsons.pdf.

[Han17] V. Hannen et al., *Deconvolution of the energy loss function of the KATRIN experiment*, Astropart. Phys. **89** (2017) 30–38.

[Höt12] M. Hötzel, *Simulation and analysis of source-related effects for KATRIN*, Ph.D. thesis, Karlsruhe, Karlsruher Institut für Technologie (KIT) (2012).

[Hye12] K. Hyeon-Deuk et al., *Intermolecular diatomic energies of a hydrogen dimer with non-Born–Oppenheimer nuclear and electron wave packets*, Chem. Phys. Lett. **532** (2012) 124–130.

[Ima08] Imagecreator, *An example of the correlation of x and y for various distributions of (x y) pairs.* (2008), file: https://commons.wikimedia.org/wiki/File:Correlation_examples.png.

[Jon01] E. Jones et al., *SciPy: Open source scientific tools for Python* (2001), http://www.scipy.org/ [Online accessed 2017-03-03].

[Kei01] Keithley Instruments Inc., *Model 7001 Switch System Instruction Manual* (2001).

[Kei03] Keithley Instruments Inc., *Model 2701 Ethernet-Based DMM / Data Acquisition System User's Manual* (2003).

[Kei05] Keithley Instruments Inc., *Model 6220 DC Current Source Model 6221 AC and DC Current Source User's Manual* (2005).

[Kle05] W. Kley, *Skript: Numerische Methoden* (2005), http://www.tat.physik.uni-tuebingen.de/ kley/lehre/numerik/script/kap4.pdf.

[Kra05] C. Kraus et al., *Final results from phase II of the Mainz neutrino mass searchin tritium decay*, EPJ C **40**, 4 (2005) 447–468.

[Kuc16] L. Kuckert, *The Windowless Gaseous Tritium Source of the KATRIN Experiment-Characterisation of Gas Dynamical and Plasma Properties*, Ph.D. thesis, Karlsruhe, Karlsruher Institut für Technologie (KIT) (2016).

[Lee57] T. D. Lee et al., *Parity nonconservation and a two-component theory of the neutrino*, Phys. Rev. **105**, 5 (1957) 1671.

[Lin05] P. J. Linstrom et al., editors, *NIST Chemistry WebBook, NIST Standard Reference Database Number 69*, National Institute of Standards and Technology, Gaithersburg MD, 20899 (2005).

[Lob85] V. Lobashev et al., *Numerical simulation of a low-energy electron electrostatic integral spectrometer with adiabatic magnetic collimation*, Nucl. Instr. Meth. Phys. Res. **238**, 2 (1985) 496–499.

[Lob00] V. M. Lobashev, *Direct search for the neutrino mass in the beta decay of tritium: Status of the "Troitsk ν-mass" experiment*, Phys. Atom. Nucl. **63**, 6 (2000) 962–968.

[Lob02] V. Lobashev, *Study of the tritium beta-spectrum in experiment "Troitsk -mass"*, Prog. Part. Nucl. Phys. **48**, 1 (2002) 123–131.

[Luc00] L. L. Lucas et al., *Comprehensive review and critical evaluation of the half-life of Tritium*, J. Res. Natl. Inst. Stand. Technol. **105**, 4 (2000) 541.

[Mak62] Z. Maki et al., *Remarks on the Unified Model of Elementary Particles*, Progr. Theor. Exp. Phys. **28**, 5 (1962) 870.

[Mer17] S. Mertens, *Coresspondence on the importance of the WGTS beam tube temperature stability for the search of sterile neutrinos*, personal communication (2017).

[Mic06] D. Michael et al., *Observation of muon neutrino disappearance with the MINOS detectors in the NuMI neutrino beam*, Phys. Rev. Lett. **97**, 19 (2006) 191801.

[Mye15] E. Myers et al., *Atomic masses of tritium and helium-3*, Phys. Rev. Lett. **114**, 1 (2015) 013003.

[Nak00] K. Nakamura, *Status of the K2K long-baseline neutrino-oscillation experiment*, Nucl. Phys. A **663–664** (2000) 795c–798c.

[Osi01] A. Osipowicz et al., *KATRIN: A Next generation tritium beta decay experiment with sub-eV sensitivity for the electron neutrino mass. Letter of intent*, Wissenschaftliche Berichte Forschungszentrum Karlsruhe Nr 6691 (2001).

[Ott08] E. W. Otten et al., *Neutrino mass limit from tritium decay*, Rep. Prog. Phys. **71**, 8 (2008) 086201.

[Pon58] B. Pontecorvo, *Inverse beta processes and nonconservation of lepton charge*, Sov. Phys. JETP **7** (1958) 172–173, [Zh. Eksp. Teor. Fiz.34,247(1957)].

[Pri13] F. Priester et al., *TriToP–A compatibility experiment with turbomolecular pumps under tritium atmosphere*, Vacuum **98** (2013) 22–28.

[Pri15] F. Priester et al., *Commissioning and detailed results of KATRIN inner loop tritium processing system at Tritium Laboratory Karlsruhe*, Vacuum **116** (2015) 42–47.

[Pri17] F. Priester, *Discussion on the stability of Leybold MAG W 2800 turbomolecular vacuum pumps*, personal communication (2017).

[Ram08] R. Ramalingam et al., *Study of Platinum sensors (PT-500) for the temperature measurement of the KATRIN WGTS-Beam Tube*, Technical Report FE.5130.0013.0012/M, Forschungszentrum Karlsruhe (2008).

[Ram12] R. Ramalingam et al., *Directional oriented magnetic field induced temperature error of PT-500 sensor at cryogenic environment*, in *AIP Conference Proceedings*, volume 1434, AIP (2012), pp. 507–514.

[Rob91] R. G. H. Robertson et al., *Limit on* ν_e *mass from observation of the* β *decay of molecular tritium*, Phys. Rev. Lett. **67** (1991) 957–960.

[Sae00] A. Saenz et al., *Improved molecular final-state distribution of HeT+ for the* β*-decay process of T 2*, Phys. Rev. Lett. **84**, 2 (2000) 242.

[Sch15] M. Schlösser et al., *Raman spectroscopy at the tritium laboratory Karlsruhe*, FUSION SCI TECHNOL **67**, 3 (2015) 555–558.

[Sha49] C. E. Shannon, *Communication in the presence of noise*, Proceedings of the IRE **37**, 1 (1949) 10–21.

[Suz99] Y. Suzuki, *Solar neutrino results from Super-Kamiokande*, Nucl. Phys. B **77**, 1 (1999) 35–42.

[Val11] K. Valerius et al., *Prototype of an angular-selective photoelectron calibration source for the KATRIN experiment*, J. Instrum. **6**, 01 (2011) P01002.

[Wat67] R. A. Watkins et al., *Thermomolecular Pressure Difference Measurements for Precision Helium- 3 and Helium- 4 Vapor-Pressure Thermometry*, J. Chem. Phys. **46**, 3 (1967) 1007–1018.

[Wei99] C. Weinheimer et al., *High precision measurement of the tritium β spectrum near its endpoint and upper limit on the neutrino mass*, Physics Letters B **460**, 1 (1999) 219–226.

[Wil87] J. F. Wilkerson et al., *Limit on ν^- e Mass from Free-Molecular-Tritium Beta Decay*, Phys. Rev. Lett. **58**, 20 (1987) 2023.

Danksagung

Im Rahmen der Erstellung dieser Arbeit und der dazu notwendigen Messungen wurde mir von vielen Personen tatkräftig geholfen, weswegen ich ihnen an dieser Stelle dafür danken möchte. Ohne diese Personen wäre diese Arbeit nicht möglich gewesen und meine Zeit am TLK wesentlich weniger mit Spaß erfüllt.

Für die Ermöglichung dieser Arbeit möchte ich Herrn Prof. Dr. Guido Drexlin ganz herzlich danken. Sein beherzter Einsatz in den Astroteilchenphysik Vorlesungen hat mich erst zu KATRIN gebracht und durch seinen Ansporn während der Durchführung meiner Arbeit hat er mich dazu motiviert die besten Ergebnisse zu erzielen.

Ich möchte Herrn Prof. Dr. Bernhard Holzapfel dafür danken, dass er sich bereit erklärt hat, meine Arbeit als zweiter Gutachter zu bewerten.

Immer verfügbar und mit gutem Rat zur stelle möchte ich Frau Dr. Beate Bornschein danken. Ihre Leitung hat es mir erst ermöglicht das inhaltliche wie auch förmliche Qualitätsniveau dieser Arbeit zu erreichen und nicht den Tücken von Zeit-Mismanagement zu erliegen. Ebenfalls möchte ich Herrn Dr. Lutz Bornschein für die vielen praktischen Kniffe, die ich während der Zusammenarbeit mit ihm lernen durfte, sowie die vielen netten Gespräche bei einer heißen Schokolade danken.

Insbesondere möchte ich meinen beiden Betreuern, Moritz Hackenjos und Hendrik Seitz-Moskaliuk danke. Moritz verdanke ich viele meiner im Laufe dieser Arbeit erworbenen Fertigkeiten im Labor. Unter ihm durfte ich viel über Vakuum- und Kryosysteme lernen. Hendrik möchte ich für seine Unterstützung bei der Kalibrierung sowie bei der Interpretation der Ergebnisse danken. Seine gnadenlos ehrlichen Korrekturen dieser Arbeit haben es mir erlaubt viel über das schreiben einer wissenschaftlichen Arbeit zu lernen und mir trotzdem den vollen Freiraum gelassen um meine eigenen Ideen zu Papier zu bringen.

Dem weiteren WGTS-Team bestehend aus Alexander Jansen, Benedigt Kuffner, Alan Kumb, Heike Bolz und Florian Heizmann möchte ich für die gute Zusammenarbeit danken, ohne die der Betrieb der WGTS oder die Kalibrierung der Pt500 Sensoren nicht möglich gewesen wäre. Alexander Jansen möchte ich für seine Leitung und sein profundes Wissen rund um die WGTS danken auf das ich mich immer verlassen konnte. Für die gute Zusammenarbeit und seine Expertise mit dem Dampfdrucksystem zur Kalibrierung der Pt500 sensoren danke ich Benedigt Kuffner. Während der Inbetriebnahme der WGTS habe ich viele Stunden an Lecktests mit Alan Kumb durchgeführt und möchte ihm dafür danken, dass er diese tröge Arbeitszeit wesentlich angenehmer gemacht hat. Heike Bolz möchte ich für ihre Hilfe bei der Inbetriebnahme des Temperaturerfassungssystems sowie Umbauten daran, die ohne sie nicht in dieser Form möglich gewesen wären, danken. Bei Florian Heizmann möchte ich mich für die Mitarbeit an Inbetriebnahme und Kalibrierungen bedanken.

Für die schöne Zeit am TLK möchte ich mich bei Michael Sturm, Marco Röllig, Florian Priester, Simon Niemes, Matthias Wecker, Alexander Kraus, Max Reimer, Michael Gross und Genrich Zeller bedanken. Die vielen humor-gefüllten und interessanten Gespräche haben das vergangene Jahr lehrreich und aufheiternd gestaltet.

Abschließend möchte ich meinen Eltern und meiner Schwester für die stetige Unterstützung meines Studiums danken.